The distributions of stellar remnants in disk galaxies

Submitted by

Matthew Molloy B.Sc.

for the degree of

Master of Science

to the

School of Physical Sciences

at

Dublin City University

November 2011

Supervisors

Dr. Laura Norci

Prof. Dr. Evert Meurs

I hereby certify that this material, which I now submit for assessment on the programme of study leading to the award of Master of Science is entirely my own work, and that I have exercised reasonable care to ensure that the work is original, and does not to the best of my knowledge breach any law of copyright, and has not been taken from the work of others save and to the extent that such work has been cited and acknowledged within the text of my work.

Signed: ____________________ ID No.: __________ Date: _____

Contents

List of Figures

List of Tables

Abstract

Data from the Asiago SN catalogue is used to study the distributions of CC SNae about their host galaxy. The vertical distribution of CC SNae in edge-on galaxies is fit with a sech ^{2} profile with scaleheight 0.49±0.08kpc. A photometric method is developed and applied to the sample and a separate sample of six runaway candidates is found. The radial distribution of CC SNae is also studied for the case of face-on disk galaxies. The surface density distribution is fit with and exponential profile with scalelength $0.67{\pm}0.18R_{Gal}$. A selection effect is confirmed to be present in the centres of disk galaxies and taking this into account we tentatively fit the surface density distribution with a scalelength of $0.35{\pm}0.05R_{Gal}$. The selection effect is shown to increase in strength for ever distant galaxies. The dynamics of massive runaway stars is modelled using a (fifth and sixth order) Runge-Kutta scheme and a galactic potential that produces a flat rotation curve. We find that a velocity kick imparted during the SN of a former binary companion is generally not enough to displace the SN progenitor to distances beyond 2kpc above the plane of the disk for progenitors witha disk scaleheight of $<0.4h_z$. The dispersion of HMXBs from their birthplace in the spiral arms is also modelled. For this purpose we develop a population synthesis model which includes the effects of mass transfer and tidal interactions to evolve a sample of binary systems. A kick is then applied to the SN remnant of one of the components in the binary. We determine the disruption rate of these binaries for various kick velocity distributions. The undisrupted binaries are then assumed to produce X-ray emission due to a wind fed mechanism and we use these objects to populate a dynamical model. We find that there is no obvious dispersion from the spiral pattern and show that HMXBs are an excellent tracer for recent star formation.

Chapter 1

Introduction

Supernova events are important areas of study when looking at many different astrophysical phenomena. They are important for areas such as nucleosynthesis and galactic chemical enrichment, determining the origins of neutron stars and black holes, the study of cosmic rays, the disruption of the interstellar medium (ISM) and subsequent star formation and their use as cosmological standard candles.

They can be set into separate classes and subclasses depending on their spectra (and the temporal evolution of the spectra) and their photometric characteristics. There are two main classes established by Minkowski (1941) which are denoted Type I/II SNae and are based on clear spectral differences. Type I SNae show no obvious Hydrogen in their spectra (although in some cases it may appear to be due to contamination of the spectra). Type II SNae show prominent Hydrogen lines which can vary temporally.

SNae II, Ib and Ic have never been found in elliptical/S0 galaxies and are usually found in HII regions (in or around spiral arms and OB associations) which suggests that their progenitors were massive stars with M $\gtrsim 8-10M_{\odot}$ (Huang, 1987). SNae Ia tend to occur in all types of galaxies. They are more common in spirals and are randomly distributed with no particular region having an excess (McMillan and Ciardullo, 1996). Della Valle (1994) showed that the luminosity of SNae Ia increases as one moves from early to late Hubble type galaxies. Studies have shown that the progenitors of SNae Ia are probably massive stars with M $\gtrsim$4-7M$_{\odot}$ of an intermediate age $\sim$1-5$\times 10^8$Yrs (Oemler and Tinsley, 1979). Woosley (1986) showed that the SNae Ia originate in binary systems with a white dwarf rich in carbon and oxygen. The white dwarf in this case then accreted matter from its companion and then underwent a thermonuclear runaway resulting in the SN explosion.

As mentioned above, the progenitors of SNae II/Ib/Ic are thought to be more massive stars than the progenitors of SNae Ia that underwent an Iron core collapse (CC) (usually) leaving behind a neutron star or black hole (Brown and Bethe, 1994). Due to the absence of Hydrogen in the spectra of SNae Ib/c it is thought that the progenitors of these explosions somehow lost their Hydrogen envelopes either through mass loss in a binary system or through very strong stellar winds (WR stars). The lack of Helium in SNae Ic suggests that the Helium envelope in these stars was also lost at some stage in their stellar evolution. Since stellar winds grow stronger with increasing metallicity a comparison of the distributions of varying types of CC SNae can be argued to trace the metallicity gradient in galaxies (Boissier and Prantzos, 2009).

A SN event in a binary system is one of many mechanisms which can alter the orbital parameters of the system. Others include the development of a common envelope and the interaction of the binary with another massive object. SN events in massive binary systems can eject a significant amount of mass from the system which changes the orbital dynamics. Here we estimate the effects of such a SN event on the disruption rate of massive binaries (Section 4.2). When the SN shell passes the companion star there is a sizeable drop in gravity and depending on the details of the evolution, the eccentricity of the orbit and the velocity kick due to an asymmetric SN, the SN remnant may not stay with the secondary, releasing both as runaway stars. In most cases, not enough mass is released to unbind the companions (Blaauw, 1961) and the runaway is expected to remain a binary, an example of which are High Mass X-ray Binaries (HMXBs) which have velocities of $\sim$50kms^{-1} (van den Heuvel et al., 2000). It will be shown that if the mass of the ejecta exceeds a certain limit, or if the companion star is small enough, then the binary system can become unbound. It will also be shown that if the SN is asymmetric, the ejecta can impart a very strong kick to the post-SN object which unbinds the system and can cause the binary components to be flung off at very high speeds. These runaway stars have massive peculiar velocities and are the subject of great interest as some appear to be leaving the galaxy altogether (Irrgang et al., 2010).

This thesis has three main Sections. We firstly, in Chapter 2, look at the distributions of CC SNae in disk galaxies. We use a sample of SNae from the Asiago SN database for the case of edge-on and face-on galaxies. In the case of the edge-on sample we investigate the height distribution of SNae above/below the plane of the galaxy and develop a photometric method to extract a sample of runaway candidates. For the face-on sample we use de-projected and normalised radial distances to determine a surface density distribution. In Chapter 3 we model the dynamics of these runaways by distributing a sample of massive stars according to the observed light profiles of disk galaxies, giving each star a high space velocity and following their trajectories in an axisymmetric disk potential. In Chapter 4 we investigate the dispersion of HMXBs from their birthplace in the spiral arms. For this purpose we develop a population synthesis model in which we evolve massive binaries. These binaries are then used to populate a dynamical model in which they are distributed about a spiral pattern. We then measure the dispersion of the population from the spiral pattern.

Chapter 2

Observing Runaways

2.1 Introduction

While SNae have been the subject of great interest for most of the past century, studies have mainly focused on the physical processes which govern their evolution. Models have been created to try to explain the enormous release of energy and the spectral features that are associated with SNae (eg. (Thielemann et al., 2004)). However, there have been only a few investigations into the distribution of SNae about their host galaxies and into the study of how many of these may have been ejected from their progenitor's birthplace by either a dynamical event or a SN in a binary system. This can be a fruitful endeavour since SNae can be seen from distant galaxies and their distribution can tell us about star-forming regions in these galaxies. With the flood of high quality data about SNae and their host galaxies becoming available, more accurate distribution studies can be done.

A recent paper by Hakobyan et al. (2009) used SNae and host galaxy data to study the radial distribution of SNae in face-on galaxies. They used the data from the Asiago database to conduct their survey and then compared their results with those that describe the distributions of stars and ionized gases. They found that the distribution of core-collapse SNae is consistent with an exponentially decaying law similar to the distribution of light attributed to the disk structure in edge-on spiral galaxies. They derive an exponential distribution of core-collapse SNae with a scale length of $h_{SN} = 0.29R_{25}$ (where R_{25} is the radius of the galaxy derived from the 25th B-band magnitude isophotal diameter - here denoted R_{Gal}). They also notice that there is a deficit of SNae in the centre of spiral galaxies within $0.2R_{Gal}$ and argue that this could be due to extinction in the central bulge regions of spirals or that the brightness of the central regions hinders the discovery of SNae in those places. They also note that the scale lengths they derive are in agreement with the scale lengths of ionized gas reported by Athanassoula et al. (1993) even though there is a large uncertainty in these values.

With regard to the distribution of secondary SNae (those that have been ejected from their original cluster by a kick imparted by a former binary companion) only one study has investigated candidates in the solar neighbourhood. Hoogerwerf et al. (2001) looked at 56 runaway stars to determine, with accurate proper motions and parallaxes, the cause of their runaway status. They use these data to trace back the path of these runaways and associate them with a parent cluster and then, with the timescales involved, deduce whether the SN was ejected either in a dynamical ejection scenario (DES) or a binary SN scenario (BSS). A DES is a scenario in which a young star undergoes a three- or n-body gravitational interaction and is ejected from the parent cluster and would seen as having a large peculiar motion compared to the stars in the parent cluster (Blaauw, 1961). A BSS is a scenario in which a (stable) binary system is disrupted due to the SN explosion of one (in most cases the "primary", the initially most massive star) of the components. The SN explosion ejects matter from the system and in some cases can be asymmetric, resulting in a kick being imparted to the SN remnant. In Section 4.2 we describe the effects of such an occurrence in a massive binary system which can completely disrupt a binary system sending both components out with a high space velocity (Hills, 1983). Out of their sample of 56 runaways they were able to determine the parent cluster and the likely cause of the ejection for 16 objects. Eleven out of the 16 were deemed to have been ejected via a velocity kick imparted by a SN and the rest were ejected in a gravitational interaction. Another candidate had two possible parent clusters but in either case was argued to have been ejected via a BSS. This gives some idea of the statistical properties of both types of runaways (even though the sample is small) suggesting that about two thirds of runaways are ejected via a BSS and a third are ejected via a DES. These estimates can then be used to draw conclusions about the distributions of SNae found in surveys in that it implies that some SNae should occur away from the birthplace of the progenitor. A number of models have also been created to determine the fractions of SNae ejected by DES or BSS (a ratio of 50:50 for O-type stars with B-type stars having a slightly higher chance of being ejected in a BSS (O Maoileidigh, 2009))

Models of high velocity O- and B-stars also shed light on the SN distributions. Dray et al. (2005) ran numerical simulations of binary interactions to estimate the fraction of O-type runaways caused by gravitational or SN interactions. They estimate that the fraction of O-type runaways can be as high as 50% of the total O-type population but that, due to the asymmetry of SN explosions, many of these will have a space velocity that is too low for them to be observed as runaways. The percentage of all O stars that are runaways has been observed to lie between 10% and 30% (Gies, 1987) while de Wit et al. (2005) suggest that a further 20% are not resident in a parent cluster but are not identified as runaways, due to their low space velocities. This result correlates well with the model by Dray et al. (2005).

The characteristics of runaway O- and B- stars has been investigated by Portegies Zwart (2000) who ran binary population synthesis calculations with the primary star exploding in a SN and imparting a kick to its companion. The results of his model suggested that in order to maximise the amount of runaways the binary fraction of O and B stars should be approaching 100% and that the masses of both stars should be roughly equal. He argues that BSS runaways should exhibit a high rotational velocity and lower than usual helium abundances due to accretion of material from the 'pre-SN' primary and that this would rejuvenate the runaway to the point where it would appear as a "blue straggler" in its parent group. He also points out that the frequency of O type runaways from his model ($\sim 2\%$) may be much lower than the observed frequency ($\sim 20\%$) because many young early type stars may be hidden in the clouds in which they are born, increasing the fraction of observed O-star runaways. His model, however, only allows runaways to be produced by a SN which may distort the results since strong gravitational forces, which can also create runaways, could perturb the initial binary fractions and also the mass fractions.

A paper by Kazarian (1997) attempted to link the distribution of SNae with active or star forming galaxies (with a UV excess) but showed no correlation. That study concluded that the rates of SNae are not enhanced in active galaxies.

2.2 The Sample

The sample of SNae is taken from the Asiago SN database which is maintained by the Asiago-Padova SN group, is updated regularly with SN discoveries announced in the IAU circulars and supplemented with additional information from the NED and LEDA galaxy databases. The database is easily accessible on a web form hosted by the Vizier service.[1] As of the 9th of October 2011 the catalogue contained 5,745 instances of recorded SNae. Out of this catalogue we have selected edge-on galaxies as an investigation into the positions of SNae relative to their parent galaxy should

[1] The database is available at *http://vizier.u-strasbg.fr/viz-bin/VizieR* by searching for "Asiago".

exhibit more runaway candidates if the host galaxy is viewed edge on since a SN that is above or below the galaxy disk, away from the likely birthplace of its progenitor, would be easier to spot than if looking at the galaxy face-on. We use only Core-Collapse (CC) for this purpose, the progenitors of which are formed primarily in the thin disk of spiral galaxies. A photometric method is defined and employed to separate the SNae that are placed away from an idealised representation of their host galaxy. We also investigate the distributions of CC SNae for a sample of face-on galaxies using de-projected and normalised radial distances. For the face-on sample we also compare the radial distributions of type Ib/c and type II SNae.

2.2.1 Constraints

Each SN is required to have a known Position Angle (PA) so that the orientation of the galaxy in the sky could be determined and from that, the position of the SNae in relation to the galactic nucleus. Another required parameter was the redshift, z, of the host galaxy which was needed to calculate values for the distance to the galaxy, D, the diameter and radius of the host galaxy, D_{Gal} and R_{Gal} respectively, and also the real distance, in kpc, of the SNae from the galactic disk and nucleus.

For the case of investigating SNae in edge-on galaxies we restrict the inclination of the host (disk) galaxy to between 80° and 90° so as to limit projection effects. Also, since this is an investigation into the distributions of Core-Collapse SN we require the SN to be classified as either a type II, Ib or Ic (or some variant, eg. type IIp or IIl). Applying these restrictions we retrieve a sample for the edge-on investigation of 64 SN, all of which reside in spiral galaxies with redshifts $0.0018 < z < 0.0383$. For the photometric method outlined below we also require for the edge-on sample a galaxy type code, T, which gives an indication of the host galaxy's place along the Hubble sequence. From this it is possible to infer some characteristics of the host galaxy.

For the case of face-on galaxies we restrict the inclination of the host galaxy to below 50° and in the same way as for the edge-on case, we constrain the sample by SN type. For the face on sample we retrieve a total of 444 SNae which reside in spiral galaxies with redshift $0.0007 < z < 0.0514$. For both samples it is required that the offset from the host galaxy centre is known as well as a position angle of the host galaxy and also an isophotal diameter of the host galaxy which is used to normalise distances in later parts of the study.

2.2.2 Work on the Sample

The following section outlines the work performed on each sample. The parameters used in the calculations are listed in Table 2.1.

Parameter	Units
Inclination, i	degrees
Position Angle, PA	degrees
Redshift, z	$\sim$
Isophotal Diameter, d_{iso}	$\log_{10} d_{iso}$ [B_{25}] [d in 0.1 arcmins]
SN offset in the x-direction, x	arcsec (East/West)
SN offset in the y-direction, y	arcsec (North/South)
Galaxy type code, T	$\sim$

Table 2.1: *This table lists the parameters used in the following calculations.*

Edge-on

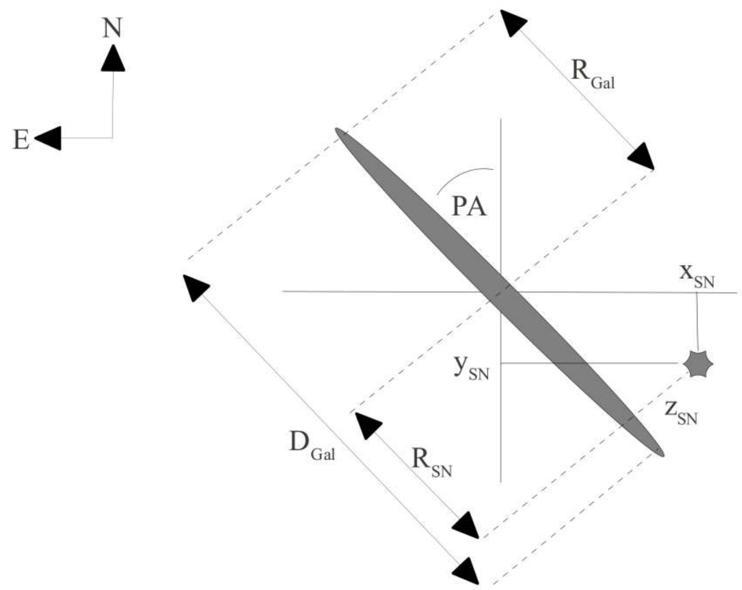

Figure 2.1: *This figure shows how the orientation of galaxies is defined for the edge-on sample. The galaxy was taken to be a line through the origin with the position angle (PA) determining the slope of the line. The length of the line was set by the isophotal diameter (D_{Gal}) and the position of the SN was given by the offset values.* $R_{Gal} = \frac{1}{2} D_{Gal}$.

In order to determine the distances of the SN along the host galaxy, R_{SN}, and the height of each SN above the disk of the galaxy, z_{SN} (see Figure 2.1), it is assumed that the host galaxy centre is located at the origin of a Cartesian coordinate system.

The disk of the galaxy is taken to be a line, through the origin, with a slope, m, calculated from the position angle, PA

$$y = mx \tag{2.2.1}$$

where

$$m = \frac{1}{\tan(PA)} \tag{2.2.2}$$

giving an equation for the line representing the disk of the galaxy

$$y = \left(\frac{1}{\tan(PA)}\right) x \tag{2.2.3}$$

where x is the coordinate in the East/West direction and y the coordinate in the North/South direction. As the centre of the host galaxy is taken to be at the origin the position of the SN is given simply by the offset values (x_{SN} and y_{SN}) from which the vertical height of the SN, above/below the plane of the disk, is given by

$$z_{SN} = \frac{|ax_{SN} + by_{SN} + c|}{\sqrt{a^2 + b^2}} \tag{2.2.4}$$

where in this case $a = m$, $b = -1$ and $c = 0$ giving

$$z_{SN} = \frac{mx_{SN} - y_{SN}}{\sqrt{m^2 + 1}} \tag{2.2.5}$$

The distance of the SN along the galaxy is found by first defining a line, perpendicular to the plane of the galaxy, which intersects the position of the SN. The slope of this line, $m_{\perp}$, is given simply by

$$m_{\perp} = \frac{-1}{m} = -\tan(PA) \tag{2.2.6}$$

giving an equation for the perpendicular line of

$$y - y_{SN} = (\frac{-1}{m})(x - x_{SN}) \tag{2.2.7}$$

or

$$y = m_{\perp}x + c_{\perp} \tag{2.2.8}$$

where

$$c_{\perp} = \frac{x_{SN}}{m} + y_{SN} \tag{2.2.9}$$

Subsequently, the point of intersection of this perpendicular line, which goes through the position of the SN, with the plane of the galaxy, x_{int} and y_{int}, is then used to deduce the distance of the SN along the plane of the galaxy, away from the centre.

$$x_{int} = \frac{c_{\perp}}{m + \frac{1}{m}} \tag{2.2.10}$$

$$y_{int} = m_{\perp} x_{int} + c_{\perp} = \frac{-1}{m} \left[\frac{c_{\perp}}{m + \frac{1}{m}} \right] + c_{\perp} \tag{2.2.11}$$

Giving

$$R_{SN} = \sqrt{x_{int}^2 + y_{int}^2} \tag{2.2.12}$$

where R_{SN} is in arcseconds.

An attempt is also made to quantify the possible errors associated with projection effects in inclined galaxies. It is assumed above that the SN lies at a distance which is exactly equal to the distance to the centre of the host galaxy. It is not known whether each of the SN is located on the near or far side of the galaxy - this provides some ambiguity in the true height of the SN above/below the disk of the host galaxy (see Figure 2.4(a)). For this error analysis it is assumed that each of the host galaxies is an infinitely thin circular disk. The error in the height (z_{SN}) due to this projection effect will be a function of the galaxy's inclination and the distance of the SN along the disk (or, more accurately, the normalised distance R_{SN}/R_{Gal} where R_{Gal} is the radius of the disk defined by the isophotal diameter). This error will be at a maximum for those SN with R_{SN}/R_{Gal}= 0 since the distance variation over the disk (see y in Figure 2.4(b)) will be at a maximum here. As seen in Figure 2.2 the parameters R_{Gal} and R_{SN} lead to

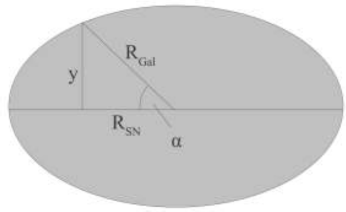

Figure 2.2: *Looking at a slightly inclined galaxy the parameter α is found from the known values of R_{SN} and R_{Gal}. From this the total distance through the disk for a given value of R_{SN}, 2y, is found.*

$$\alpha = \cos^{-1}\left(\frac{R_{SN}}{R_{Gal}}\right) \tag{2.2.13}$$

and

$$y = R_{Gal}\sin(\alpha) \tag{2.2.14}$$

where $2y$ is the (real, de-projected) complete distance through the disk from the observers point of view at R_{SN}. As can be seen from Figure 2.4, if the SN is at the far side of the galaxy then its true height above the disk will be much smaller than if it were at the near side of the disk. Following the assumptions above, the SNs true height can be anywhere in the range $z_{SN} \pm \epsilon_z$ where

$$\epsilon_z = y\sin(\beta) \tag{2.2.15}$$

and β is calculated from the inclination of the galaxy, i

$$\beta = 90° - i \tag{2.2.16}$$

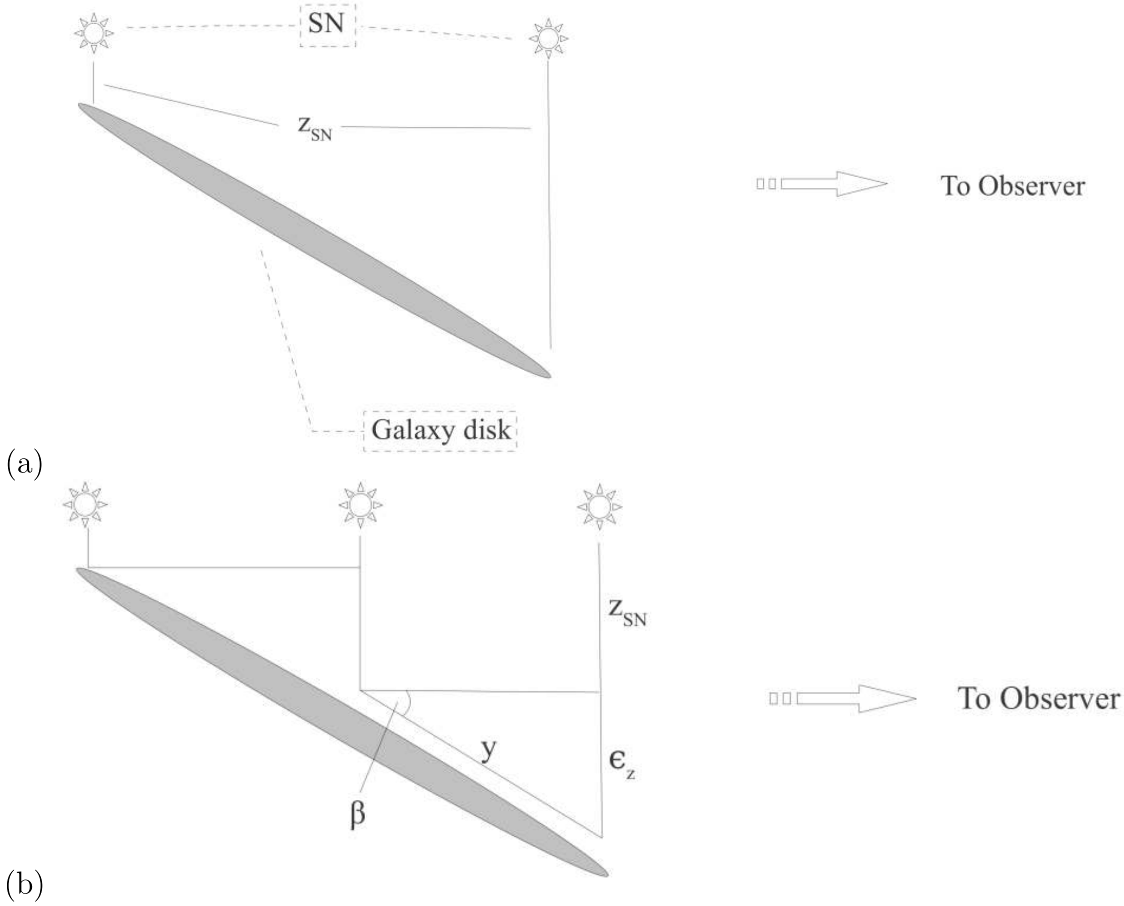

Figure 2.4: *(a) Depending on whether the SN lies at the front of the disk or at the back, the value of z_{SN} computed above may be an under- or over-estimate. Assuming that the disk is completely circular, a crude estimation of the error in z_{SN}, ϵ_z may be made. (b) β is easily calculated from the inclination i and y, the distance through the disk at a given value of R_{SN}, follows from known values (R_{SN} and R_{Gal}) allowing an estimation of the error in z_{SN}.*

An obvious shortcoming of this error calculation is that it is zero for perfectly edge-on galaxies and fails to take into account the thickness of the galaxy. It does however give at least some idea of the possible true heights of SN above their host galaxy and in certain cases assures the reader that a SN must lie well above the disk of the galaxy (see for example Figure 2.3 which shows the position of SN2007ac - 3.9kpc above the disk of galaxy UGC10550 which has a recorded inclination of 83°).

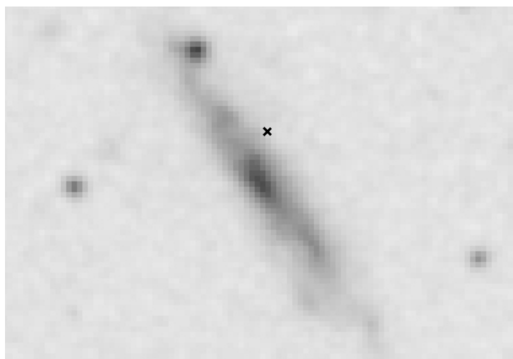

Figure 2.3: *Above shows the position of SN2007ac (black x) which occurred over 3.9kpc above the disk of its host galaxy UGC10550.*

For a galaxy with an inclination of 80° the maximum possible error in z could be as much as $0.17R_{Gal}$ (At $R_{SN} = 0$). Although this error calculation is also a function of R_{SN}, the upper limit for this kind of error in a galaxy with $R_{Gal} = 15$kpc is 2.55kpc which is non-negligible given the dimensions of disk galaxies.

We also introduce a method, based on the light profiles of observed edge-on galaxies, that aims to separate potential runaway candidates from the ever increasing samples of SNae using only the parameters available from the Asiago SN database. We define a synthetic galaxy based on the available parameters of each host galaxy from the edge-on sample. We then calculate the expected surface brightness at the point where the SN in question lies and apply a criterion to determine whether the SN could be considered away from the disk. The method assumes that the distribution of light in edge-on disk galaxies can be adequately described by a function of the form

$$I(r, z) = I_0 \exp\left(\frac{-r}{h_r}\right) \operatorname{sech}^2\left(\frac{z}{h_z}\right) \tag{2.2.17}$$

where $I(r, z)$ and I_0 are the brightness at (r,z) and (0,0) respectively and h_r and h_z are the scalelength and scaleheight of the brightness distribution respectively. Along with the parameters used above we also use the morphological type code, T, of the host galaxy which gives an indication of where the galaxy sits on the Hubble sequence: $1< n <4$ indicates galaxies in the range Sa-Sbc and $n >4$ indicates galaxies of type Sc and later. We use this morphological code to assign each case a scaleheight by noting that early type galaxies ($1< n <4$) have been shown to have systematically thicker disks than later type galaxies ($n >4$) (de Grijs, 1998). From a sample of edge-on galaxies Mosenkov et al., (Mosenkov et al., 2010) have shown that scaleheights can lie in the range 0.4 - 1.2kpc [1]. We therefore set the scaleheights for our synthetic galaxy profiles as having a simple linear relation to the host galaxy's morphological type code. We set the scalelengths of the synthetic galaxies as a fraction of the isophotal diameter with $h_r = 0.3R_{Gal}$. For this simple analysis we set $I_0 = 1$. We then input the position of each SN (R_{SN},z_{SN}) into Equation 2.2.17 along with their respective h_r and h_z to find $I(r, z)$. As a criterion, we consider a SN to be a runaway candidate if $I(r, z)$ is less than 0.01.

Face-on

Here we analyse the positions of SNae for the sample of face-on galaxies. We use a larger range of inclinations for this sample which introduces projection effects due to

[1] They also describe a "tail" of large scaleheights in their distribution.

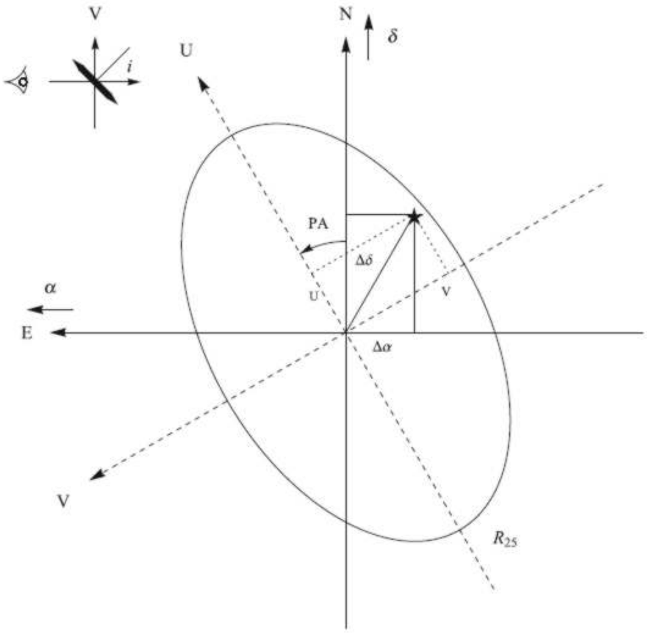

Figure 2.5: *To correct for the projection effects caused by the inclination of host galaxies the SNae are assume to have occurred in the plane of the disk and so a coordinate system, (U,V), in the plane of the disk is defined - U is aligned with the plane of the sky and the long axis of the galaxy and V is aligned with the plane of the disk and the short axis of the galaxy. Here △ α and △ δ relate to x and y offsets respectively. (Picture taken from Hakobyan et al., (2009).)*

the inclination of the host galaxy. In order to correct for the projection effects caused by inclined galaxies we follow the prescription of Hakobyan et al., (2009). Their method assumes that the SN occur in the plane of the disk, the likely birthplace of their progenitor stars - but as can be seen from the edge-on sample, they may not explode there (see Section 2.3.1). Firstly one defines the Cartesian coordinate system, (U,V) - see Figure 2.5, in the plane of the galaxy disk and relates it to the coordinate system on the plane of the sky - as used for the edge-on sample above. In terms of the (U,V) coordinate system, the SN is at

$$U = x\sin(PA) + y\cos(PA) \tag{2.2.18}$$

$$V = x\cos(PA) - y\sin(PA) \tag{2.2.19}$$

where again x and y are the offsets described in Table 2.1. The U-axis is aligned with the plan of the sky and the long axis of the galaxy while the V-axis is aligned with the plane and the short axis of the disk. The true radial distance of the SN from the centre of the host galaxy is then given by

$$R_{SN} = \sqrt{U^2 + \left(\frac{V}{\cos i}\right)^2} \tag{2.2.20}$$

where i is the inclination of the galaxy and R_{SN} is in arcseconds. A surface density profile is also constructed in order to extract the scalelength of the distribution. This is done by counting the number of SN in concentric annuli in the galaxy disk such that

$$\Sigma_j = n_j/\pi(r_{j+1}^2 - r_j^2) \tag{2.2.21}$$

where n_j is number of SN in the annulus with inner radius r_j and outer radius r_{j+1}.

Distances and Normalisation

The distances, D, to the host galaxies are easily found from the redshift, z. Here a value for the Hubble constant of H_0=74.2kms^{-1}Mpc^{-1} is used (Riess and Macri, 2007).

$$v = zc \quad ; \quad D = \frac{v}{H_0} \tag{2.2.22}$$

The values of R_{SN} and z_{SN} are converted to kpc using D and the isophotal diameter of the host galaxy d_{iso}. The diameter of the galaxy is

$$D_{Gal} = 10^{\log(d_{iso})} \text{ in units of 0.1 arcmins} \tag{2.2.23}$$

The radius of the host galaxy, R_{Gal}, is then used to normalise the radial distances of the SNae to the size of their host galaxy. The normalised distances are then denoted

$$R_N = \frac{R_{SN}}{R_{Gal}} \tag{2.2.24}$$

2.3 Results

2.3.1 Edge-on Sample

Plotting the positions of the SN about their host galaxy it is easily seen that some do occur well beyond the extent of the galaxy defined by the B_{25} isophotal diameter. It can be seen from Figures 2.6 and 2.7 that in most cases the SNae lie close to the disk (z_{SN} <1kpc) but that in some instances they clearly lie above it. The error bars associated with each point refer to the range of possible heights for each case as calculated in Section 2.2.2. The points with no error bars indicate those SNae that resided in perfectly edge-on systems. In order to derive the scaleheight,

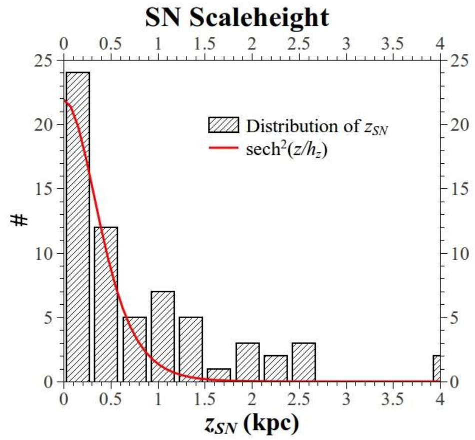

Figure 2.6: *The distribution of z_{SN} exhibits an sech^2 decay with a scaleheight of h_z = 0.486±0.081kpc.*

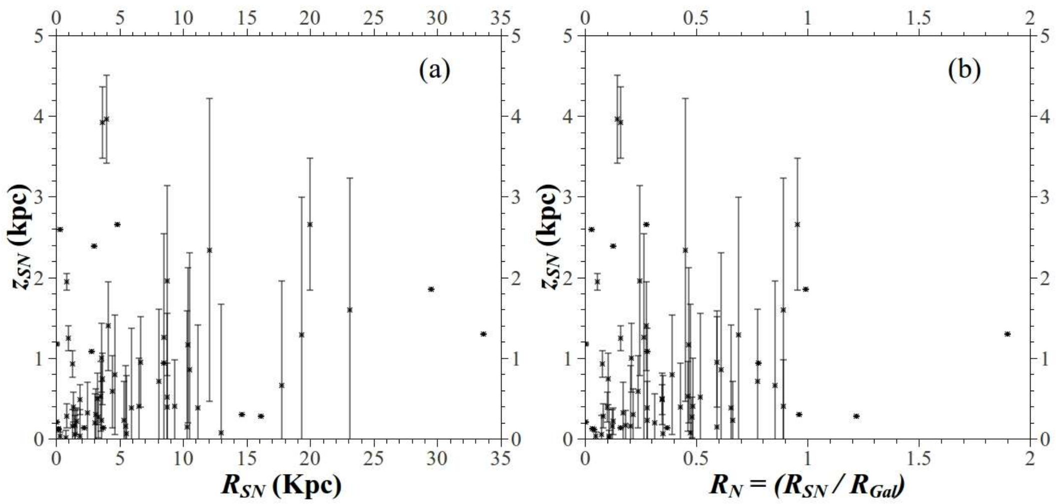

Figure 2.7: *For the edge-on sample the heights of the SNae above their host disks, z_{SN}, are calculated according to the prescription in Section 2.2.2. The error bars show the possible range of z_{SN} due to the inclinations of the host galaxy - those with no error bars occurred in perfectly edge-on galaxies. Figure (a) shows the heights as a function of distance along the plane, R_{SN}, in kpc while figure (b) shows the heights as a function of the normalised distance $R_N = R_{SN}/R_{Gal}$.*

h_z, of the density of SNae for this sample we find the populations of SNae in bins of 0.3kpc and then fit, with a scaled Levenberg-Marquardt algorithm[1], a sech^2 decay of

[1]This is implemented within the GNU QTIplot program

the form

$$\Sigma_z = \Sigma_0 \mathrm{sech}^2\left(\frac{z}{h_z}\right) \tag{2.3.1}$$

where Σ_0 is the central surface density. We find a scaleheight of $h_z = 0.486 \pm 0.081$kpc. The distribution (shown in Figure 2.6) does deviate from the sech^2 fit beyond 1kpc since the SNae in the sample resided in galaxies of many sizes (4.6< R_{Gal} <35.5kpc). It does show however that over half of the sample SNae lay within 0.6kpc of the $z =$ 0kpc plane which naturally follows from the concentration of OB stars to the disks of spiral galaxies.

We now look at each member of the sample individually by applying the method outlined above which defines a synthetic brightness distribution based on parameters about the host galaxy of each SN. A criterion ($I(r, z) < 0.01$) is applied to the brightness of the synthetic galaxy at (R_{SN},z_{SN}) to see if the SN could be considered a runaway candidate. From this method we extract nine runaway candidates from the sample of 64. Of the nine candidates, three reside in barred galaxies which deviate from the idealised brightness distributions and are rejected. The remaining six however do represent possible runaway candidates and are shown in Figure 2.8 with their corresponding $I(r, z)$ listed in Table 2.2.

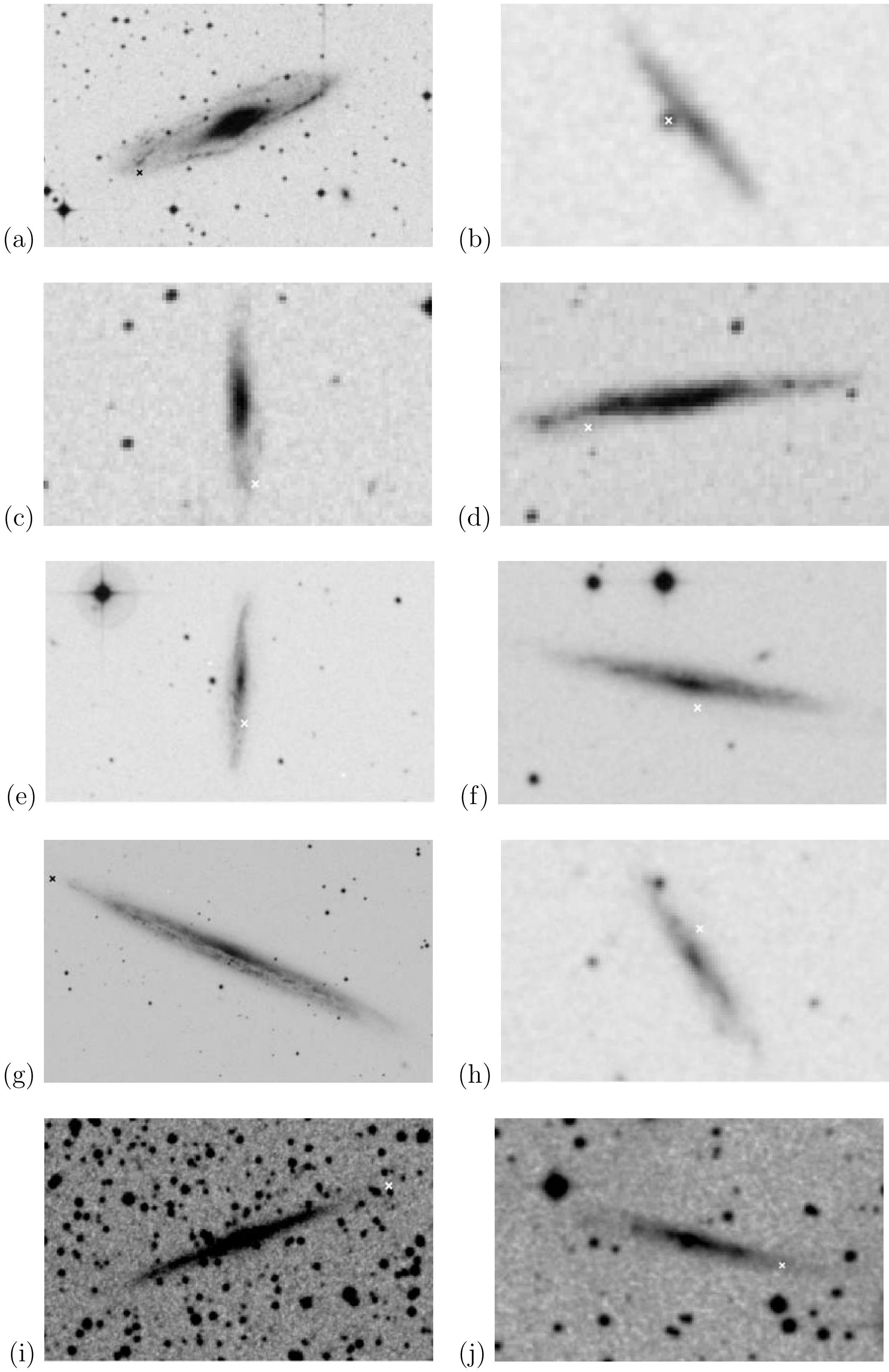

Figure 2.8: *From the method outlined above we extract 9 runaway candidates (3 are discarded due to an irregular host galaxy morphology), we include here 4 others that do not meet the criterion but have low $I(r, z)$. The point at which SN occurred is marked with black/white cross. Refer to Table 2.2 for the galaxy/SN designations and the calculated $I(r, z)$ for each case.*

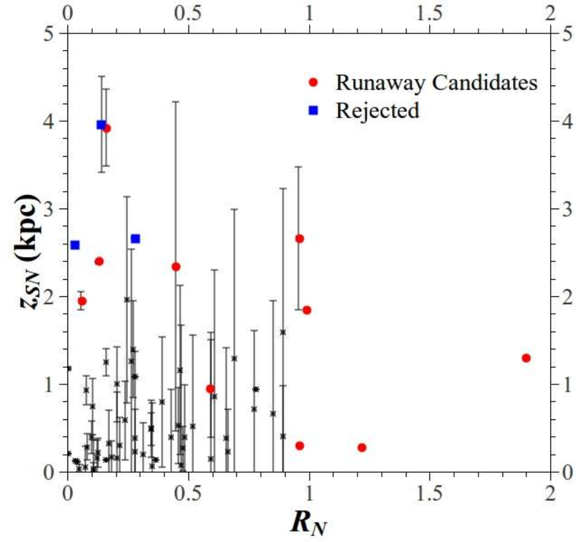

Figure 2.9: *The positions of the runaway candidates extracted from the photometric method along with four others with low $I(r, z)$ (red dots). Also depicted are the rejected candidates whose host galaxy deviated from the idealised brightness profile due to the presence of a bar (blue squares).*

	SN	Galaxy	$I(r, z)$
(a)	SN1992N	IC4831	0.68%
(b)	SN1988I	LEDA0086944	0.59%
(c)	SN2009gc	M-03-28-32	0.37%
(d)	SN2001dh*	M-06-44-26	2.61%
(e)	SN2005ab	NGC4617	0.95%
(f)	SN2003dr*	NGC5714	1.28%
(g)	SN1940A*	NGC5907	4.88%
(h)	SN2007ac	UGC10550	0.00%
(i)	SN2005da	UGC11301	0.04%
(j)	SN2004cr*	UGC11603	2.74%

Table 2.2: *Runaway candidates extracted from the photometric method outlined above along with four other candidates (marked with "*") who do not meet the selection criterion but have low $I(r, z)$. The candidates are listed with the designation of their host galaxy and the computed $I(r, z)$ for each case (as a percentage of the central surface brightness of the host galaxy).*

We also include in Figure 2.8 four other possible runaways (SN1940A in NGC5907, SN2003dr in NGC5714, SN2001dh in M-06-44-26 and SN2004cr in UGC11603) who do not meet the criterion above but nonetheless have small $I(r, z)$. Plotting the runaway candidates among the whole sample shows how effective this simple method is in separating SNae that are placed well away from the disk of their host galaxy (see Figure 2.9). These runaway candidates account for just over 15% of the initial sample suggesting that the observed and theoretical runaway populations of OB stars (Dray et al., 2005) has manifested itself in the distribution of CC SNae.

2.3.2 Face-on sample

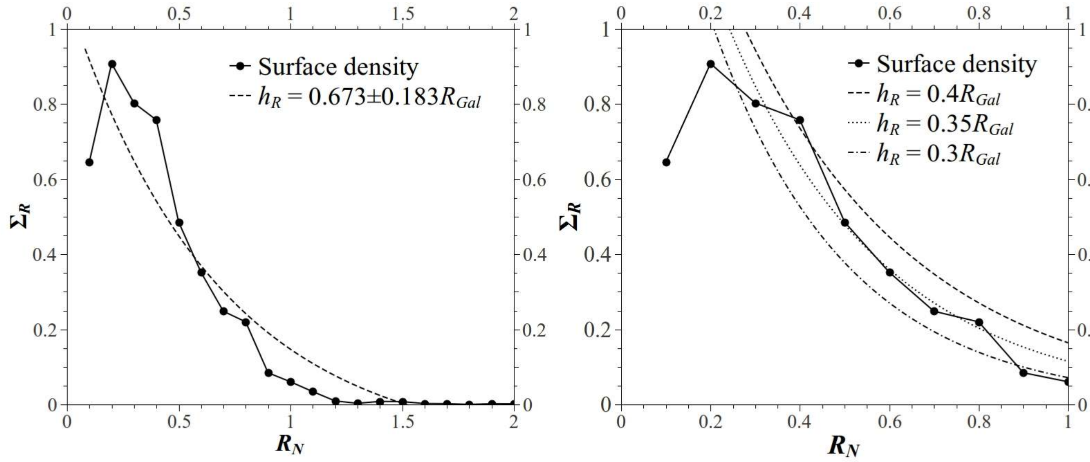

Figure 2.10: *A surface density profile is constructed for the face-on sample using the normalised inclination corrected radial distances. The profile exhibits a central deficit (discussed further on) with an exponential decay beyond R_N =0.2. Including the central deficit the scalelength of the distribution is h_R =0.67±0.18R_{Gal}. However, as an example we fit an exponentially decaying profile to the outer parts of the distribution with a scalelength in the range 0.3< h_R <0.4R_{Gal}.*

We construct surface density profiles according to Equation 2.2.21 for the face-on sample, firstly for the whole sample and then separately for the type Ib/c and type II SNae. We use the normalised de-projected radial distances and find that there is a clear deficit of SNae in the central regions of the host galaxies (Figure 2.10). The central regions of disk galaxies can be quite bright making the detection of SNae here more difficult since they may be confused with the bright central bulge and not noticed at all. This effect is more pronounced with more distant galaxies so that the more distant a galaxy is, the harder it is to notice a SN occurring in the central regions. An exponentially decaying curve is the fit to the distribution revealing a scalelength in the density distribution for type Ib/c/II SNae of h_R =0.67±0.18R_{Gal}. Because the host galaxies in this sample vary in size and shape the scalelength calculated here is not representative of any particular distribution of stellar population or brightness. The scalelength is however more representative of type II SNae since they account for over 75% (336 out of 444) of the sample. In an effort to account for the central deficit we also fit an exponential with a scalelength of 0.35±0.05R_{Gal} to the outer section of the sample (R_N >0.2).

Separating the sample into separate groups of type Ib/c and II it is shown in Figure 2.12 that SNae of type Ib/c tend to be more concentrated towards the centres of their host galaxy. Although the sample contains a host of galaxy morphologies the two groups are distributed similarly in Hubble type (see Figure 2.11) allowing a more direct comparison of their distribution. We fit the surface density distribution of type Ib/c SNae with a scalelength of $h_{R,Ib/c}$ =0.43±0.05R_{Gal} while the distribution of type II SNae is fit with a more extended scalelength of $h_{R,II}$ =0.75±0.08R_{Gal} (see Figure 2.12).

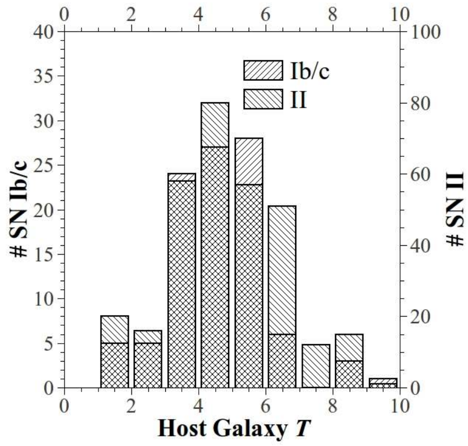

Figure 2.11: *Both groups of type Ib/c and II SNae are distributed similarly among their host galaxies.*

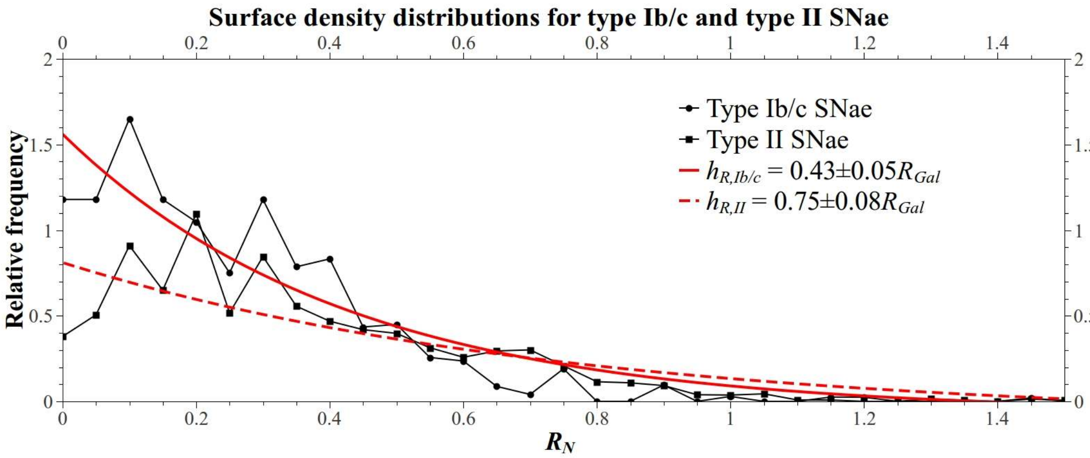

Figure 2.12: *Here shows the surface density distribution of both groups of SNae (type Ib/c and type II). The type Ib/c SNae are more centrally concentrated and are fit with an exponential decay with scalelength $h_{R,Ib/c}$ = 0.43±0.05R_{Gal}. The type II SNae display a more extended distribution and is fit with a scalelength $h_{R,II}$ = 0.75±0.08R_{Gal}.*

Shaw effect

For the SNae in the face-on sample (both type Ib/c and type II) we plot the surface density distributions of their de-projected radial distance for host galaxies that lie in distinct distance bins 0-50Mpc, 50-100Mpc, 100-150Mpc and 150Mpc+. The distributions are normalised to the number of SNae in each galaxy distance bin. It is apparent from these plots (Figure 2.13) that the distributions of radial distance for

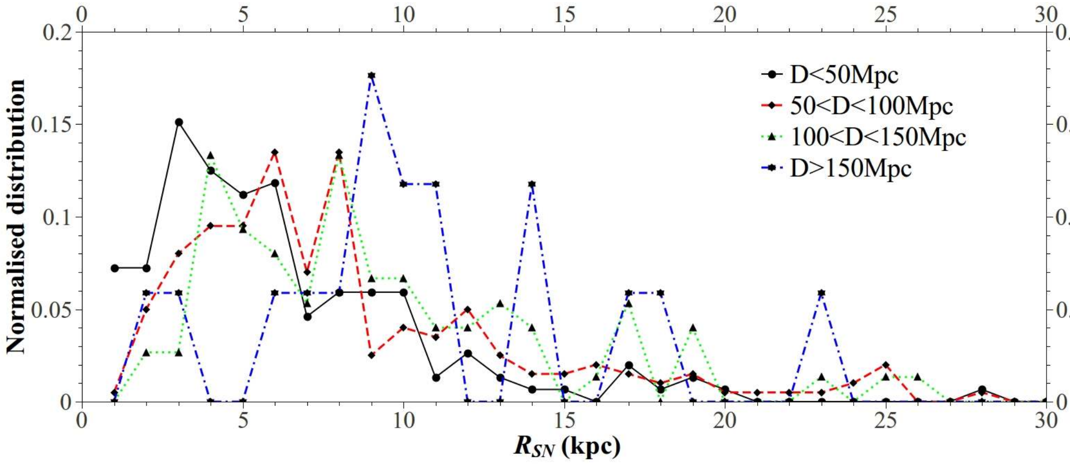

Figure 2.13: *With ever increasing host galaxy distances the central deficit in the distribution of radial distances becomes more pronounced. Shown here is the distribution for host galaxies with distance D <50Mpc (circles), 50< D <100Mpc (diamonds), 100< D <150Mpc (triangles) and D >150Mpc (stars).*

ever distant host galaxies exhibit larger deficits of CC SNae near the centres of the host galaxies with increasing galaxy distance. This effect was first shown by Shaw (1979) and is reproduced here with a sample almost twice as large (444 compared to 228). To ensure that this central deficit is not due to a physical lack of CC SN progenitors in the central regions of disks we also plot the surface density distribution of type Ia SNae. Type Ia progenitors should be distributed evenly about the disk and bulge of a galaxy and their abundance in the stellar halo should produce an overdensity in the central regions of disk galaxies since in these regions, assuming a homogeneous distribution throughout the halo, one would be looking through a greater volume of space which would contain a greater number of type Ia progenitors (see for eg. Baade (1944) or Wyse et al., (1997)). Indeed we find the same deficit, which is also more pronounce with host galaxy distance, implying that the selection effect due to the brightness of central bulges is also present in the case of CC SNae. Normalising the radial distances, R_{SN}, to the radius of the galaxy defined by the isophotal diameter appears to remove the increasing deficit of SNae with increasing host galaxy distance. This result suggests that the same fractional area of disk galaxies hide SNae due to bright central bulges, irrespective of host galaxy distance. Normalisation of radial distances to the isophotal radius of the host galaxy shows that the amount of disk area that obscures SN, preventing their discovery, is dependant only on the radius of the galaxy. From Figure 2.15 we see that obscuration begins to take effect at radial distances less than $0.4R_{Gal}$ implying that the central 16% of area in disk galaxies provides enough light to hide a SN.

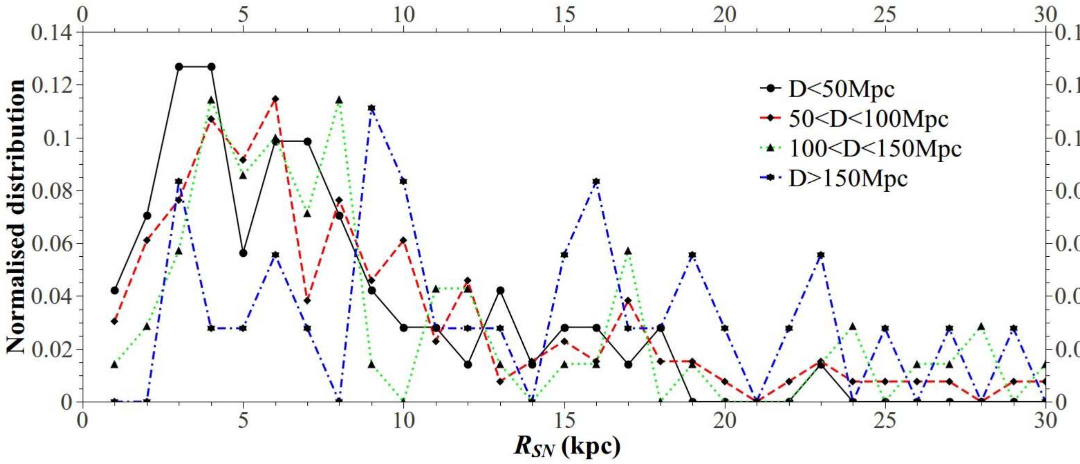

Figure 2.14: *In order to support the hypothesis that the deficit of SNae in the central regions of disk galaxies is caused by confusion with the bulge rather than there being a lack of CC SN progenitors in these regions we construct a similar radial distribution as a above for a sample of type Ia SNae. The progenitors of type Ia SNae are known to populate these inner regions yet with increasing galaxy distance the distributions exhibit similarly more pronounced central deficits.*

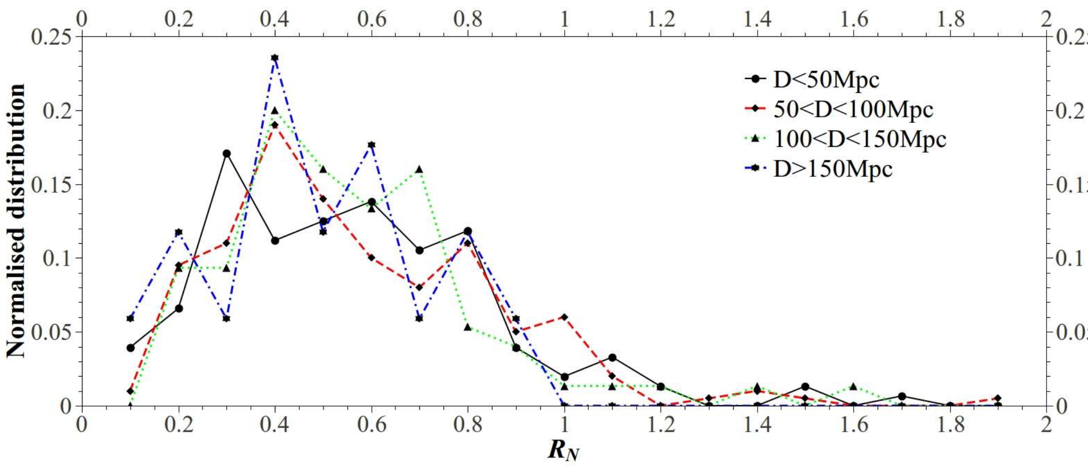

Figure 2.15: *Normalising the radial distances shows that, regardless of host galaxy distance, the same fraction of area in the host galaxy hides SN. At radial distances less than $0.4R_{Gal}$ SNae are less likely to be noticed.*

2.4 Discussion

From the Asiago SN database we have extracted a sample of sixty four Core-Collapse SNae that reside in edge-on (i>80°) spiral galaxies. We fit the distribution of the heights of the SNae with a sech ^{2} profile and a scaleheight of $h_z = 0.49 \pm 0.08$kpc. The host galaxies of the SNae from the sample ranged from Sa to Sd type galaxies with no real preference shown for any particular type although early type spirals are under-represented (see Figure 2.16). It should also be noted that only ten out of the sixty four SNae were of type Ib/c making the distribution almost entirely representative of type II SNae. The concentration of SNae to the disk of the host galaxies, with over half lying within 0.6kpc of the disk, is characteristic of the distribution of CC SN progenitors in galactic disks. The calculated scaleheight agrees well with the scaleheights of edge-on spirals derived from I-band photometry of Kregel et al., (2002) and indeed the scaleheight of the thin Milky Way disk of 0.3kpc (Jurić et al., 2008). Although the derived scaleheight fits well with other quoted values it is clear that in some instances the SNae appear completely detached from the host galaxy disk. It is thought that the progenitors of these wayward SNae had been ejected from their parent stellar cluster, by either a dynamical or SN event, and would be seen as “Runaway” stars with a high space velocity (Poveda et al., 1967; Blaauw, 1961; Hills, 1983). We develop a method, based on an idealised photometric profile galaxy disks, to separate this group of SNae from the others, who lie clearly within the disk of the host galaxy. Using this method we extract six possible candidates, with three rejected due to an odd host galaxy morphology. Another four had low $I(r, z)$ and could also be considered runaway candidates. From Figure 2.9 it can be seen that this method, which uses only readily available archival data, can reliably select SNae that are distinct from their host galaxy and whose progenitors may have been ejected from their likely birthplace in the disk. This method could be used to identify candidates worthy of a detailed spectroscopic follow up to ascertain abundances which may shed light on the binary evolution history of the progenitor.

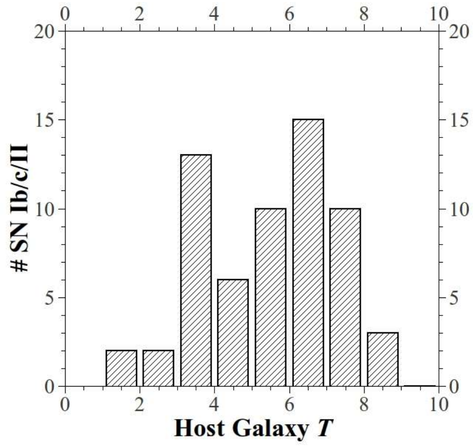

Figure 2.16: *The host galaxies in the edge-on sample exhibit no preference for Hubble type.*

For the face-on sample we have extracted a total of 444 CC SNae that are hosted in galaxies with inclinations less than 50°. We use the method of Hakobyan et al. (2009) to calculate the de-projected radial distance of the SNae from the centre of their host galaxy. A surface density distribution of the normalised (to the isophotal radius of the host galaxy) radial distances is then fit with an exponential profile with a scalelength of h_R =0.67±0.18R_{Gal}. The density distribution does show a truncation in the inner regions of the host galaxies ($R_{SN} < 0.4R_{Gal}$). A similar distribution for the case of type Ia SNae, the progenitors of which are known to populate the bulges of disk galaxies, implies type Ia SNae in these regions go undetected due to confusion with the bright bulges and that a similar effect also affects the detection of CC SNae. We also fit a scalelength to the outer ($R_{SN} > 0.4R_{Gal}$) part of the distribution in the range h_R =0.35±0.5R_{Gal}. The host galaxies, as in the case for the edge-on sample, range in size and shape (see Figure 2.11) and the derived scalelength is not representative of any particular galaxy type. When the sample is split into groups of type Ib/c and type II SNae, the density distribution of radial distances shows that the type Ib/c SNae are more concentrated towards the centres of their host galaxy. Although the host galaxies vary in Hubble type, the two groups are distributed similarly in T allowing a confident comparison (see Figure 2.12). The type Ib/c SNae are fit with a scalelength of $h_{R,Ib/c}$ =0.43±0.05R_{Gal} while the type II SNae are fit with a scalelength of $h_{R,II}$ =0.75±0.08R_{Gal}. This difference in scalelengths has been suggested to be due to the radial metallicity gradient in galaxy disks (eg. Boissier and Prantzos (2009)). The metal rich inner disk causes the massive OB stars to generate strong winds compared to the relatively metal poor OB stars in the outer disk. This mass loss removes Hydrogen from the CC SN progenitors resulting in an absence of Hydrogen in their spectra and consequently, their classification as type Ib/c type SNae.

We reproduce the Shaw effect (Shaw, 1979) with a sample twice as large to confirm a selection effect due to distance. As one investigates the radial distribution of SNae for ever distant host galaxies it is clear that the central deficit described above becomes more apparent (see Figure 2.13). This selection effect is due to confusion with bright bulges in spiral galaxies and the decreasing spatial resolution of telescopes with distance. Normalising the radial distances suggests that for all galaxies the same fractional disk area is bright enough to hide SNae, preventing their detection. Noting that in Figure 2.15 the inner truncation in the distribution occurs for galaxies in all distance bins at $<0.4R_{Gal}$ we estimate that the inner 16% of the area in galaxy disks is bright enough to obscure SNae, regardless of host galaxy distance.

Chapter 3

Modelling Runaways

3.1 Introduction

In this chapter we investigate the distributions of SNae, whose progenitors have been given a kick during the SN explosion of a former binary companion, by placing test particles in an axisymmetric potential and giving them a kick. The test particles are firstly distributed about a galaxy disk following the surface brightness profiles of observed spiral galaxies. These brightness profiles are parameterised by their respective scalelengths. The test particles are given a "kick" velocity which is added to their initial "systematic" velocity which is due to their position in the galactic potential. This kick velocity is based on observations of high velocity, or "runaway", OB stars and pulsars and varies from 30 to 150kms^{-1}. Each test particle is also assigned a mass which determines how long the particle will travel before exploding as a SN. Once the particle has exploded its position is noted and the distribution these positions is then fit with new scalelengths. This allows a measure of the dispersion from the initial distribution.

Also in this chapter we describe the routine with which we evaluate the trajectories of the test particles. We use a $5^{\text{th}}-$ and $6^{\text{th}}-$ order Runge-Kutta scheme, which is tested and evaluated, to reproduce the orbits. The gravitational potential is also described and is shown to produce a flat rotation curve. This aspect of the potential affords the model a certain consistency in that the test particles will, without any alterations, replicate the orbital characteristics of stars in any spiral galaxy.

3.2 Initial Distribution

The light profiles of disk galaxies form the basis of the initial distribution of test particles in this model. Along with input from mass models of the inner galactic disk, the light profiles serve to adequately distribute the test particles about an azimuthally homogeneous disk with a central hole. The spherical bulge is not included in our model since its constituents are population II stars and are not connected to the phenomenon being investigated here.

3.2.1 Distributions within the disk

Here the initial distribution of test particles is described. We define the distribution separately for each component of the cylindrical-polar coordinate system in which the particles reside. Once each of the R, z and ϕ components are populated they are then combined to give the full 3-dimensional distribution.

Radial Distribution

While radial light profiles of disk galaxies are well fitted by two component models (a central spheroidal bulge (Sersic, 1968; de Vaucouleurs, 1948) and an exponential disk (Freeman, 1970; Knapen and van der Kruit, 1991)) there still remains an ambiguity about the physical distribution of high mass stars in the inner regions of disk galaxies. Freeman (1970) also describes his Type II disk where the disk is truncated at small R showing a dip in surface brightness outside the central bulge. This inner truncation of galaxy disks has been observed in early type spiral galaxies by (Ohta et al., 1990) and dynamical models of the Milky Way have included disk density profiles described by the difference of two exponentials which creates a distribution with a central hole (Robin et al., 2003; Freudenreich, 1998). This central hole will be included when distributing our test particles as dynamical interactions with the central compact object described in our potential (Equation 3.3.2) may produce high velocity objects which are not the subject of study here ie. hyper velocity stars (Brown et al., 2005). Freudenreich (1998) describes a central hole in the Galactic centre which is truncated at R=3kpc but in our case, as we want to investigate all possible cases, we choose that the inner truncation is described by the difference of two exponentials - an exponential disk, with scalelength h_r, minus an exponential bulge with scalelength h_b.

Face-on galaxies are commonly modelled with light profiles consisting of two components - a spherical bulge described by a $R^{\frac{1}{4}}$ law (de Vaucouleurs, 1948) (or, more generally, a $R^{\frac{1}{n}}$ law where n is the Sérsic index (Sersic, 1968)) and an exponentially decaying disk (Knapen and van der Kruit, 1991). However, while the bulges of spiral galaxies are commonly modelled with Sérsic profiles it should be noted that bulges of spiral galaxies have been successfully described with exponential profiles (Andredakis et al., 1995). We derive h_b, the scalelength of the bulge, from the K-band effective radius (r_e, the radius containing half the total light due to the Bulge) observed for Sc-type galaxies by Graham and Worley (2008). We adopt an r_e value of 0.9kpc and a Sérsic index of n=1 (both of which lie in the observed ranges - r_e=$0.60\pm^{0.92}_{0.26}$kpc and n=$1.78\pm^{2.18}_{0.79}$). The Sérsic profile is parameterised by r_e and n and the equivalent exponential profile is parameterised by h_b and n and both can be equated as follows (Sersic, 1968);

$$I(r) = I_0 \exp\left[\left(\frac{-r}{h_b}\right)^{\frac{1}{n}}\right] = I_e \exp\left[k\left\{\left(\frac{r}{r_e}\right)^{\frac{1}{n}} - 1\right\}\right] \tag{3.2.1}$$

where k, a normalising factor, has been shown to be well approximated by $k = -(2n - 0.327)$ (see Equation A.1.2); $I(r)$ describes the surface brightness at r, I_0 is the central surface brightness and I_e is the surface brightness at r_e. It can be seen that for a Sérsic index of 1, the first equation in 3.2.1 describes a purely exponential falloff and by equating the equations one can deduce the relationship between h_b and r_e as

$$\left(\frac{r_e}{h_b}\right) = (2n - 0.327)^n \tag{3.2.2}$$

which gives in the case of n=1: $h_b = r_e/1.67 = 0.538$kpc.

We also use the B-band Sc-type disk scalelength, h_r=$3.37\pm^{1.66}_{0.88}$kpc, from Graham and Worley (2008) which is in good agreement with the median value in a photometric (r-band) study of face-on galaxies by Fathi et al. (2010). They also describe a bimodality in scalelengths with lower mass galaxies ($10^9 - 10^{10} M_\odot$) having an average scalelength of 1.52 ± 0.65 kpc and higher mass galaxies ($10^{10} - 10^{12} M_\odot$) having an average scalelength of 5.73 ± 1.94 kpc.

As mentioned above we model the distribution of test particles on the difference of two exponentials - an exponential bulge profile derived from a Sérsic profile taken from an exponential disk profile - to create a central hole in the distribution. This gives a function of the form

$$I(r) = I_0 \left[\exp\left(\frac{-r}{h_r}\right) - \exp\left(\frac{-r}{h_b}\right)^{\frac{1}{n}}\right] \tag{3.2.3}$$

where h_r and h_b are the scalelengths of the surface brightness of the disk and bulge respectively and n is the Sérsic index which we take to be equal to 1. A list of random numbers between 0 and 1 is generated (Set B_R containing numbers B_{Ri} where i goes from 1 - 10,000). These numbers relate to the area under the curve described by

$$A_R \left[\exp\left(\frac{-r}{h_r}\right) - \exp\left(\frac{-r}{h_b}\right) \right] \tag{3.2.4}$$

such that

$$B_{Ri} = \int_0^{R_i} A_R \left[\exp\left(\frac{-r}{h_r}\right) - \exp\left(\frac{-r}{h_b}\right) \right] dr. \tag{3.2.5}$$

In Equation 3.2.4 A_R is a constant, fixed so that the area under the curve of 3.2.5, integrated from 0 to R_{max} is equal to 1 (where R_{max} is the maximum extent of the disk). We tentatively set the maximum extent of the disk to be 15kpc - the average galaxy radius (using B_{25}-isophotal radii) in the sample of edge-on and face-on galaxies in Section 2.2 is 16.21kpc and 14.92kpc respectively. Kregel et al., (Kregel et al., 2002) argue that the radial truncation in disks does not occur until at least $4h_r$. Unfortunately there is no way to analytically evaluate R from Equation 3.2.5 so another method has been employed to extract the distribution. A simple script was written that implements Newtons method for 50 iterations. A first guess, R_n, was estimated and following values of R were calculated by

$$R_{n+1} = R_n - \frac{f(R_n)}{f'(R_n)} \tag{3.2.6}$$

where $f(R)$ is just Equation 3.2.5 rearranged with one side equal to zero: ie.

$$f(R) = \left(\int_0^{R_i} A_R \left[\exp\left(\frac{-r}{h_r}\right) - \exp\left(\frac{-r}{h_b}\right) \right] dr \right) - B_R \tag{3.2.7}$$

and $f'(R)$ is the derivative of Equation 3.2.7 with respect to R (a full derivation is outlined in Appendix A.1). This method proved quite successful as can be seen in Figure 3.1. Although quite a high proportion of test particles have a radial distance between 0kpc and 2kpc, only a small fraction are situated very close to the central compact object described in Equation 3.3.2 thereby significantly limiting the chance of strong gravitational encounters and consequently the production of hype-velocity stars (Brown et al., 2005).

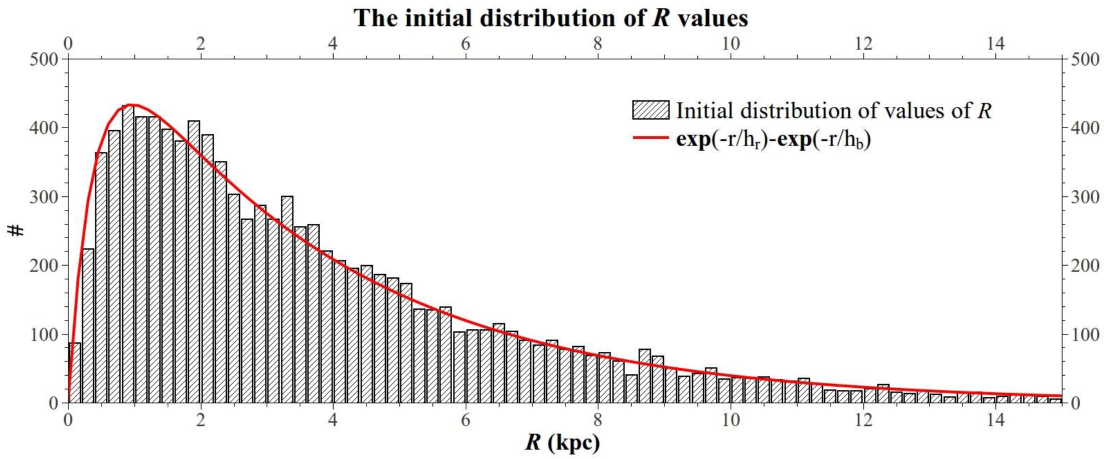

Figure 3.1: *For a model galaxy with a maximum extent of R_{max} = 15kpc this is the radial distribution of test progenitors produced by set B_{Ri}. We subtract an exponential bulge with scalelength h_b = 0.538kpc from an exponential disk scalelength of h_r = 3.37kpc. This distribution of values of R_i is produced by equation 3.2.5 and is overlain with a smooth plot of the function.*

Azimuthal Distribution

Now that each test particle has an R position, each needs to be distributed evenly around a disk. A set of random numbers (set B_ϕ containing random numbers between 0 and 1, $B_{\phi i}$, where i goes from 1 to 10,000) is then generated and used to position the test particles at certain angles, ϕ_i, around the disk. This operation is simply

$$\phi_i = B_{i\phi} \times 2\pi$$

Height Distribution

Height distributions of brightness in disk galaxies have been successfully modelled on sech^2 profiles of the form

$$I(z) = I_0 \mathrm{sech}^2\left(\frac{z}{h_z}\right) \tag{3.2.8}$$

where I is the surface brightness (I_0 the central surface brightness), z is the height above the disk, and h_z is the scaleheight of the surface brightness (van der Kruit and Searle, 1981; Mosenkov et al., 2010). High mass stars, the progenitors of SNae, are said to be located in the "thin disk" of spiral galaxies as opposed to the "thick disk" which contains older stars. These two disk components can be separated by analysing characteristics such as metallicity and velocity dispersions. Thin disk stars are said to formed by gas that has been accreted on to the galaxy and consequently exhibit similar galactic rotation speeds and abundances while the thick disk stars, said to be accreted on to the galaxy from satellite clusters or dwarf galaxies, exhibit a lower metallicity, higher z-velocity dispersions and tend to lag behind the rotation of thin disk stars (Yoachim and Dalcanton, 2006). This thin disk can be reasonably well described in the outer regions of disks by photometry of external galaxies (Yoachim and Dalcanton, 2006) and also by surveys of stars in the Solar neighbourhood (Jurić et al., 2008). We use the scaleheight, h_z, from Juric et al. (2008) of 300pc but note that we use a larger scalelength than theirs (2.6kpc) so as to include the possibility of high mass stars forming at the outer, often bright, regions of disks (Bush et al., 2010).

Another set of numbers, between 0 and 1, is generated (Set B_z containing numbers B_{zi} where i goes from 1 to 10,000) which corresponds to the height of each test particle in an analogous way to set B_R. Firstly the distribution is based on

$$B_{zi} = \int_{z_{min}}^{z_i} A_z \mathrm{sech}^2 \left(\frac{z}{h_z} \right) dz \tag{3.2.9}$$

where, in the same way as for the derivation of the values of R_i, A_z is a constant set so that the area under the curve of Equation 3.2.9 integrated from z_{min} to z_{max} is equal to 1. Again, as in the case for the derivation of R_i, we tentatively set a maximum/minimum height of the disk of 1kpc (or $3.33h_z$) so that $z_{min} = -z_{max}$. A full derivation is outlined in Section A.2 and gives a formula to determine the height above/below the disk for each test particle:

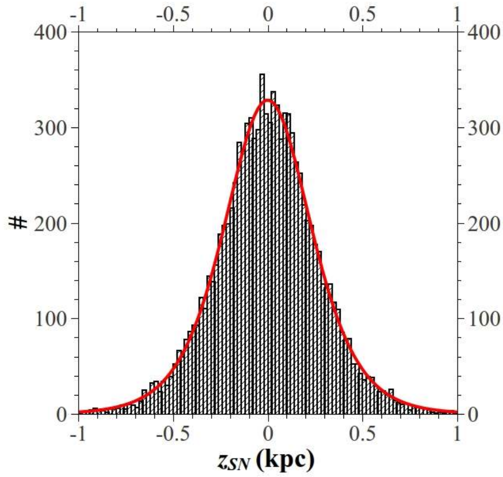

Figure 3.2: *The distribution of test particle heights as defined by Equation 3.2.10 overlain with a smooth plot of Equation 3.2.8. A large proportion lie within 500pc from the plane of the disk making it an extremely flat disk when compared to the radial distribution.*

$$z_i = \frac{h_z}{2} \ln \left[\frac{1 + \tanh\left(\frac{z_{max}}{h_z}\right)(2B_z - 1)}{1 - \tanh\left(\frac{z_{max}}{h_z}\right)(2B_z - 1)} \right] \tag{3.2.10}$$

In Figure 3.2 the distribution of the values of z_i is plotted. It can be seen that the vast majority of test particles have a height between -500pc and 500pc. To test the dependence of the final height distribution on the initial scaleheight we also run the model with different initial h_z. The distributions of these varying heights can be seen in Section 3.5.2.

Combining the initial distributions

For the case of a disk scalelength of $h_r = 3.37$kpc, a bulge scalelength of $h_b = 0.538$kpc, a maximum radial disk length of $R_{max} = 15$kpc, a disk scaleheight of $h_z = 0.3$kpc and a maximum disk height of $z_{max} = 1$kpc we present a graphical view of the initial distribution of test particles in Figure 3.3. The full initial distribution of test particles about a homogeneous disk is defined by

$$I(r,z) = A\left[\exp\left(\frac{-r}{h_r}\right) - \exp\left(\frac{-r}{h_b}\right)\right]\operatorname{sech}^2\left(\frac{z}{h_z}\right) \tag{3.2.11}$$

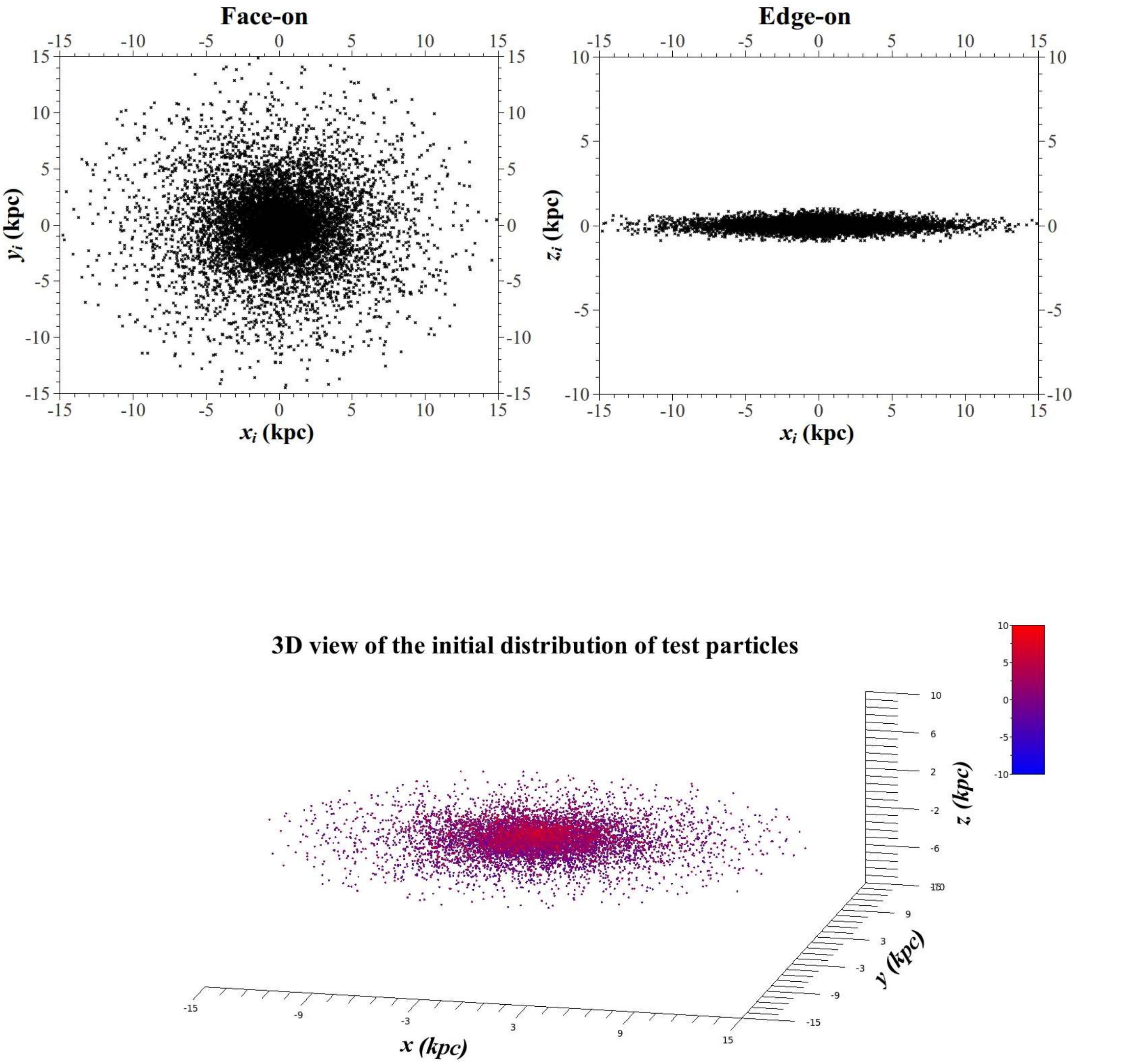

Figure 3.3: *For scalelengths h_r = 3.37kpc and h_b = 0.538kpc and a scaleheight of h_z = 0.3kpc an initial distribution test particles is shown above. The initial distribution of test particles, viewed edge-on, exhibits the familiar profile of late type disk galaxies.*

3.2.2 Velocity Kicks

Previous studies of the dynamics of OB populations have shown that the majority of OB stars have motions which follow those of the gas clouds from which they were formed, with a small dispersion ∼10kms^{-1}. These surveys use distances and radial/proper motion data, corrected for solar motion and galactic rotation, to discern the space velocities of these high mass stars (Blaauw, 1958; Stone, 1979; Gies, 1987). The distribution of the space velocities of OB stars has also shown an excess of higher velocity stars and when these are taken as a separate group (runaway stars - usually defined to be those with a space velocity ≥30kms^{-1} although some studies include those with a high distance from the galactic plane) they show a much higher velocity dispersion ∼30kms^{-1} (and higher space velocities) (Stone, 1991). These high velocities show that a proportion of these stars (∼10-30% of O-stars and 5-10% of B-stars (Gies, 1987; Stone, 1991)) undergo a process which not only ejects the star from its parent gas cloud but frequently unbinds the star from a previous binary companion (Mason et al., 1998; Gies and Bolton, 1986). There has been much debate about the nature of this mechanism with some suggesting a dynamical (ie. gravitational) three- or n-body origin (Poveda et al., 1967). The ejection mechanism we focus on is the one whereby the primary star in a binary system (the initially most massive) undergoes a SN event and imparts a velocity to the secondary star (the initially least massive), potentially unbinding the binary and sending the secondary out with a high space velocity due to a recoil experienced when SN ejecta leaves the system (a Binary Supernova Scenario, BSS) (Blaauw, 1961; Hills, 1983; Burrows et al., 1995). We investigate the disruption of such binaries in our population synthesis in Section 4.2. We do not use the population synthesis model to derive velocity kicks as the nature of asymmetric SNae is quite uncertain.

HIP	v_{space} (kms^{-1})
14514†	39.4
18614	64.9
38455	41.4
38518	31.1
42038	31.3
46950	32.1
48943	35.2
49934	31.2
57669	31.1
76013	69.0
81377*	23.5
82868	30.3
91599†	44.7
102274	46.1
109556*	74.0

Table 3.1: *Sample of confirmed BSS runaways reproduced from Hoogerwerf et al. (2001). Those marked with an "*" are known as the classical runaways whose parent cluster were known, those marked with a "†" have an uncertainty about their parent cluster which therefore presents an ambiguity as to their ejection mechanism. The average v_{space} is 41.68kms^{-1} and this sample is 63.3%±4.5% of the total sample with confirmed ejection mechanism (BSS or DES).*

A criterion for the breakup of a system via this mechanism requires that more than half the mass of the system is ejected in the process, however, an asymmetric SN explosion increases the chances of binary separation by lowering the amount of ejected matter needed for disruption (Hills, 1983; Burrows et al., 1995). The binary fraction among runaway OB stars is low (∼10%) compared to the "normal" population of OB stars (≥50%) however an example of SNae in undisrupted binary systems is high mass X-ray binaries (HMXBs) which are often found to have high space velocities 50kms^{-1} (Kaper et al., 1997; van den Heuvel et al., 2000). Our distribution of velocity kicks (v_{kick}) is partly based on observations of high velocity early-type stars. Hoogerwerf et al. (2001) use milli-arcsecond Hipparcos astronomy to retrace the path of known runaway stars and describe a range of velocities for confirmed BSS runaways of between 30-75kms^{-1} (A full list of the confirmed BSS runaways is reproduced from Hoogerwerf et al. (2001) in Table 3.1). The velocities of the sample in Table 3.1 only describe a limited selection according to Martin (2006) who suggests that runaways can have ejection velocities much greater than 100kms^{-1}. Asymmetric neutrino emission has been shown to provide a mechanism that could impart a velocity kick to neutron stars of ≈1000kms^{-1} (Kotake et al., 2003; Kusenko and Segrè, 1996; Scheck et al., 2004), other sources of velocity include an electromagnetic rocket effect (Tademaru and Harrison, 1975) and to a lesser extent, convective instabilities in a compact stellar core. The distribution of observed pulsar velocities has traditionally been described as having two Gaussian components centred on 90kms^{-1} and 500kms^{-1} (Arzoumanian et al., 2002) but more recently it has been described as a Maxwellian with a mean velocity of ≈400kms^{-1} with σ = 265kms^{-1} (Hobbs et al., 2005). Assuming a neutron star mass of 1.4M$_{\odot}$ and neglecting the ejection of a SN shell, conservation of momentum would suggest that a 7M$_{\odot}$ star (a lower limit for CC SN progenitors) would gain a speed of ≈200kms^{-1} if the neutron star receives a natal kick of ≈1000kms^{-1}. Since the observed number of runaways with a confirmed ejection mechanism is quite low (with low space velocities) we set the distribution of velocity kicks imparted to our test particles to be centered at 90kms^{-1} with a dispersion of σ = 60kms^{-1} so as to include a range of possible velocities. The velocity kicks are given a t-distribution (used when there is a only a small sample of known

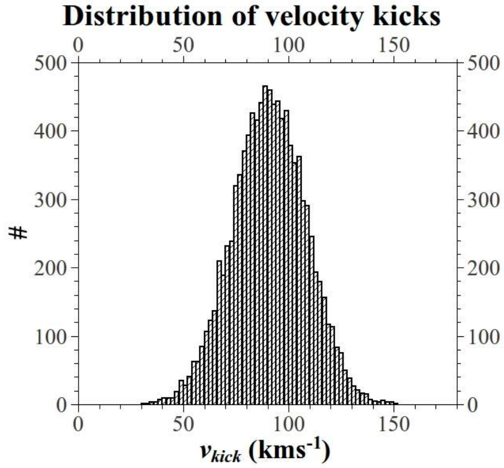

Figure 3.4: *Since the number of space velocities of known BSS runaways is quite low (Hoogerwerf et al., 2001) we use a t-distribution to assign each of our test particles a velocity. We centre the distribution at 90kms^{-1} with σ=30kms^{-1} so that a good range of velocities is covered.*

values). The t-distribution produced in *Octave*[1] is centred on 0 and extends from -3.78 to +3.78 (due to the way the program runs). All values are then shifted to the right so that they are positive by adding 3.78. The numbers are then multiplied by 120/7.56 since the width of the velocity dispersion is 120kms^{-1} (ie. 2σ) and the final step is to then add 30 to each number so that the distribution is centred on 90kms^{-1} and extends from 30kms^{-1} to 150 kms^{-1} (Figure 3.4).

3.2.3 Stellar masses

We assume that the test particles have undergone a period of mass transfer during their binary evolution and have therefore been "rejuvenated" to a zero age main sequence (ZAMS) star. The masses of the test progenitors, M_i, range from $M_{min} =$ 10 to $M_{max} = 100M_\odot$ and their distribution, $\Theta(M_i)$, follows the formulation of Bethe & Brown (1998) such that

$$\Theta(M) \propto M_i^{-1.5} \tag{3.2.12}$$

A set of random numbers, B_M, is again generated and each element is equated to the area under the curve of 3.2.12 integrated from 0 to M_i. This gives a function which determines the mass of each of the test particles:

$$B_{Mi} = A_M \int_{M_{min}}^{M_i} M^{-2.5} dM \tag{3.2.13}$$

where A_M is a constant which sets Equation 3.2.12, integrated from 10 to $100M_\odot$, equal to one. Following the derivation in Section A.3 the stellar mass for each test particle is calculated from

$$M_i = \left\{B_{Mi}\left[M_{max}^{-1.5} - M_{min}^{-1.5}\right] + M_{min}^{-1.5}\right\}^{\frac{1}{-1.5}} \tag{3.2.14}$$

From the stellar masses the main sequence stellar lifetimes, τ_{MS}, are deduced from the formula of Belczyński and Bulik (1999):

$$\tau_{MS}(M) = 20 \times 10^6 \left(\frac{M}{10M_\odot}\right)^{-2} \text{ yr} \tag{3.2.15}$$

where M is in solar masses. We then assume that the duration of the giant phase of the stars evolution is $0.2\tau_{MS}$. When a period of $1.2\tau_{MS}$ has elapsed the position of the test particles are noted - these positions make up the final distributions described in Section 3.5.

[1] A high level interpreted language similar to *MatLab* - see http://www.gnu.org/software/octave/

3.3 The Potential

In order to examine the dynamics of runaway SNae in a realistic way, the test particles are situated in a gravitational potential that takes into account the well observed kinematics of stars in disk galaxies. The rotation curves of disk galaxies show that stars in the disk orbit the galactic centre at a speed which is almost constant over most of the disk. A simple galactic potential which replicates this behaviour has been described by Flynn et al., (1996) and is adopted for this study. This potential includes components due to the disk, the bulge/stellar halo, a dense central component and a dark halo and is described further on.

3.3.1 Description of potential

Flynn et al. (1996) describe a gravitational potential (per unit mass) which corresponds to observed Galaxy parameters such as its rotation curve, local density and disk scalelength. The potential, $\Phi(R, z)$, is composed of three main parts: Φ_H due to the dark halo, Φ_C due to the central component and Φ_D due to the disk. The central component comprises of a term for a dense central object and a bulge/stellar halo. The disk component is made up of three Miyamoto-Nagai potentials (Miyamoto and Nagai, 1975) which together describe a disk (with a central hole) that also satisfy measurements of the local density and reproduces a scalelength that is consistent with observation. The potential due to the dark halo is spherical and is described as

Parameter	Value
V_H	220kms^{-1}
r_0	8.5kpc
M_{C1}	3.0×10^{9}M$_{\odot}$
M_{C2}	1.6×10^{10}M$_{\odot}$
r_{C1}	2.70kpc
r_{C2}	0.42kpc
M_{D1}	6.6×10^{10}M$_{\odot}$
M_{D2}	-2.9×10^{10}M$_{\odot}$
M_{D3}	3.3×10^{9}M$_{\odot}$
a_1	5.81kpc
a_2	17.43kpc
a_3	34.86kpc
b	0.30kpc

Table 3.2: *Values of the parameters used in Equations 3.3.1, 3.3.2 and 3.3.3*

$$\Phi_H = \frac{1}{2} V_H \ln(R^2 + z^2 + r_0^2) \tag{3.3.1}$$

where V_H is the rotational velocity at a large distance from the core radius r_0 (values shown in Table 3.2). The potential of the central component is described as

$$\Phi_C = \frac{-GM_{C1}}{\sqrt{(R^2 + z^2) + r_{c1}^2}} - \frac{GM_{C2}}{\sqrt{(R^2 + z^2) + r_{C2}^2}} \tag{3.3.2}$$

where G is the gravitational constant, M_{C1} and r_{C1} denote the mass and core radius of the bulge/stellar halo and M_{C2} and r_{C2} are the mass and core radius of the compact central component. The disk is represented by a function of the form

$$\Phi_D = \sum_i^3 \frac{GM_{Di}}{\sqrt{R^2 + [a_i + \sqrt{z^2 + b^2}]^2}} \tag{3.3.3}$$

The constants a_i and b relate to the scalelengths and scaleheight of each of the disk components, each having a total mass M_{Di}, respectively. The total potential per unit mass is then just the sum of each of the above;

$$\Phi(R, z) = \Phi_H + \Phi_C + \Phi_D \;\; \mathrm{m^2 s^{-2}} \tag{3.3.4}$$

Together the components of the potential create a flat rotation curve for the model galaxy (Figure 3.5). A circular rotation curve of the galactic plane is constructed by noting that

$$\nabla\Phi(R) = \ddot{R} - R\dot{\phi}^2 \tag{3.3.5}$$

giving;

$$\dot{\phi} = \sqrt{\frac{-\nabla\Phi}{R}}$$

since for circular rotation $\ddot{R} = 0$. Following the derivation in A.4.2 this gives the function for the circular speed, $\dot{\phi}_c$

$$\dot{\phi}_c = \left[\frac{V_H^2}{(r^2 + r_0^2)} + \sum_{i=1}^{2} \frac{GM_{Ci}}{(r^2 + r_{Ci}^2)^{\frac{3}{2}}} + \sum_{i=1}^{3} \frac{GM_{Di}}{(R^2 + A_{Di}^2)^{\frac{3}{2}}} \right]^{1/2} \tag{3.3.6}$$

3.4 Runge-Kutta-Fehlberg Method for Stellar Orbits

Simple numerical methods like a direct summation need a small timestep to be moderately accurate and are therefore computationally intensive and time consuming. Runge-Kutta methods offer a good solution since they apply a straight-forward procedure, produce an estimation of the local truncation error (at each iteration) and can be integrated into an adaptive method that keeps the local errors within certain predefined limits by altering the step size. In this example we use the RKF (Runge-Kutta-Fehlberg) scheme, which uses a fifth- and sixth-order method to give local

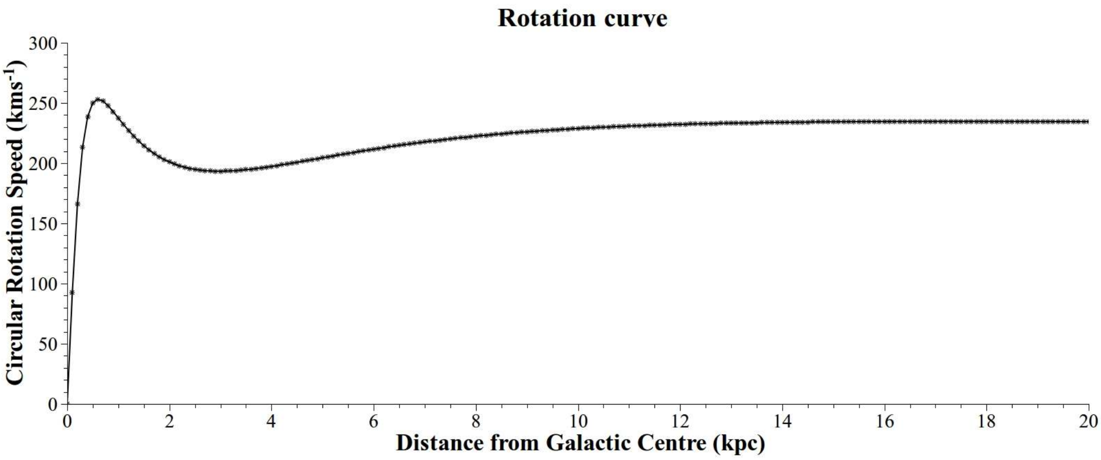

Figure 3.5: *The rotation curve, in the $z = 0$kpc plane, which is determined by the potential 3.3.4. At the solar radius, $R_{\odot} = 8$kpc, the rotational velocity is $\sim$220kms^{-1} which is consistent with Galactic mass models (Dehnen and Binney, 1998) but is slightly lower than recent observational measurements (Reid et al., 2009).*

truncation errors accurate to a fifth order Taylor expansion, to reproduce a simple orbit. This method is then applied to the main models described in this thesis - the dynamics of high velocity SN progenitors and the dispersion of HMXBs from spiral arms in disk galaxies. We describe here a brief synopsis of the method but refer the reader to Butcher (2003) for an extensive review.

3.4.1 Runge-Kutta Methods

Runge-Kutta (RK) methods are used to numerically solve initial value problems of the type

$$\begin{aligned} y' &= f(t, y) \\ y(t_0) &= y_0 \end{aligned} \tag{3.4.1}$$

where y', equal to some function $f(t, y)$, is the time derivative of y and y_0 is the value of y at $t = 0$. If a particle has some position y, then y' is the particles velocity. If the velocity of the particle is some function of time and/or position, $f(t, y)$ (due to some external force eg. gravity), then there is some error when calculating the particles position after some increment of time, h, by

$$y_1 = y_0 + hy' \tag{3.4.2}$$

since this assumes that the velocity is constant over the time interval h. Runge-Kutta methods attempt to reduce this error by using a velocity which is a weighted average of the velocities at different points during the timestep (eg. it could be an average of the velocities at $h = 0, h/4, h/2$ and h). The points at which the velocities are worked out and the weightings that each one is given are defined in an array of values known as a *Butcher Tableau*. A *Butcher Tableau* can have any size but as more intermediate velocities are used the accuracy of each new position increases. The number of these velocities that are used define the *order*, i, of the RK method. These velocities, which are to be averaged, are represented below as the k-coefficients (see Equation 3.4.4) and the weightings they are given in the averaging process are defined by the b values in the table which defines any fourth order RK method below.

$$\begin{array}{c|cccc} c_1 & a_{11} & a_{12} & a_{13} & \\ c_2 & a_{21} & a_{22} & a_{23} & \\ c_3 & a_{31} & a_{32} & a_{33} & \\ c_4 & a_{41} & a_{42} & a_{43} & \\ \hline & b_1 & b_2 & b_3 & b_4 \end{array}$$

The points at which the velocities are worked out are defined by the a and c coefficients such that

$$k_i = f(t_n + c_i h, y_n + \sum_{j=1}^{i-1} a_{ij} h k_j) \tag{3.4.3}$$

which gives for this fourth order method

$$\begin{aligned} k_1 &= f(t_n + c_1 h, y_n) \\ k_2 &= f(t_n + c_2 h, y_n + a_{21} h k_1) \\ k_3 &= f(t_n + c_3 h, y_n + a_{31} h k_1 + a_{32} h k_2) \\ k_4 &= f(t_n + c_4 h, y_n + a_{41} h k_1 + a_{42} h k_2 + a_{43} h k_3) \end{aligned} \tag{3.4.4}$$

Notice that for the method to be consistent $\sum_{j=1}^{i-1} a_{ij}$ must be equal to c_i for i = 2,3,4 since the function $f(t, y)$ at $t_n + ch$ must correspond to the function at $y_n + \Sigma ahk$. Once all of the velocities, or k-coefficients, have been evaluated then it is possible to to get the weighted average and, in turn, work out the particles position by

$$y_{n+1} = y_n + h \sum^{i} b_i k_i \tag{3.4.5}$$

which for this fourth order method gives

$$y_{n+1} = y_n + h(b_1 k_1 + b_2 k_2 + b_3 k_3 + b_4 k_4) \tag{3.4.6}$$

$$\begin{array}{c|cccc} 0 & 0 & 0 & 0 & 0 \\ \frac{1}{2} & \frac{1}{2} & 0 & 0 & 0 \\ \frac{1}{2} & 0 & \frac{1}{2} & 0 & 0 \\ 1 & 0 & 0 & 1 & 0 \\ \hline & \frac{1}{6} & \frac{1}{3} & \frac{1}{3} & \frac{1}{6} \end{array}$$

Table 3.3: *A Butcher tableau for a fourth order RK method.*

As an example, a particular fourth-order RK method for the numerical solution to the initial value problem above (Equation 3.4.1) has the tableau which has the solution

$$y_{n+1} = y_n + \frac{h}{6}(k_1 + 2k_2 + 2k_3 + k_4) \tag{3.4.7}$$

and k-coefficients

$$\begin{aligned} k_1 &= f(t_n, y_n) \\ k_2 &= f(t_n + \frac{h}{2}, y_n + k_1\frac{h}{2}) \\ k_3 &= f(t_n + \frac{h}{2}, y_n + k_2\frac{h}{2}) \\ k_4 &= f(t_n + h, y_n + k_3 h) \end{aligned} \tag{3.4.8}$$

3.4.2 Applying methods to Orbits

This method must be slightly changed since numerically solving orbits involves second order differential equations. In this case we use polar coordinates in which the potential is a function of r only, i.e.

$$\Phi(r) = \frac{GMm}{r} \tag{3.4.9}$$

and the force is

$$\nabla\Phi(r) = -\frac{GMm}{r^2} = \text{ mass} \times \text{acceleration} \tag{3.4.10}$$

giving the acceleration in the r-direction, a_r,

$$a_r = -\frac{GM}{r^2} \tag{3.4.11}$$

which in polar coordinates is

$$a_r = \ddot{r} - r\dot{\theta}^2 \tag{3.4.12}$$

This gives

$$\ddot{r} = -\frac{GM}{r^2} + r\dot{\theta}^2 \tag{3.4.13}$$

This second order differential equation can be expanded into two first order equations that will describe the motion in the potential

$$\dot{v_r} = a_r \tag{3.4.14}$$

$$\dot{r} = v_r \tag{3.4.15}$$

The solutions to these equations follow the same method as above except that the k coefficients for each solution must be evaluated in turn such that the second k coefficient for Equation 3.4.14 (k_{2v}) relies on the first k coefficient of Equation 3.4.15 (k_{1r}) and vice-versa. The first coefficients, k_{1v} and k_{1r}, are simply the initial acceleration and velocities respectively. The k_{iv} coefficients have units of ms^{-2} and the k_{ir} coefficients have units of ms^{-1}. The solutions for the fourth order RK method can be found below;

$$\begin{aligned} v_{n+1} &= v_n + \frac{h}{6}(k_{1v} + 2k_{2v} + 2k_{3v} + k_{4v}) \\ r_{n+1} &= r_n + \frac{h}{6}(k_{1r} + 2k_{2r} + 2k_{3r} + k_{4r}) \end{aligned} \tag{3.4.16}$$

where the coefficients are as follows

$$\begin{aligned} k_{1v} &= a(t_n, r_n) - \text{i.e. the acceleration at } r_n \\ k_{2v} &= a(t_n + \frac{h}{2}, r_n + k_{1r}\frac{h}{2}) - \text{i.e. the acceleration at } r_n + k_{1r}\frac{h}{2} \\ k_{3v} &= a(t_n + \frac{h}{2}, r_n + k_{2r}\frac{h}{2}) \\ k_{4v} &= a(t_n + h, r_n + k_{3r}h) \\ \\ k_{1r} &= v(t_n, r_n) - \text{i.e. the velocity at } r_n \\ k_{2r} &= v(t_n + \frac{h}{2}, r_n) + k_{1v}\frac{h}{2} - \text{i.e. the velocity at } r_n \text{ plus the velocity from } k_{1v}\frac{h}{2} \\ k_{3r} &= v(t_n + \frac{h}{2}, r_n) + k_{2v}\frac{h}{2} \\ k_{4r} &= v(t_n + h, r_n) + k_{3v}h \end{aligned} \tag{3.4.17}$$

Notice that the coefficients need to be evaluated alternately and that both solutions follow the *Butcher Tableau* (Table 3.3).

3.4.3 RKF Orbits

The method outlined above can be easily implemented for any higher order method once the appropriate *Tableau* has been obtained. For our simulation of a simple orbit we use the extended Butcher Tableau which has two solutions (two rows of b's), one of order five (which is accurate to a fourth order Taylor series expansion) and one of order six (which is accurate to a fifth order Taylor series expansion). This allows us to evaluate the local truncation error for each iteration which can be used to to alter the time-step and keep within a predefined error tolerance.

The extended Butcher Tableau for our method was developed by Fehlberg (1969) and is defined by

$$
\begin{array}{c|cccccc}
0 & & & & & & \\
1/4 & 1/4 & & & & & \\
3/8 & 3/32 & 9/32 & & & & \\
12/13 & 1932/2197 & -7200/2197 & 7296/2197 & & & \\
1 & 439/216 & -8 & 3680/513 & -845/4104 & & \\
1/2 & -8/27 & 2 & -3544/2565 & 1895/4104 & -11/40 & \\
\hline
 & 25/216 & 0 & 1408/2565 & 2197/4104 & -1/5 & \\
 & 16/135 & 0 & 6656/12825 & 28561/56430 & -9/50 & 2/55
\end{array}
$$

where the bottom two lines give the fifth and sixth order results (y_{n+1} and y'_{n+1}). The local truncation error is then calculated as

$$\epsilon = |y_{n+1} - y'_{n+1}| \tag{3.4.18}$$

If ϵ_{tol} is a desired accuracy and β is some safety factor that controls how the time-step changes, then the optimum time-step, h_{opt}, can be evaluated by

$$h_{opt} = \begin{cases} \beta h \left(\dfrac{\epsilon_{tol}}{\epsilon}\right)^{0.2} & , \epsilon \geq \epsilon_{tol} \\ \beta h \left(\dfrac{\epsilon_{tol}}{\epsilon}\right)^{0.25} & , \epsilon \leq \epsilon_{tol} \end{cases}$$

3.4.4 Example application of an RKF method

In order to begin the orbit simulation the orbiting body must be given some initial values. These include the distance from the mass about which it orbits, r_n, the angle of the starting point, θ, which for simplicity is taken to be zero, the velocity in the

r-direction, v_r, and the velocity in the θ-direction, v_θ. For an example of a simple circular orbit we take the case of the Earth orbiting the Sun - the radial velocity is zero and the orbital velocity (in $rads^{-1}$) is just 365 days (in seconds) divided by 2π. The radial distance is taken to be 1AU (1.496×10^{11}m) and from this we can define the initial specific angular momentum, P

$$P = r^2 v_{\theta,1} \tag{3.4.19}$$

where subscript 1 refers to the initial velocity (ie. at $r_{n,1}$ - subsequent subscripts, 2, 3+, refer to the rotational velocity at $r_{n,2}$ etc.). The first task is to calculate the k-values defined above which in this case ultimately depend only on different values of r. The first is

$$k_{1v} = a(r_n) \tag{3.4.20}$$

which is simply derived from our initial values (see Equation 3.4.13)

$$k_{1v} = -\frac{GM}{r_n^2} + r_{n,1} v_{\theta,1}^2 \tag{3.4.21}$$

We also have k_{1r} from our initial values which is simply the initial radial velocity

$$k_{1r} = v(r_n) = v_{r_{n,1}} = 0 \ \text{ms}^{-1} \tag{3.4.22}$$

k_{1r} can now be used to evaluate k_{2v}, or, more precisely, the radial acceleration at $r_{n,2} = r_n + k_{1r}\frac{h}{4}$ (or $r_n + k_{1r}ha_{21}$ following the extended Butcher Tableau). For consistency we also evaluate the orbital velocity at this new value of r, $v_{\theta,2}$ from the angular momentum we defined earlier

$$v_{\theta,2} = \frac{P}{(r_n + k_{1r}\frac{h}{4})^2} = \frac{P}{r_{n,2}^2} \tag{3.4.23}$$

giving

$$\begin{aligned} k_{2v} &= -\frac{GM}{(r_n + k_{1r}\frac{h}{4})^2} + (r_n + k_{1r}\frac{h}{4})v_{\theta,2}^2 \\ &= -\frac{GM}{r_{n,2}^2} + r_{n,2}v_{\theta,b}^2 \end{aligned} \tag{3.4.24}$$

Now the next coefficient is worked out

$$k_{2r} = v_{r_n} + k_{1v}\frac{h}{4} \tag{3.4.25}$$

from which we get the new value of r

$$r_{n,3} = r_n + h(k_{1r}\frac{3}{32} + k_{2r}\frac{9}{32}) \tag{3.4.26}$$

Then

$$k_{3v} = -\frac{GM}{r_{n,3}^2} + r_{n,3}v_{\theta,3}^2 \tag{3.4.27}$$

where $v_{\theta,3}$ has been calculated from the angular momentum and the new r. This process is followed until all the required k-coefficients have been evaluated and which are then used in the following equations to compute the next values: r_{n+1}, θ_{n+1}, $v_r(r_{n+1})$ and $v_\theta(r_{n+1})$.

$$\begin{aligned}
r_{n+1} &= r_n + h(k_{1r}b_1 + k_{2r}b_2 + k_{3r}b_3 + k_{4r}b_4 + k_{5r}b_5) \\
\theta_{n+1} &= \theta_n + h(v_{\theta,a}b_1 + v_{\theta,b}b_2 + v_{\theta,c}b_3 + v_{\theta,d}b_4 + v_{\theta,e}b_5) \\
v_{r_{n+1}} &= v_{r_n} + h(k_{1v}b_1 + k_{2v}b_2 + k_{3v}b_3 + k_{4v}b_4 + k_{5v}b_5)
\end{aligned}$$

and the new orbital velocity is

$$v_{\theta,n+1} = \frac{P}{r_{n+1}^2} \tag{3.4.28}$$

This gives us the next set of values from which we can proceed with the next iteration. In order to evaluate an error for this iteration we calculate the sixth order values of r_{n+1}, r'_{n+1}, by using the b' values from the extended Butcher Tableau (the very bottom line)

$$r'_{n+1} = r_n + h(k_{1r}b'_1 + k_{2r}b'_2 + k_{3r}b'_3 + k_{4r}b'_4 + k_{5r}b'_5 + k_{6r}b'_6) \tag{3.4.29}$$

which gives a local truncation error of

$$\epsilon = |r_{n+1} - r'_{n+1}| \tag{3.4.30}$$

The time step can then be altered following the method outlined above.

All of this may seem redundant in the case of a perfectly circular orbit since the only parameter to change is θ, but by altering the initial values of v_r or v_θ it is possible to simulate elliptical orbits which obey the laws of orbital mechanics. Once a program has been written it is then a simple task to alter the initial conditions and in order to simulate orbits in a more complex gravitational potential it is required to only change that term. We present an example of the simple circular and elliptical orbit in Figure 3.6. For the elliptical orbit the only change in the initial conditions was that the test particle had an initial radial velocity of $v_{r_n} = 15\text{kms}^{-1}$.

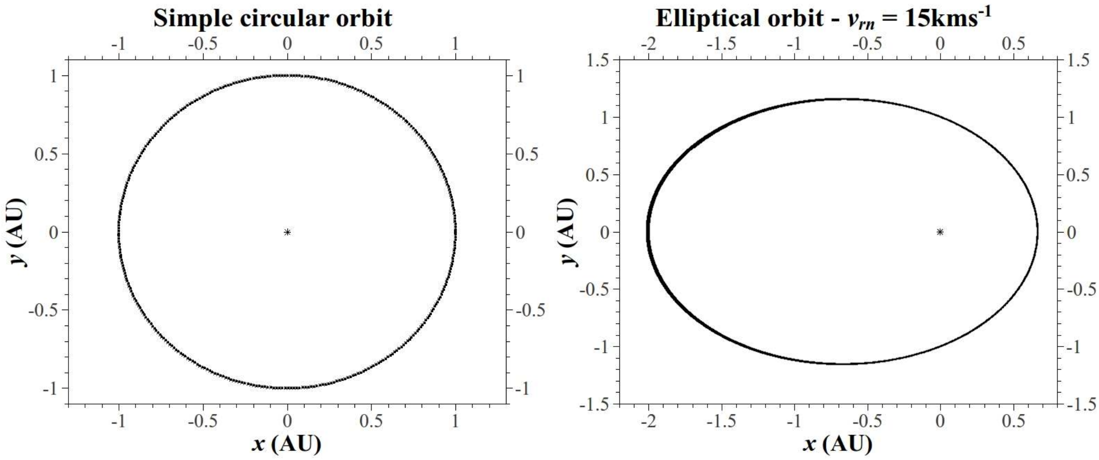

Figure 3.6: *A simple circular and elliptical orbit using the RKF method outlined above.*

3.4.5 Testing the potential/method

As can be seen from Figure 3.5 the circular speed in the plane of this potential rises sharply in the inner regions and then falls and levels out with $\dot{\phi}$ almost constant for $R > 8kpc$. This ensures that particles placed in the potential act in a way which is consistent with the observed stellar dynamics in spiral galaxies. It also allows the model to run more freely without the need to include some artificial rotation speed which would in-turn alter the specific angular momentum and therefore the consistency of the model. In order to test for this consistency the model is run for a variety of initial $R-$velocities ($5kms^{-1}$, $10kms^{-1}$, $15kms^{-1}$: with $z = 0$) which are shown in Figure 3.7. These test are run with a timestep of 1Myr up to a lifetime of 2.5Gyr with an initial radius of 5kpc.

The z-dependence is tested by keeping R constant at R =8kpc $\approx R_\odot$ and varying the initial height of the particle. This test is done for z =50pc, 100pc, 300pc, 800pc and 1kpc, again evaluated with a timestep of 1Myr up to a lifetime of 2.5Gyr. The test shows that as the initial height is increased the particle oscillates above and below the plane fewer times - at 50pc the particle oscillates $\approx$2.5 times per orbit and decreases to $\approx$1.75 times for an initial height of 1kpc (see Figure 3.8).

The model is then run for a variety of initial parameters (shown in Table 3.4) with a timestep of 1Myr up to a lifetime of 2.5Gyr. For all initial parameters the orbits are fairly stable but gradually become more unstable due to the inherent errors associated with the model and the large timestep used here (1Myr) which is apparent in the gradual increase of the local truncation error, ϵ_R, in Figures 3.9 b, d and f (see Equation 3.4.18 in Section 3.4.3).

	R	v_R	z	v_z	ϕ	v_ϕ
Set A	8kpc	-25kms^{-1}	50pc	30kms^{-1}	25°	10kms^{-1}
Set B	5kpc	10kms^{-1}	200pc	7kms^{-1}	25°	0kms^{-1}
Set C	8kpc	-10kms^{-1}	-100pc	-7kms^{-1}	125°	5kms^{-1}

Table 3.4: *The initial parameters which define the orbits plotted in Figure 3.9. Note that the velocity in the ϕ-direction, v_ϕ, above is added to the circular rotation speed which is defined by equation 3.3.6.*

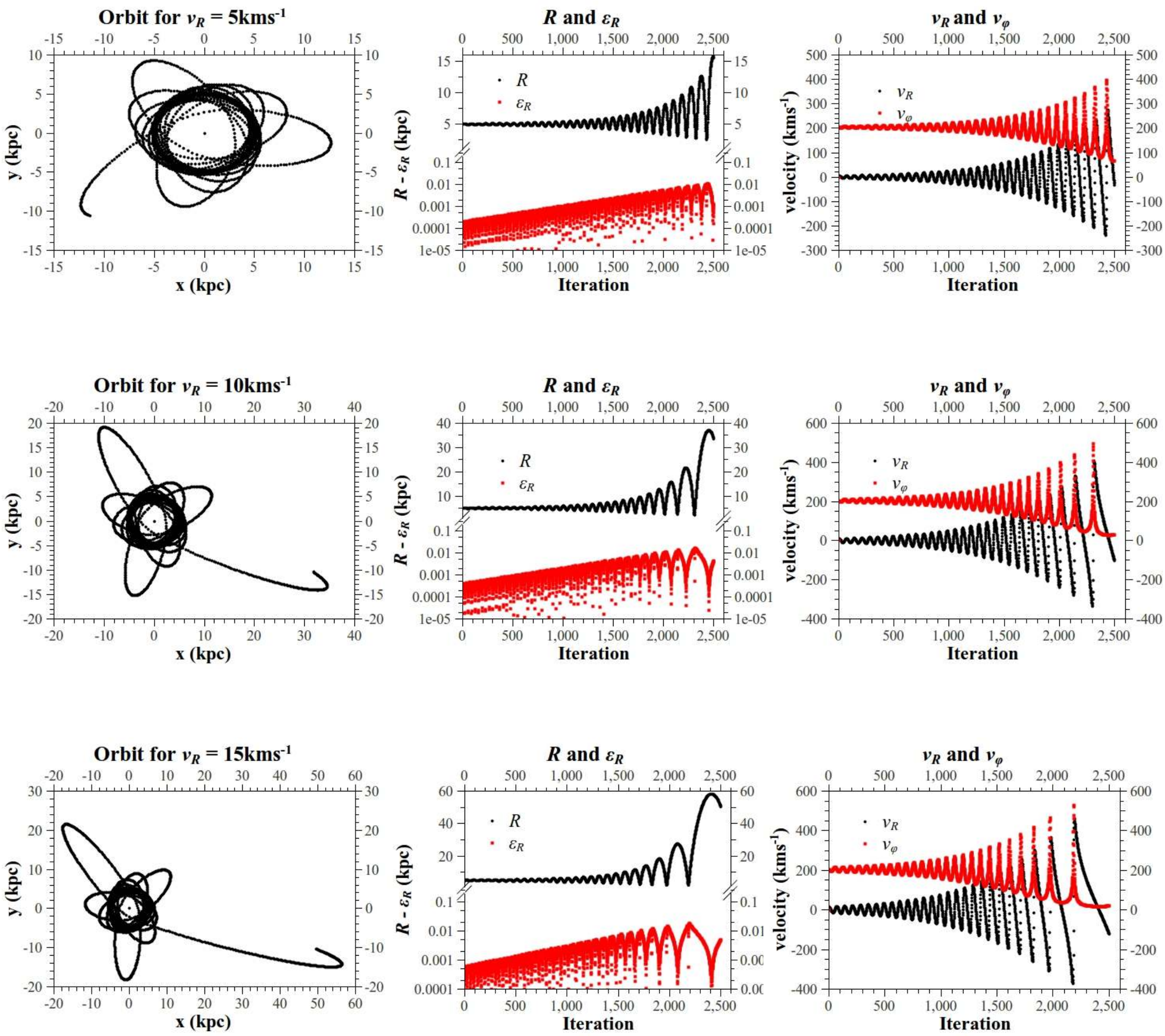

Figure 3.7: *Orbits in the galactic plane for different values of v_R (5kms^{-1}, 10kms^{-1} and 15kms^{-1}). Also shown are how R, ϵ_R (the truncation error at each step, see Equation 3.4.18), v_R and v_ϕ change with time - 1 iteration = 1Myr.*

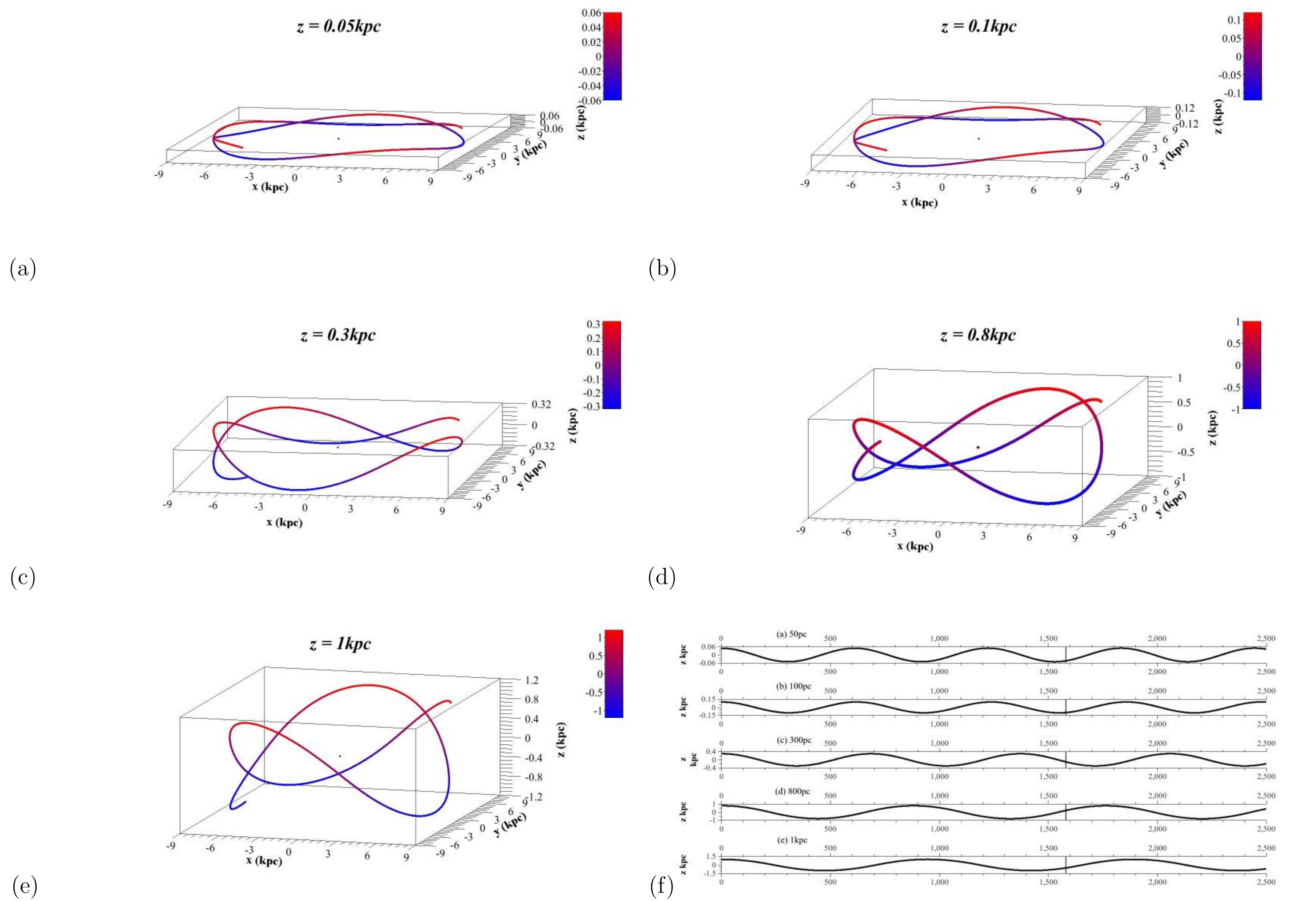

Figure 3.8: *Orbits with different initial heights above the galactic plane (at $R_\odot = 8kpc$) are evaluated so as to test the z-dependence of the potential. Plotted here are orbits with initial height (a)50pc (b)100pc (c)300 (d)800 (e)1kpc showing that the smaller the initial height, the more rapid the oscillation above and below the plane as shown in (f) where the vertical line indicates one full orbit.*

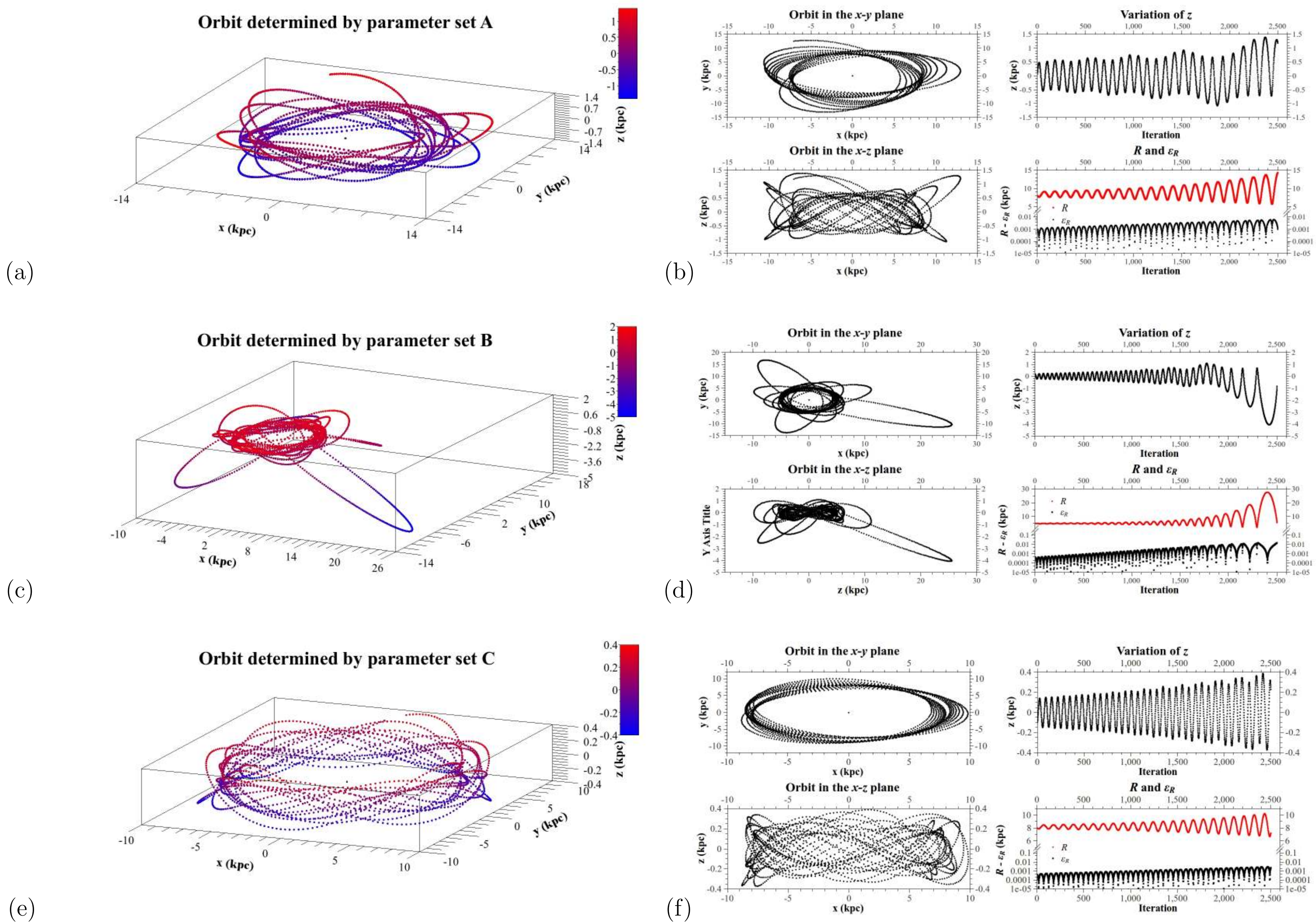

Figure 3.9: *The orbits determined by the parameters in Table 3.4. The figures on the right describe the orbits in the* $x - y$ *and* $x - z$ *plane along with the variations of* z, R *and* ϵ_R *with respect to time.*

3.5 Results

We first present some example trajectories for the test particles in the model in Figure 3.10.

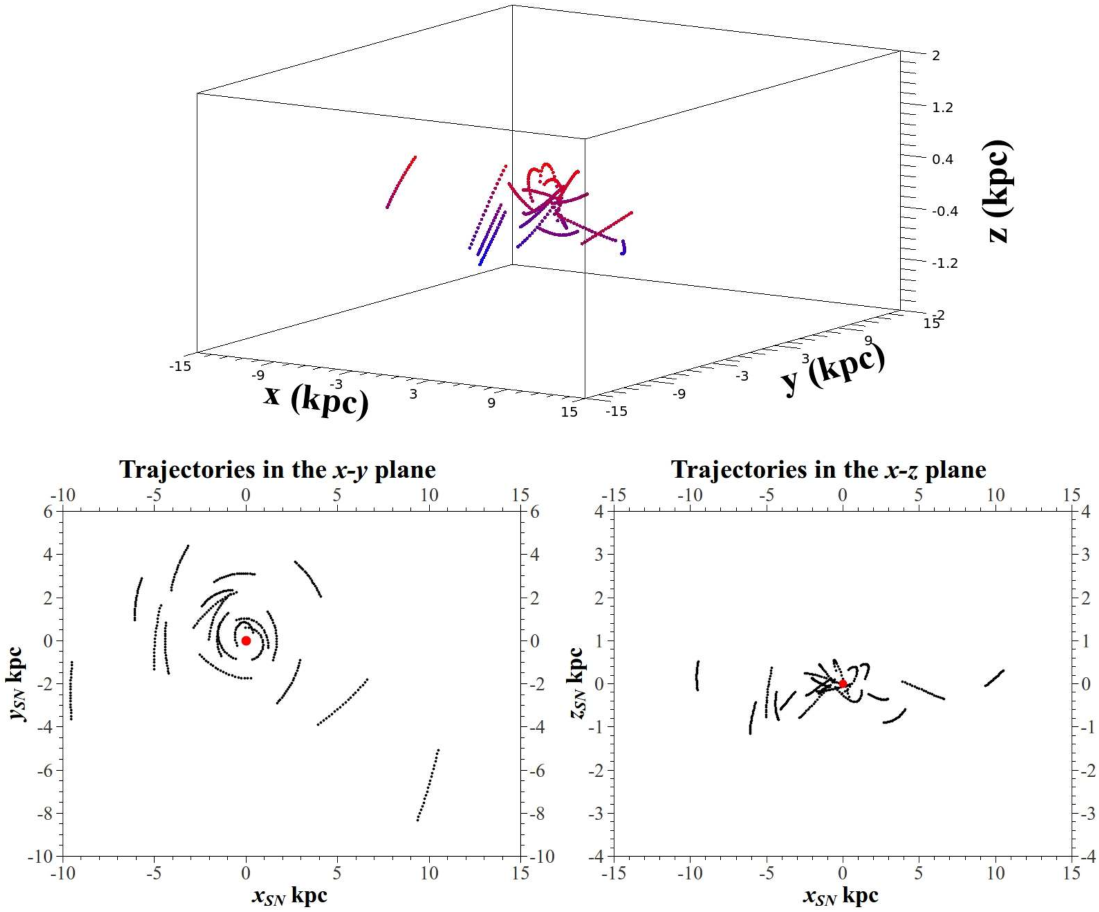

Figure 3.10: *From the distributions defined in Section 3.2 we present the trajectories of a sample of the 10,000 test particles.*

3.5.1 Face-on

Using the initial distribution of radial distances (R_i), heights (z_i) and velocities (v_z, v_R and v_ϕ) defined in Section 3.2 the model is run for a total of 10,000 test particles. The model has little impact on the radial distribution of particles. Out of the 10,000 test particles only 0.3% end up with a radial distance greater than the maximum imposed when setting the initial distribution - 15kpc - with only 0.02% having a final radial distance greater than 17kpc. This result would suggest that it is extremely unlikely that a SN will end up beyond the maximum radial extent of the disk due to a kick imparted by a former binary companion. The morphology of the distribution in R_{SN} does however change. We fit the final distribution of radial distances using a Scaled Levenberg-Marquardt algorithm[1] with a function of the form

$$\exp\left(\frac{-r}{h_r}\right) - \exp\left(\frac{-r}{h_b}\right) \tag{3.5.1}$$

The resulting fit shows that while the scalelength of the disk, h_r, has grown the scalelength of the bulge, h_b, has been reduced.

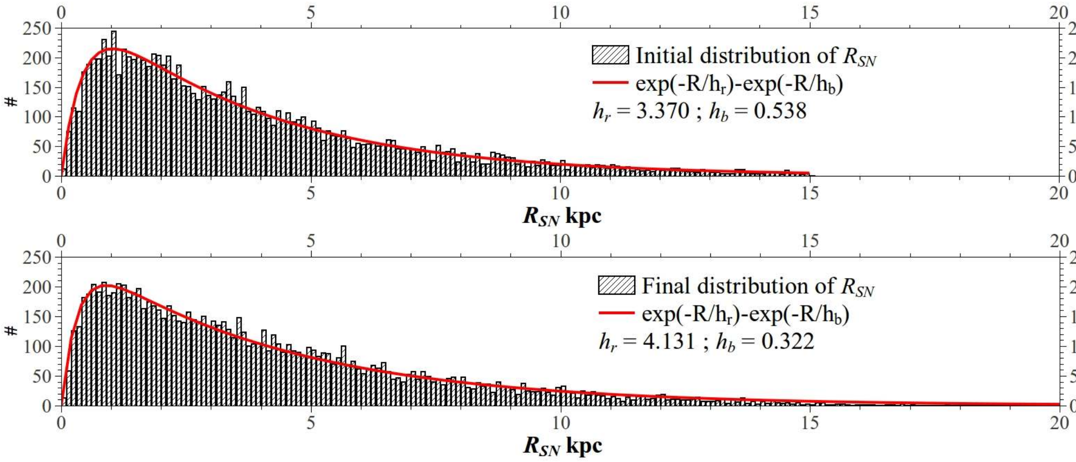

Figure 3.11: *Although there is no obvious deviation of the final distribution of R_{SN} (bottom) from the initial distribution (top) a fit to the profile reveals that the scalelength of the disk, h_r, has increased from 3.370 to 4.131kpc while the scalelength of the central deficit, h_b, has been reduced from 0.538 to 0.322kpc. Note also that only a very small fraction of the test particles end up beyond the initial maximum extent of the disk.*

We also construct a surface density profile for the final distribution using Equation 2.2.21. As can be seen from Figure 3.12 there is no major deviation from the initial distribution. A surface density profile of the initial distribution is fit with an exponentially decaying profile with a scalelength of 1.196kpc or $0.080R_{Gal}$ (where we take $R_{Gal} = 15$kpc) while the final distribution has only a very small variation and is fit with a scalelength of 1.291kpc or $0.086R_{Gal}$.

3.5.2 Edge-on

For the case of the edge-on distributions the deviation from the initial distribution is much more pronounced than for the radial distribution. The test particles become much more dispersed in the z-direction than they do in the R-direction, most

[1] Implemented within the GNU QTIplot program.

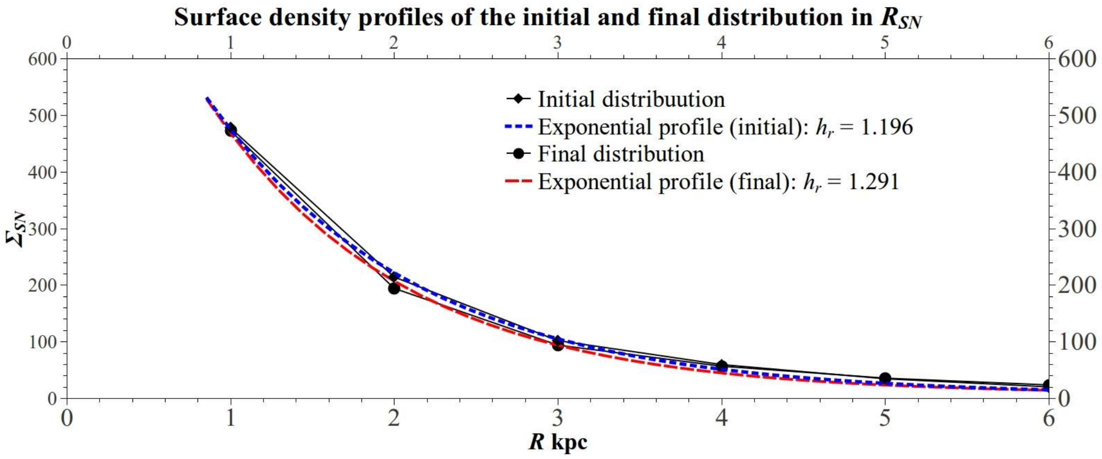

Figure 3.12: *The initial and final surface density distributions of test particles varies only slightly. The initial distribution is fit with an exponentially decaying scalelength of 1.196kpc while the final distribution is fit with a scalelength of 1.291kpc.*

likely because of the finite distances each particle can travel and the extent of the z-distribution compared to the R-distribution. As mentioned above we test the dependence of the final distribution of heights on the initial scaleheight by running the model with varying h_z. We fit the final distributions with a profile of the form

$$\operatorname{sech}^2\left(\frac{z}{h_z}\right) \tag{3.5.2}$$

and compare the initial, $h_{z,i}$, and final, $h_{z,f}$, scaleheights. We vary the scaleheights, in steps of 0.1kpc, from 0.2 to 1.0kpc each time setting the maximum height of the disk to be $3.33h_z$. The initial and final distributions are plotted together in Figure 3.15 with each plot showing the scalelength of the initial/final distribution. An interesting result of this exercise is that as the initial scaleheight is increased, $h_{z,f}$ tends to converge on $h_{z,i}$. As can be seen from Figure 3.16 the initial and final scalelengths converge at $\sim$0.9kpc after which the model has a compressing effect on the test particles.

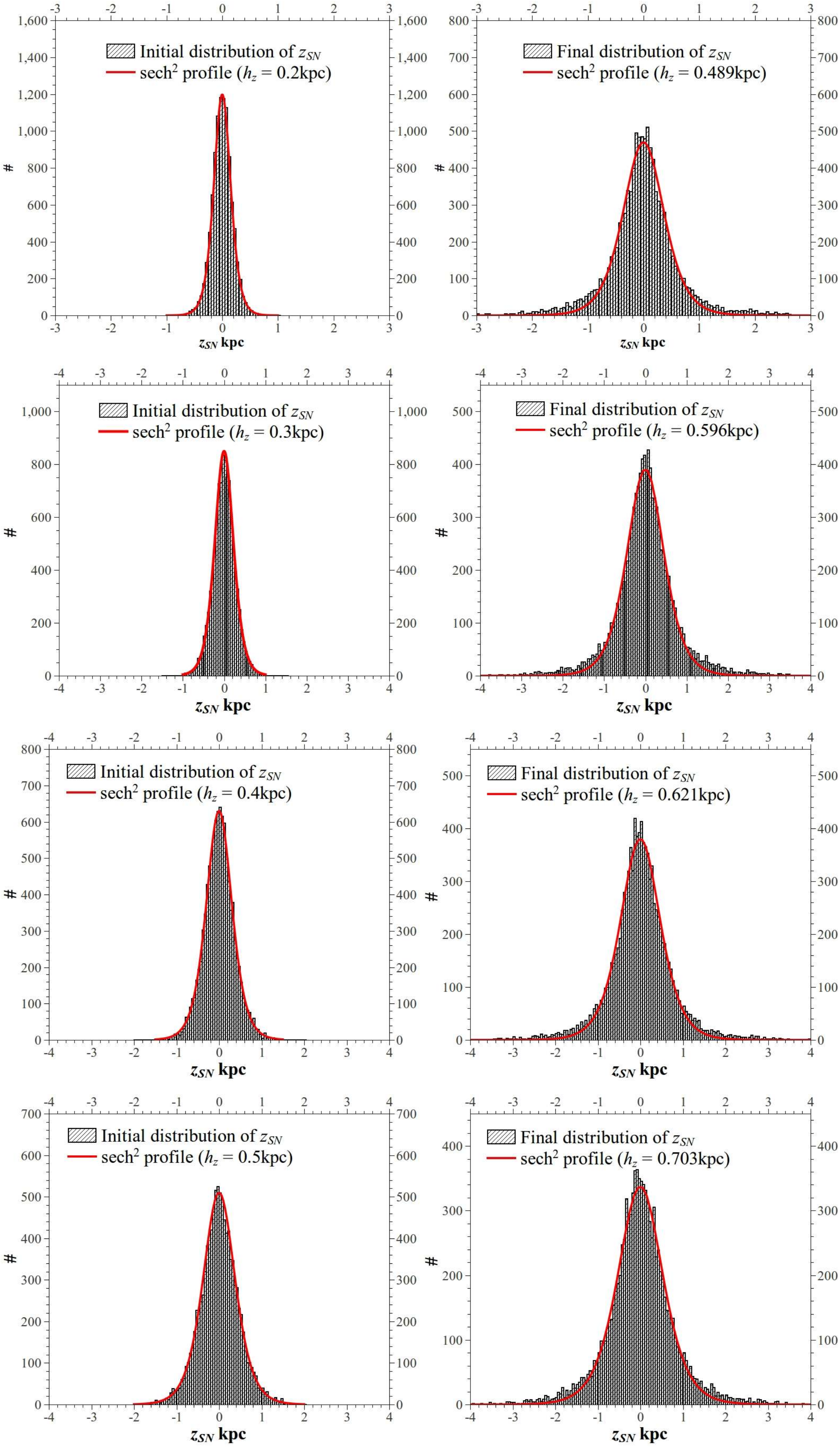
Initial distribution of z_{SN}
sech^2 profile (h_z = 0.2kpc)
Final distribution of z_{SN}
sech^2 profile (h_z = 0.489kpc)
Initial distribution of z_{SN}
sech^2 profile (h_z = 0.3kpc)
Final distribution of z_{SN}
sech^2 profile (h_z = 0.596kpc)
Initial distribution of z_{SN}
sech^2 profile (h_z = 0.4kpc)
Final distribution of z_{SN}
sech^2 profile (h_z = 0.621kpc)
Initial distribution of z_{SN}
sech^2 profile (h_z = 0.5kpc)
Final distribution of z_{SN}
sech^2 profile (h_z = 0.703kpc)
#
z_{SN} kpc

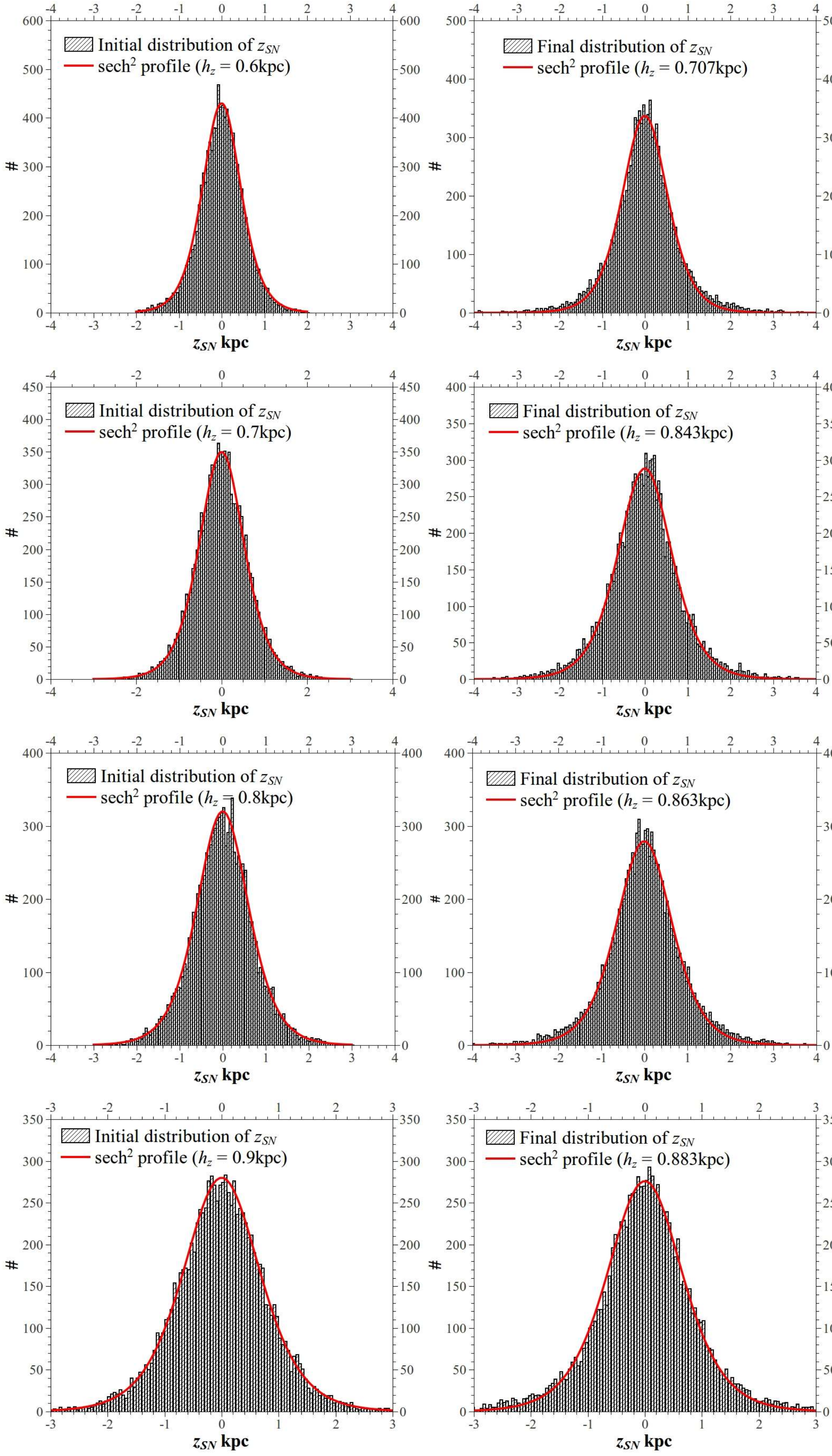
Initial distribution of z_{SN}
sech^2 profile (h_z = 0.6kpc)
Final distribution of z_{SN}
sech^2 profile (h_z = 0.707kpc)
Initial distribution of z_{SN}
sech^2 profile (h_z = 0.7kpc)
Final distribution of z_{SN}
sech^2 profile (h_z = 0.843kpc)
Initial distribution of z_{SN}
sech^2 profile (h_z = 0.8kpc)
Final distribution of z_{SN}
sech^2 profile (h_z = 0.863kpc)
Initial distribution of z_{SN}
sech^2 profile (h_z = 0.9kpc)
Final distribution of z_{SN}
sech^2 profile (h_z = 0.883kpc)
#
z_{SN} kpc

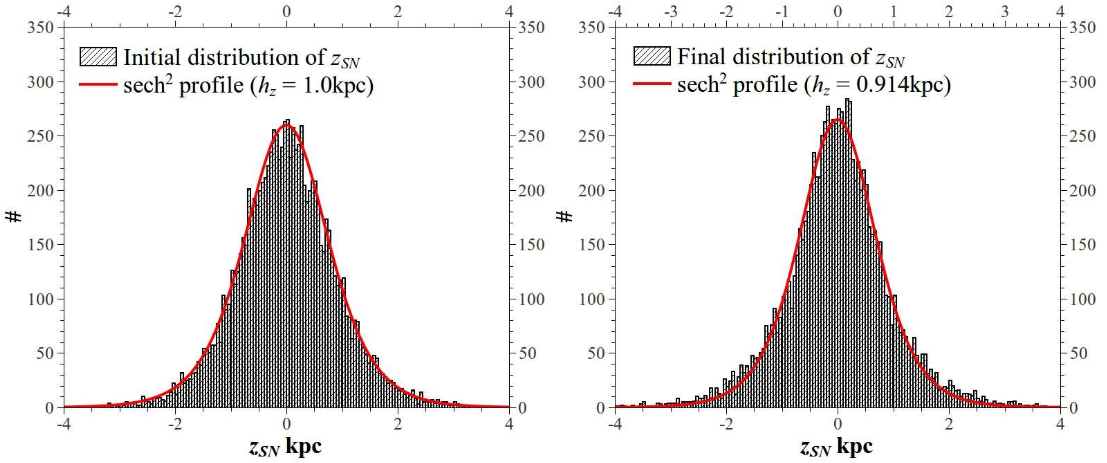

Figure 3.15: *The initial (left) and final (right) vertical distributions of test particles from the runaway model are shown above (and on the preceding pages). The initial distributions are characterised by their respective scaleheights, $h_{z,i}$. The smallest $h_{z,i}$ (0.2kpc) leads to the greatest dispersion of test particles with the final distribution fit with a scaleheight of $h_{z,f} =$ 0.489kpc or $2.445 h_{z,i}$. This dispersion decreases as $h_{z,i}$ is increased until the distribution begins to be compressed at $h_{z,i} >$ 0.9kpc.*

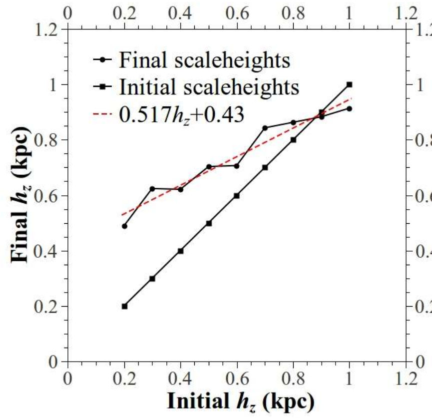

Figure 3.16: *The initial and final scaleheights converge for increasing $h_{z,i}$ at 0.9kpc. For $h_{z,i}$ >∼ 0.9kpc the model tends to compress the test particles.*

As a function of the initial scaleheight, the final scaleheights are fit with a linear function:

$$h_{z,f} = 0.517 h_{z,i} + 0.43 \text{ kpc} \qquad (3.5.3)$$

This result suggests that there is a higher chance of seeing a SN away from the disk of a "thin" galaxy if its progenitor had been given a high space velocity due to a kick provided by a former binary companion. Also, it suggests that for "thicker" galaxies the probability of finding a SN above/below the disk is diminished.

3.6 Discussion

We define a distribution of OB stars about an azimuthally homogeneous disk with a scalelength of 3.37kpc and varying scaleheights. The stars are situated in a gravitational potential which conforms to the dynamical characteristics of stellar orbits around a galaxy centre (ie. a flat rotation curve). We impart to each star a kick velocity based on observations of high velocity OB stars and pulsars assuming that the star had previously been a component in a massive binary where the primary component exploded as a SN. Each star also has a defined mass from which we derive a stellar lifetime, after which the star is assumed to have exploded as a SN. The positions at which the stars explode then make up the final distributions. We find that the scalelength of the final distribution of radial distances has increased from 3.37kpc ($0.24R_{Gal}$) to 4.131kpc ($0.28R_{Gal}$) while the scalelength of the surface density distribution of SNae has increased only slightly from 1.196kpc ($0.08R_{Gal}$) to 1.291kpc ($0.09R_{Gal}$). Only 0.3% of the stars end up beyond the initial maximum extent of the galaxy (15kpc) but note that we have used a minimum mass of $10M_{\odot}$ which sets a limit on the amount of time a star can travel. These results suggest that the radial distribution of CC SN progenitors does not completely follow the distributions of light in galaxies since the scalelength of the surface density of CC SNae from Chapter 2 exhibits a much more gradual falloff ($0.67R_{Gal}$ - or $0.35R_{Gal}$ excluding the observed central deficit - compared to $0.09R_{Gal}$ from the model). The final distribution of heights does however show a marked variation from the initial distribution for the case of a scaleheight of 0.3kpc. We find that for a scaleheight of 0.3kpc the final distribution is fit with a sech^2 profile with a scaleheight of 0.596kpc, an increase of almost double the initial value. We also find that 13.6% of the stars end up beyond the maximum height of the initial distribution (1kpc in this case). Applying the same photometric method as for the observed SNae in Section 2.3.1 (see Equation 2.2.17) we construct a light profile of the form

$$I(r, z) = I_0 \exp\left(\frac{-r}{h_r}\right) \text{sech}^2\left(\frac{z}{h_z}\right) \tag{3.6.1}$$

and use the final positions (R_{SN},z_{SN}) to separate a subgroup of SNae that would be deemed to be positioned away from brightness profile of the host galaxy. From this method we find that at the final positions of 24.7% of the stars the surface brightness is less than 1% of the central surface brightness for the case of $h_z = 0.3$kpc. We show in Table 3.5 for differing initial scaleheights the corresponding characteristics of the final height distributions. For smaller initial scaleheights it is clear that it is much easier for a runaway star to distance itself from the host galaxy. This is due

Initial h_z (kpc)	Final h_z (kpc)	$z_{SN} > z_{max}$ (%)	$I(r, z) < 0.1I(0, 0)$ (%)
0.2	0.49	20.6%	32.7%
0.3	0.60	13.6%	24.7%
0.4	0.62	7.5%	16.1%
0.5	0.70	5.5%	13.4%
0.6	0.71	2.9%	8.5%
0.7	0.84	1.9%	7.8%
0.8	0.86	1.4%	6.3%
0.9	0.88	0.5%	4.4%
1.0	0.91	0.4%	3.7%

Table 3.5: *For each initial scaleheight (h_z) we show the corresponding final scaleheight, the percentage of stars that end up beyond the initial maximum height of the disk ($z_{max} = 3.33h_z$) and the percentage of stars whose positions would have less than 1% of the central surface brightness of the galaxy.*

to the finite lifetimes, and the finite distances they can travel, of the SN progenitors. For a star to travel to a away from the disk in a thick galaxy would require either a greater velocity and/or a longer lifetime. The initial and final scalelengths converge at ∼0.9kpc which suggests that the potential of the galaxy acts a s a "high pass filter", allowing only very high velocity stars to escape it. This brings into question the origin of the the examples of CC SNae which occurred well above the disk of their host galaxy from Chapter 2 (see Figure 2.9). A possible explanation for their extraordinary height may be that their progenitors had lower masses than the current model allowed ($10M_\odot$) and therefore longer lifetimes allowing them to travel further. Our model was also limited in the magnitude of the velocity kick imparted to the SN progenitors. Stars may achieve extremely high velocities in encounters with a massive compact object at the centre of a galaxy (Brown et al., 2005). There is also the possibility that these SNae, which are placed well above the disk of their host galaxy, may be tracers of field type O-stars (de Wit et al., 2005). The percentage of SNae that lie in low surface brightness areas from our model compares well with percentage of runaway candidates from Chapter 2 for the cases with initial scaleheight 0.4 or 0.5kpc. However, the SNae that are observed to be well above the disk cannot be explained by the current model and suggests that their presence indicates either a dynamical event which imparts massive velocities to their progenitors or a population of massive stars which form in isolation, away from the disk. It is interesting to note that for the observed sample of SNae in Chapter 2, those SNae that are recorded to have a vertical height greater than 2kpc are all type II SNae, indicating a relatively low metallicity (which is common for halo stars) compared to those in the disk.

Chapter 4

Modelling the dispersion of HMXBs

4.1 Introduction

The nature of the spiral structure observed in many galaxies has been studied for many years with a number of hypotheses emerging about their origin. Among these theories are (i) the Spiral Detonation Wave theory which suggests that star formation is a self renewing action - star formation in the spiral arms trigger more star formation in nearby regions causing a self-propagating wave of stellar births (Mueller and Arnett, 1976) (ii) the formation of spirals due to interactions with a galactic bar - it has been suggested that the spiral structure can be driven by forces exerted by a central bar (Sanders and Huntley, 1976) however this proposal has difficulty explaining spiral structure in galaxies with no bar (iii) Magnetohydrodynamic theories - forces due to magnetic fields have been proposed to have influence on the spiral structure in galaxies but observations of magnetic fields yield field strengths which are much too small to have any significant effect in building and maintaining a spiral (Spitzer, 1978) (iv) Gravitational effects of nearby galaxies - Toomre and Toomre (1972) suggested that gravitational forces from nearby galaxies can introduce a perturbation which manifests itself as a spiral pattern and was shown to have this effect (Toomre, 1981) but are unable to maintain it for long periods of time. There is still much unknown about the nature of spiral patterns in galaxies but a theory accepted by most and which is capable of creating and maintaining spiral structure over long periods of time is the theory put forward by Lin and Shu (1964) in which the spiral pattern is the result of a density wave propagating through the disk. Stars in the galactic disk have elliptical orbits with varying epicyclic frequencies which naturally lead to a spiral structure which can be sustained over long periods of time.

These spiral structures are host to vigorous star formation and young stellar objects should be tightly correlated with the spiral structure. Maps of Hα emission have been shown to follow this pattern which is a consequence of its origin from the young stellar populations here (Kennicutt, 1998). An example of a short-lived stellar population in galaxies is the High Mass X-ray Binaries (HMXBs). These are binary systems which contain either a neutron star or a black hole. Mass is accreted on to the compact object from a massive companion and powers the X-ray emission. HMXBs have a lifetime in the range 10^{6-7} years and are therefore commonly associated with regions of recent star formation (Giacconi and Gursky, 1974). In this chapter we develop a population synthesis code to evolve binary systems and produce a sample of these HMXBs. We then use this sample to populate a dynamical model and measure their dispersion from the spiral arms.

The spiral pattern in most galaxies (unperturbed "grand design" galaxies) can be adequately described by a logarithmic spiral of the form (in polar coordinates)

$$\phi - \phi_0 = \pm \frac{\ln(\frac{r}{r_0})}{\tan(\alpha)} \tag{4.1.1}$$

where ϕ_0 and r_0 indicate the origin of the spiral arm and α is the angle made between the arm and the tangent to a circle at that point known as the pitch angle. The $\pm$ operator defines the direction that the spiral arms swing - using a minus sign a spiral such as that in Figure 4.1 is produced.

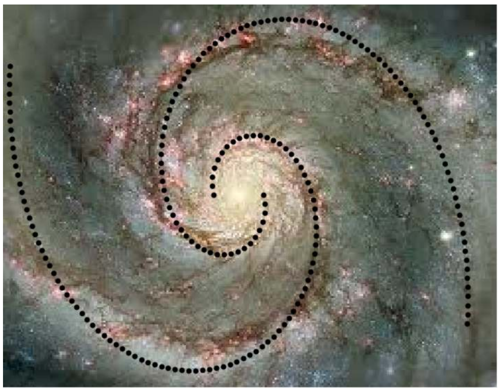

Figure 4.1: *This figure shows a logarithmic spiral defined by equation 4.1.1 with a pitch angle of α=19° overlain on an image of the spiral galaxy M51. As can be seen, the spiral arms are not perfectly logarithmic but are well approximated by the spiral.*

Not to be confused with the rotational velocities of stars in the disk, the spiral pattern moves with its own characteristic pattern speed, Ω_p. For our purposes we take it that the pattern speed moves with constant angular velocity. As a starting point we assume the pattern rotates with a speed of 30kms^{-1}kpc^{-1} which leads to an angular speed of $\approx 9.72 \times 10^{-16}$rads^{-1}. At a radial distance of R=1kpc the spiral pattern has a rotational velocity, v_p, of 30kms^{-1} which is given simply by

$$v_p = R\Omega_p \tag{4.1.2}$$

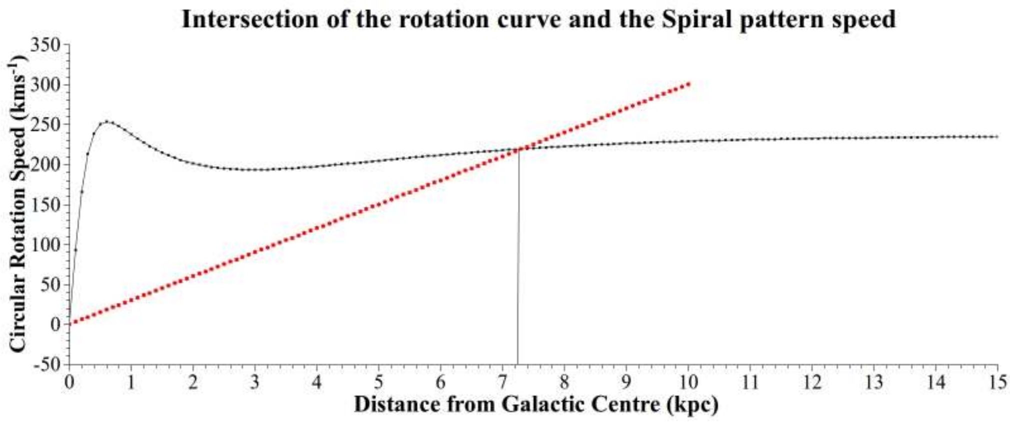

Figure 4.2: *Since no analytical solution is available from equating the pattern speed with the equation governing the rotation curve due to the potential we take the co-rotation radius to be the point where the two lines plotted above intersect - 7.2kpc.*

Rotating the spiral pattern is done simply by

$$\phi - \phi_0 \pm \phi_p = \frac{\ln(\frac{r}{r_0})}{\tan(\alpha)} \tag{4.1.3}$$

where now we have a $\pm$ operator which defines which way the spiral rotates (trailing (+) or leading (-)) and we set

$$\phi_p = \Omega_p \times t(rads^{-1}) \tag{4.1.4}$$

where t is the time.

Ω_p (kms^{-1}kpc^{-1})	r_c (kpc)
10	23.4
30	7.3
50	3.9

Table 4.1: *The various pattern speeds used in the model and their corresponding co-rotation radii.*

The co-rotation radius, r_c, is the radius at which the circular speed of the test particles, $\dot{\phi}$ from Equation A.4.11, due to the gravitational potential equals the rotational speed of the spiral pattern, Ω_p (rads^{-1}). Within this radius the test particles move, without any "kick", ahead of the spiral pattern due to their higher rotational velocities. Beyond this radius the test particles lag behind the pattern. Equating the pattern speed with the equation which defines the rotation curve (Equation A.4.11) is a natural first step in trying to evaluate the co-rotation radius. However, due to the nature of the rotation curve equation it is not possible to evaluate analytically the co-rotation radius so here we have plotted both functions and taken the co-rotation radius as the point where both lines intersect. From Figure 4.2 it is clear that they intersect at around 7.2kpc. In order to refine the value of the co-rotation radius further we use a minimization script to obtain more accuracy. The script subtracts the value of $\dot{\phi}$ (Equation A.4.11) evaluated at different R from Ω_p until the remainder goes below a certain threshold. From this method we obtain for a pattern speed of 30kms^{-1}kpc^{-1} a value of $r_c = 7.302$kpc. We use the same method to determine the co-rotation radii for pattern speeds of 10kms^{-1} and 50 kms^{-1} which are listed in Table 4.1.

4.2 Population Synthesis

A simple population synthesis is developed so that as the model is run the number and nature of the binary systems are consistent with binary evolution theory. We first set up a population synthesis model which has initially thousands of objects with coeval evolution (hereafter the "starburst model") to ensure that the model produces a plausible amount of binary disruptions. For example Dray et al., (2005) estimate from models that the runaway fraction of OB stars is ∼50% of the total population whereas observations by Gies (1987) suggest the runaway population to be 10-30% with an extra 20% estimated to be uncounted runaways due to their low space velocities (de Wit et al., 2005). The synthesis is then run in a way in which it is continuously populated at a constant rate (hereafter the "continuous starburst model") to ensure that the population levels reach an equilibrium. Once the population levels agree with previous studies (Meurs and van den Heuvel, 1989) then the synthesis model is used to populate the dynamical model to investigate the motions of such objects and ultimately their final positions in relation to the spiral arms. Stellar parameters are defined according to the fitting functions of Eggleton et al., (1989) but for simplicity we assume no temporal dependence during the main sequence or giant phases of stellar evolution - Eggleton et al., (1989) set the luminosity and radius of their stars as a function of their respective ages.

4.2.1 The binary population

The initial masses of the primary stellar population (M_1, the primary component being the initially most massive star in the binary) have a distribution, shown in Figure 4.3, following the formulations of Bethe & Brown (1998) such that

$$\Theta(M_1) \propto M_1^{-1.5} \tag{4.2.1}$$

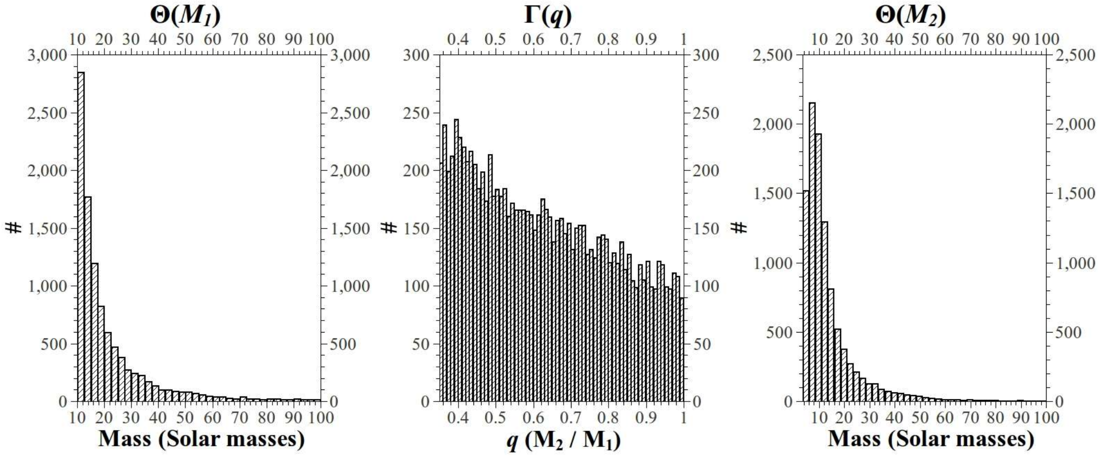

Figure 4.3: *The distribution of primary stellar masses (the primary being the initially most massive star in the binary) is defined by $\Theta(M_1) \propto M^{-1.5}$. The distribution of secondary masses, $\Theta(M_2)$, is then defined by the distribution of mass ratios ($q = \frac{M_2}{M_1}$), $\Gamma(q) = \frac{2}{(1+q)^2}$, where q is limited to the range 0.35$\leq$ q $\leq$1.0.*

where we set a lower mass limit of M_1=$10M_\odot$ since we require that the primary undergo a SN event to evolve and become a compact object and an upper mass limit of $100M_\odot$[1]. We follow Portegies Zwart & Verbunt (1996) and set a mass ratio distribution ($\Gamma(q)$, where $q = M_2/M_1$) according to

$$\Gamma(q) = \frac{2}{(1+q)^2} \tag{4.2.2}$$

$\Gamma(q)$ is limited to the interval 0.35< q <1 as Equation 4.2.2 relates only to binaries with massive primaries (see Figure 4.3). The distribution for high mass binaries with a lower mass ratio is uncertain and has been suggested to have a flat distribution (Hogeveen, 1992). We set the distribution of semi-major axes, $\Xi(A)$, to follow a logarithmic distribution (Figure 4.4)

$$\Xi(A) \propto \frac{1}{A} \tag{4.2.3}$$

with $6.96 \times 10^{10}m \leq A \leq 7\times10^{13}m$ ($10R_\odot \leq A \leq 10^5 R_\odot$) where the maximum separation, taken from Belczyński and Bulik (1999) is the point beyond which the binary period becomes extremely large and the likelihood of the system surviving a SN is greatly diminished. The lower limit on the semi-major axis allows the binary components to evolve separately - the primary will have at least a radius of $\sim 3.75R_\odot$ (for a $10M_\odot$ star - see Equation 4.2.4). We again follow Belczyński and Bulik (1999) in their procedure for the more massive binaries. If the sum of the radii in the binary exceeds $A_{min} = 10R_\odot$ the semi-major axis is set as twice the primary radius and the

[1](Portegies Zwart & Verbunt (1996) set their distribution proportional to $M_1^{-1.7}$)

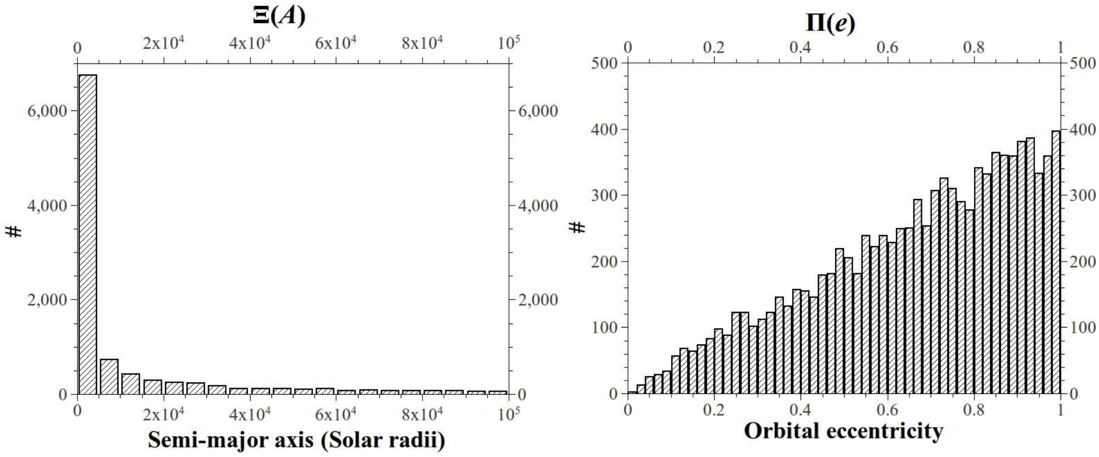

Figure 4.4: *The distribution* $\Xi(A)$ *is logarithmic. We set the minimum orbital separation to be* A_{min}*=10*$R_\odot$ *and, so as to avoid a period of common envelope evolution or merger, if the sum of the radii in the binary exceeds this* A_{min} *the semi-major axis is set to twice the radius of the primary (and the orbit is circularised). The maximum is set to be the that radius, beyond which, the binary is unlikely to survive a SN explosion and the period becomes extremely long which we assume to occur at radii approaching* $\approx 10^5 R_\odot$*. The orbital eccentricities have a distribution between 0 and 1 with* $\Pi(e) = 2e$ *following Duquennoy & Mayor (1991).*

eccentricity set to zero. This should remove any possibility of a merger. The main sequence (MS) radius is calculated from the fitting formula described by Eggleton et al., (1989)

$$R_{MS} = \frac{1.968M^{2.887} - 0.7368M^{1.679}}{1.821M^{2.337} - 1} R_\odot \tag{4.2.4}$$

where M is in solar masses.

The eccentricities, e, of the binary orbits are distributed according to Duquennoy & Mayor (1991) (Figure 4.4) such that

$$\Pi(e) = 2e \tag{4.2.5}$$

where $0 \leq e \leq 1$. We include the effects of tidal interactions on the orbital eccentricity of close massive binaries. Proposed by Portegies Zwart & Verbunt (1996), if the radius of the primary is greater than 0.2 times the periastron distance, r_p, then, conserving angular momentum and in one iteration, the orbit is circularised until r_p is five times the primary radius or until the orbit is completely circular - ie. e is reduced until either r_p is $5R_q$ or $e = 0$. This change occurs according to

$$(1 - e_1^2)a_1 = (1 - e_0^2)a_0 \tag{4.2.6}$$

where subscript 0 refers to the initial state, subscript 1 to the final state and $r_p =$

$a(1-e)$.

We follow Belczyński and Bulik (1999) and determine the main sequence lifetime of each of the stars, τ_{MS}, to be

$$\tau_{MS}(M) = 20 \times 10^6 \left(\frac{M}{10M_\odot}\right)^{-2} \quad \mathrm{yr} \tag{4.2.7}$$

where M is expressed in solar masses. We also take the duration of the giant phase to be τ_G=0.2τ_{MS} giving a total lifetime before a SN event $\tau_{total} = \tau_{MS} + \tau_G$ after which, due to the short timescales after the giant phase, it is assumed that the stellar component evolves instantly to a compact object.

Now that the initial distribution of the parameters is set, the population synthesis is run. If the radius of the primary after it becomes a giant, $R_{1,G}$, (which we assume to be simply twice the MS radius) exceeds the Roche lobe radius, r_L, then a period of mass transfer ensues. The Roche lobe radius is approximated by the formula of Eggleton (1983)

$$r_L = A\frac{0.49q^{2/3}}{0.6q^{2/3} + \ln(1+q^{1/3})}R_\odot \tag{4.2.8}$$

We assume that during the period of mass transfer the primary loses all of its Hydrogen envelope and all that remains is the Helium core which we take to be 0.3 times the initial mass (Bethe and Brown, 1998) giving a primary mass, after mass transfer, $M_{1,f}$

$$M_{1,f} = 0.3M_1 \tag{4.2.9}$$

Only a proportion of the lost mass is given to the secondary, the amount of which is dependent on the mass ratio q (Vrancken et al., 1991; Bethe and Brown, 1998). The mass of the secondary, after mass transfer, $M_{2,f}$, is

$$M_{2,f} = M_2 + 0.7q^2M_1 = f \times M_1 \tag{4.2.10}$$

where

$$f = q + 0.7q^2 \tag{4.2.11}$$

and the semi-major axis is then, from Pols and Marinus (1994),

$$A_f = A\left[\left(\frac{M_{1,f}}{M_1}\frac{M_{2,f}}{M_2}\right)^{-2}\left(\frac{M_{1,f}+M_{2,f}}{M_1+M_2}\right)^{(2\beta+1)}\right] \tag{4.2.12}$$

where here we take β=6 which is an uncertain parameter that takes into account the angular momentum lost by the ejected matter (Belczyński and Bulik, 1999). At this point the secondary will have gone through a fraction $g(q)$ of its lifetime whereby

$$g(q) = q^2 + 0.2f^2 \tag{4.2.13}$$

since, from Equation 4.2.7, the stellar lifetime is inversely proportional to the square of the mass (Bethe and Brown, 1998). If g >1.2 then we assume the secondary has exploded as a SN before the primary (shortly after mass transfer) and it is then considered the primary component for the rest of the synthesis - it is now the stellar component that accretes matter from the secondary (formerly the primary) to produce X-ray emission. If 1< g <1.2 the the secondary is instantaneously in the giant phase while if g <1 then the secondary is still on the main sequence.

For mass transfer to occur in a binary the primary must fill its Roche lobe. This also has the effect of circularising the orbit due to tidal interactions. For this reason it is assumed that those binaries that have undergone mass transfer now have zero orbital eccentricities as in Belczyński and Bulik (1999).

4.2.2 The SN

For the population of binaries who have not undergone a period of tidal interaction or mass transfer (ie. their orbital eccentricities are non-zero) a position in orbit is randomly chosen so as to determine the effect of a SN kick on the binary parameters of the remaining system. The position in the stars orbit, defined by its eccentric anomaly - the angular distance from perihelion in an elliptic orbit, does not progress uniformly with time. A fictitious orbit is defined which is circular with a radius and period equal to our "real" stars semi-major axis and period. The position in this idealised orbit, which has constant angular momentum, is defined by the "mean" anomaly. Given a mean anomaly and the (real) systems orbital eccentricity it is possible to randomly choose a position in an eccentric orbit in a way which affords an equal probability of being chosen to all orbital positions. A mean anomaly, κ, between 0 and 2π is chosen randomly since it progresses uniformly with time and gives an instantaneous position in the elliptical orbit. A simple method is used along with the each systems eccentricity to solve Kepler's equation iteratively to find the eccentric anomaly, ε, from which the true anomaly, θ, and radial distance from the focus, r, are found:

$$\cos(\theta) = \frac{\cos(\varepsilon) - e}{1 - e\cos(\varepsilon)} \tag{4.2.14}$$

$$r = A_f[1 - e\cos(\varepsilon)] \tag{4.2.15}$$

where we denote A_f as the semi-major axis of the system just prior to the SN. The orbital velocity of the SN progenitor just prior to the SN, v, is then given by (Portegies Zwart and Verbunt, 1996)

$$v^2 = G(M_{1,f} + M_{2,f}) \left[\frac{2}{r} - \frac{1}{A}\right] \tag{4.2.16}$$

For the distribution of velocity kicks imparted to the SN remnant, $\Psi(v_k)$, two options are tested. Firstly a simple Gaussian distribution with a mean velocity of 500kms^{-1} and σ =150kms^{-1} (Figure 4.5) which we denote $\Psi_A(v_k)$ and secondly a flat distribution from 150-200kms^{-1} which is denoted $\Psi_B(v_k)$. There have been many efforts to constrain the distribution of SN kicks, mainly by investigating the distribution of pulsar velocities. It has been shown that many pulsars have a velocity well over 500kms^{-1} and measurement of offsets from SN remnants indicate that the distribution has a tail of high velocities (Arzoumanian et al., 2002; Frail et al., 1994) - some authors model their kick velocities on Maxwellian, Gaussian or the sum of two Gaussian distributions (Hobbs et al., 2005; Portegies Zwart and Verbunt, 1996). However, the dynamics of neutron stars has also been fit with models that give the remnant a kick of 200kms^{-1} (Blaauw and Ramachandran, 1998) and kicks in the range 150-200kms^{-1} (Lipunov et al., 1997).

After the SN the velocity of the remnant, v_n, is

$$v_n^2 = v^2 + v_k^2 + 2vv_k\cos(\gamma) \tag{4.2.17}$$

where γ is the angle, chosen randomly, between v and v_k. We assume that all stars which were initially less than $40M_\odot$ evolve after SN to become a neutron star of mass M_{Rem}= $1.4M_\odot$ (M_{Rem} - remnant mass) and that those larger than this become black holes with a mass according to the following equation (van den Heuvel and Habets, 1984)

$$M_{Rem} = [0.35M_{1,f} - 12]M_\odot \tag{4.2.18}$$

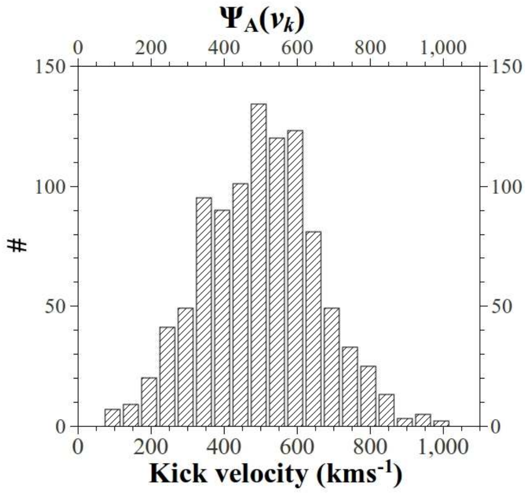

Figure 4.5: *For some of the scenarios described below we model the distribution of velocity kicks which are imparted to the compact object as a simple Gaussian with a mean of 500kms^{-1} and σ=150kms^{-1} ($\Psi_A(v_k)$).*

with $M_{1,f}$ in solar masses. Following Hills (1983) we assume that the binary is dissociated if

$$\frac{M_{ME}}{(M_{1,f}+M_{2,f})} \geq \frac{r}{2A_f}\left[1-\left(\frac{v_k}{v_c}\right)^2-2\left(\frac{v}{v_c}\right)\left(\frac{v_k}{v_c}\right)\cos(\gamma)\right] \tag{4.2.19}$$

where M_{ME} is the mass ejected in the SN explosion ($M_{ME} = M_{1,f} - M_{Rem}$) and v_c is the circular velocity of the orbit (ie. when $r = A_f$). The new semi-major axis for those systems which have not been disrupted, A_n, is then found from

$$v_n^2 = G(M_{Rem}+M_{2,f})\left[\frac{2}{r}-\frac{1}{A_n}\right] \tag{4.2.20}$$

so that

$$A_n = \left[\frac{2}{r}-\frac{v_n^2}{G(M_{Rem}+M_{2,f})}\right]^{-1} \tag{4.2.21}$$

A disruption rate, d_{SN}, is defined from the starburst model which quantifies the percentage of all initial binaries that have been disrupted in the SN

$$d_{SN} = \frac{\text{number of binaries disrupted}}{\text{total number of initial binaries}} \tag{4.2.22}$$

This rate allows one to determine the effect of altering the distribution of velocity kicks and gives an idea of how many X-ray emitters could populate the dynamical model.

4.2.3 X-ray Luminosity

We assume that all of the binaries that remain bound after the SN explosion of the primary component emit X-rays due to the wind fed accretion on to the the compact SN remnant. Depending on the initial conditions the synthesis produces a population of X-ray emitters according to the disruption rate, d_{SN}. The X-ray luminosity of the undisrupted population is assumed to be due to a wind-fed mechanism which, for the purposes of this study, is adequately described by the accretion method outlined by Bondi & Hoyle (1944) along with the assumption that all of the gravitational potential of the accreted material is released as X-rays which follows the work of Iben et al., (1995). The X-ray luminosity is approximated according to Equation 4.2.23:

$$L_x = \frac{4.1\times10^{11}}{\alpha_w^4}\left[\frac{M_{Rem}}{M_{2,f}}\right]^2\left[\frac{R_2}{A_n}\right]^2\dot{M}_w L_{\odot} \tag{4.2.23}$$

where M_{Rem} and $M_{2,f}$ are the masses of the compact SN remnant and the donor (secondary) star respectively, R_2 is the radius of the donor star, A_n is the post-SN semi-major axis, subscript "w" indicates that the parameter is associated with the stellar wind and $\dot{M}_w$ is in $M_{\odot}yr^{-1}$ (Iben et al., 1995). Equation 4.2.23 also takes into account the kinetic energy of the wind which is parameterised by its velocity. α_w is a term which takes into account the velocity of the wind as it is accreted onto the compact object. Stellar winds may not stop accelerating out to great distances meaning that in a close binary system the emitted winds may not have reached their maximum velocity (where α_w=1). We follow the prescription of Waters & Kerkwijk (1989) and take

$$\alpha_w = 1 - \frac{R_2}{A_n} \tag{4.2.24}$$

We take the mass loss rate due to stellar winds, $\dot{M}_w$, from the donor star (the secondary) to be given by

$$\dot{M}_w = \frac{L_{OB}}{v_{\infty}c} \tag{4.2.25}$$

where L_{OB} is the luminosity of the donor star. The luminosity depends on whether it is a MS or giant star and is calculated with the fitting functions of Eggleton et al., (1989) (Equations 4.2.27 and 4.2.28). In Equation 4.2.25 v_{∞} is 3 times the escape velocity of the star (Equation 4.2.26) and c is the speed of light.

$$v_{\infty} = 3\sqrt{\frac{2GM_{2,f}}{R_2}} \tag{4.2.26}$$

$$L_{OB,MS} = \frac{13990M^5}{M^4 + 2151M^2 + 3908M + 9536}L_{\odot} \tag{4.2.27}$$

$$L_{OB,BGB} = \frac{2.15M^2 + 0.22M^5}{1 + (1.4 \times 10^{-2})M^2 + (5 \times 10^{-6})M^4}L_{\odot} \tag{4.2.28}$$

where $L_{OB,MS}$ is the main sequence luminosity and $L_{OB,BGB}$ is the luminosity at the base of the giant branch and M is in solar units.

For the lifetimes of the X-ray sources we again follow Iben et al., (1995) and use the analytical approximations of Massevitch et al., (1979) for donor stars, with mass M_2, who are still on the main sequence (ie. $g(q)$ <1), τ_A, and for those who are in the giant phase (1< $g(q)$ <1.2), τ_B.

$$\tau_A = 1000M_2^2(1 + 0.000005M_2^{3.5})^{-1}\text{yr} \tag{4.2.29}$$

$$\tau_B = 14000M_2^{-0.44}\text{yr} \tag{4.2.30}$$

where M_2 is in solar masses. Following the SN of the primary component the X-ray phase of the system is ceased when a time defined by either Equation 4.2.29 or 4.2.30 (depending on the donor stars evolutionary stage) has expired.

4.3 Output

4.3.1 Starburst Model

v_k	Disruption Rate, d_{SN}
$\Psi_A(v_k)$	87.23%
$\Psi_B(v_k)$	77.63%
400kms^{-1}	85.79%
300kms^{-1}	82.63%
200kms^{-1}	78.42%
100kms^{-1}	71.70%
No kick	36.08%

Table 4.2: *In order to test the dependence of the output of the population synthesis on the magnitude of the velocity kick we varied the distribution.* $\Psi_A(v_k)$ *refers to a velocity kick distribution which is a Gaussian with a mean velocity of 500kms*$^{-1}$ *and* σ*=150kms*$^{-1}$ *and* $\Psi_B(v_k)$ *refers to a distribution which is flat from 150-200kms*$^{-1}$*. We also tested the model in which all of the remnants of the primary component received no kick and kicks of 100, 200, 300 and 400kms*$^{-1}$*.*

The starburst model initially has 10,000 binaries which have parameters as set out in Section 4.2. After ~28Myrs all of the primary components have undergone a SN event which agrees well with the prescription for the stellar lifetimes in Equation 4.2.7. At this point in the model d_{SN} can be extracted. The starburst model is run with different kick velocity distributions; $\Psi_A(v_k)$ which is a Gaussian distribution, an example of which is shown in Figure 4.5, and $\Psi_B(v_k)$ which is a flat distribution between 150 and 200kms^{-1}. We also run the model with no kick velocity so that the disruption rate, d_{SN}, is completely dependent on the mass lost from the system, M_{ME}, the semi-major axis, A_f, and the orbital velocity at the time of the SN, v. As a diagnostic the model is also run for the case where all of the SN remnants receive kicks of 100, 200, 300 and 400kms^{-1}. From Table 4.2 and Figure 4.6 it is clear that the rate of disruption is dependent the magnitude of the velocity kicks (the kicks are oriented in a random direction). Where the remnant of the primary component receives no kick the disruption rate is relatively low at about 36%. Applying a small kick of ~100kms^{-1} doubles the disruption rate indicating the strong dependence of d_{SN} on the presence of a kick. For the disruption rates due to the theoretical velocity distributions ($\Psi_{A/B}(v_k)$) the kicks can disrupt between 77-88% of all the binaries in the model. Using a Gaussian distribution which can have velocities up to ≈1000kms^{-1} means that less than 13% of the binaries remain bound after the primary goes SN. If each of the disrupted binaries produces a runaway star this would lead to a runaway fraction much higher than those suggested by Dray et al., (2005), Gies (1987) and de Wit et al., (2005). However this model doesn't include the populations of stars that evolve in solitude or those that exist in very wide binaries.

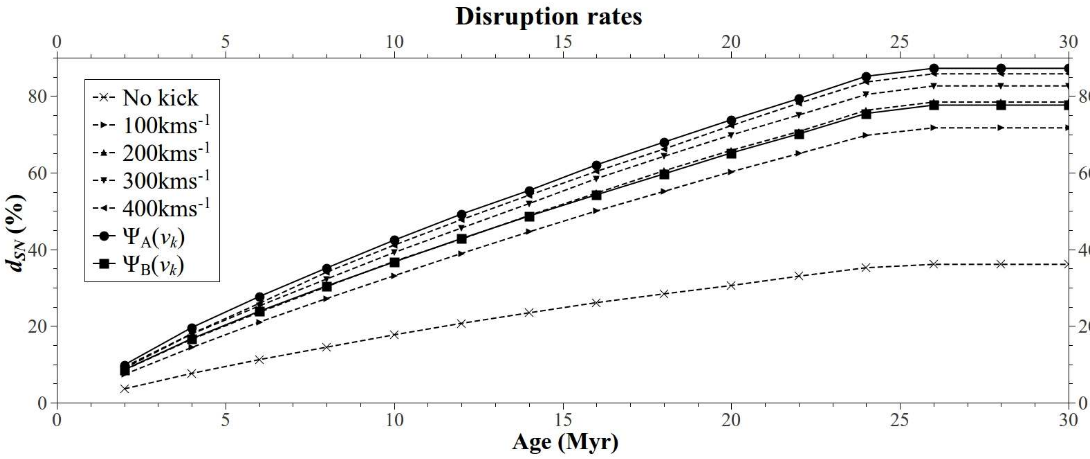

Figure 4.6: *The disruption rate, d_{SN}, is highly dependent on the magnitude of the velocity kick imparted to the remnant of the primary component in a SN. Although disruption can occur solely as the result of the loss of mass during a SN the percentage of disruptions double as a result of even a modest kick (100kms^{-1}). Here we show the disruption rates, for a number of velocity kick distributions, as a function of the age of the starburst. All the kicks are oriented in a random direction.*

4.3.2 Continuous Starburst Model

In the continuous starburst model we introduce new binaries at a specific rate. This emulates the situation across a spiral arm where star formation can be assumed to be practically constant. In this model the population of binaries reaches an equilibrium, as does the population of X-ray emitters. This allows the dynamical model to retain a population of binaries and X-ray emitters which is consistent with the binary evolution theory outline above. This model is run with the two theoretical velocity distributions defined above - $\Psi_{A/B}(v_k)$. The rate at which the model is populated is governed by the approximation of the birthrate of binaries by Iben et al., (1995)

$$dv(\mathrm{yr}^{-1}) = 0.2d\log(A)\left(\frac{dM_1}{M_1^{2.5}}\right)dq \tag{4.3.1}$$

where, as in Section 4.2, A is the semi-major axis, M_1 is the primary mass and q is the mass ratio. Taking $d\log(A)$ to be 4, dq to be 0.65 and M_1 to lie in the range of 10-100$M_\odot$ we get a binary birthrate of $1.06\times10^{-2}\mathrm{yr}^{-1}$. If the lifetimes of the primary components of the binaries are, on average, in the range 10-20Myrs the population of binaries in the starburst model will be expected to lie in the range 1.06 - 2.16×10^5. With the duration of the X-ray phase ranging from 2,000 to 100,000yrs for case A (Equation 4.2.29) and 2,000 to 8,000yrs for case B (Equation 4.2.30) the expected population of X-ray emitters lies in the range of $\sim$20-1,000 for the case

A binaries and ~20-90 for the case B binaries. The continuous starburst model

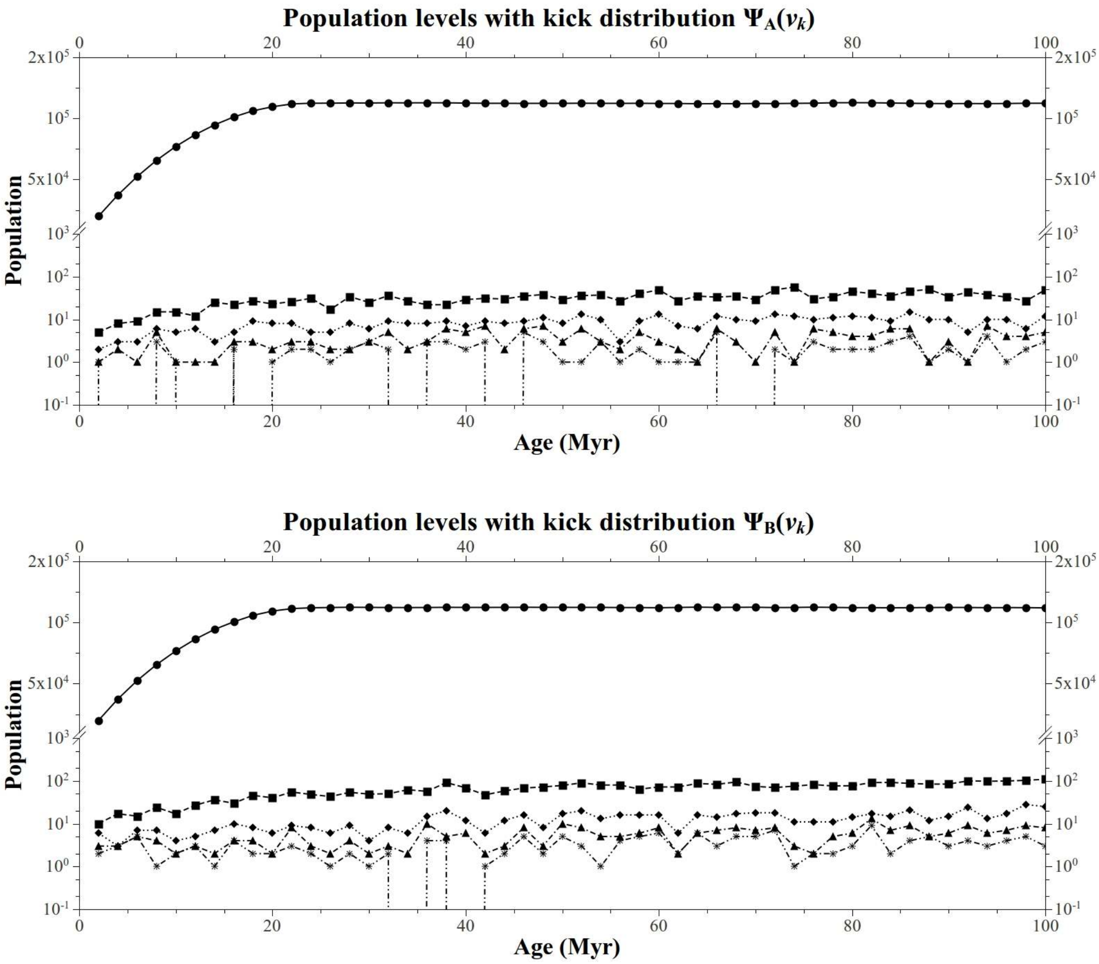

Figure 4.7: *The continuous starburst model is run with different kick velocity distributions - $\Psi_A(v_k)$ (top) and $\Psi_B(v_k)$ (bottom). In line with expectations, the total binary population (filled circles) remains at ~1.12×10 ^{5} in equilibrium. The total number of X-ray emitters (filled squares) for the $\Psi_A(v_k)$ velocity distribution levels off at between 30 and 50 but is increased for the $\Psi_B(v_k)$ velocity distribution which reflects the different disruption rates, d_{SN}, for each case. The lower lines depict the populations of X-ray emitters whose emission exceeds certain thresholds: L_X >500$L_\odot$ (diamonds), L_X >1,000$L_\odot$ (triangles) and L_X >10,000$L_\odot$.*

reaches a population equilibrium of about 1.12×10^5 objects at roughly 20Myr. For kick velocity distribution "A" ($\Psi_A(v_k)$ - the Gaussian) the total number of X-ray emitters stays in the region of between 30-50 while kick velocity distribution "B" $\Psi_B(v_k)$ allows a higher population - from about 85-110 - reflecting the dependency of the population on the disruption rate. The populations of ever more intense X-ray emitters is also looked at. We show the populations of X-ray emitters whose X-ray luminosity (defined by Equation 4.2.23) exceeds certain thresholds, namely; 500$L_\odot$ = 1.9195×10^{36}ergs^{-1}, 1,000$L_\odot$ = 3.839×10^{36}ergs^{-1} and 10,000$L_\odot$ = 3.839×10^{37}ergs^{-1}.

The number of extremely bright X-ray sources (those above $10{,}000L_\odot$) never exceeds more than ten for both kick velocity distributions.

4.4 The Dynamical Model

We use the potential and method described in Section 3.3 as the basis for the dynamical model. As in the case for the runaway model the distribution of test systems is based on the light profiles of disk galaxies. The distribution in R is defined by an exponential function:

$$I(r) = I_0 \exp\left(\frac{-r}{h_r}\right) \tag{4.4.1}$$

where $I(r)$ is the surface density of systems at r, I_0 the central surface density and h_r is the scalelength of the distribution which we tentatively set at 3.37kpc as in Section 3.2.1. We do not include a central hole in this distribution but instead set a lower limit on R of 1.5kpc and a maximum limit of 15kpc. Since we are investigating the dispersion of HMXBs from the spiral arms their distribution inside 1.5kpc is not the subject of our study although they do occur there. As can be seen from Figure 4.8 even at 2kpc binaries from both spiral arms tend to mix together and objects from both arms become inseparable. In their study of the spiral structure of HMXBs in M51 Shtykovskiy and Gilfanov (2007) also omit HMXBs in the galaxy centre (within 2.7kpc). The test systems also have a height distribution as outlined in Section 3.2.1 such that

$$I(z) = I_0 \mathrm{sech}^2\left(\frac{z}{h_z}\right) \tag{4.4.2}$$

where h_z is the scaleheight of the distribution which we take to be 0.3kpc. As in Section 3.2.1 the positions (R,z) of the test systems are defined by sets of random numbers (B_R and B_z). The position of the test particles on a spiral pattern is now found from the $R-$ position and the equation which defines a logarithmic spiral:

$$\phi(R) = -\frac{\ln(\frac{R}{r_0})}{\tan(\alpha)} \tag{4.4.3}$$

where r_0 is minimum radius - 1.5kpc and α is the pitch angle of the spiral. We rotate the spiral pattern as time, t, progresses by noting the pattern speed, Ω_p, in rads^{-1}. The model can now be populated in a rotating spiral pattern from the function

$$\phi(R,t) = -\frac{\ln(\frac{R}{r_0})}{\tan(\alpha)} + \Omega_p t \tag{4.4.4}$$

We randomly assign the test particles to one of two arms for this model by modulating Equation 4.4.4 by π.

The synthesis model described above is now used to populate the dynamical model at a rate defined by Equation 4.3.1 in order to measure the dispersions of the X-ray emitters from the spiral arms. As the dynamical model is populated each new binary system orbits the galaxy centre with a rotation speed defined by the potential (Equation 3.3.6). When the primary component of the binary explodes as a SN the resulting undisrupted systems each receive a kick of 50kms^{-1} in a random direction - the kick can have any 3D orientation. The dispersion is firstly qualitatively analysed on an R-ϕ plot (Figure 4.8). We measure the dispersions for varying pitch angles (α) and use for this purpose the kick velocity distribution $\Psi_A(v_k)$ defined in Section 4.2.2 while holding the spiral pattern speed (Ω_p) constant. We then measure the dispersion for varying Ω_p while holding α constant.

4.4.1 Constant pattern speed, Ω_p

For the purposes of investigating the effect of varying pitch angles we hold the pattern speed constant at 30kms^{-1}kpc^{-1}.

We show first how the structure of the dynamical model which includes all particles (from newly born systems to evolved X-ray emitters) evolves with time. For the first example (Figure 4.8) we use a pitch angle of $\alpha = 10°$.

Figure 4.8 shows snapshots of the dynamical model at different epochs - 1, 10 and 100Myr. From Section 4.3.2 we know that the model should reach a population equilibrium at roughly 20Myr. At 1Myr the model systems are still tightly correlated with the spiral and there is indeed little apparent deviation from this as one progresses to 10 and 100Myr. In the top panel the 100Myr "snapshot" does show some distortion from the perfect (infinitesimally thin) spiral arm. The most notable change is the "mixing" of systems close to the galaxy centre where objects from both spiral arms are now inseparable. The extent of the "central mixing" is not obvious in the top 10Myr snapshot but by inspecting the R-ϕ plot for the same epoch it is evident in the spreading out of points at small R. In the R-ϕ plots each logarithmic line represents a distinct arm and in the 100Myr plot it is clear that systems from one arm have indeed mixed with the other. There is less deviance from the arms as one moves outwards from the centre and the pattern speed approaches the circular rotation speed of the potential (ie. at the co-rotation radius, 7.3kpc see Table 4.1).

The systems then move away from the arms again in the very outer parts as they lag behind the spiral arm. The spiral arm progresses with its constant characteristic pattern speed (rads^{-1}) while the stellar systems progress according to their rotational velocity (kms^{-1}) which is almost constant for all R. This means that systems that "lag" behind a spiral arm should do so in a circular arc centred on the galaxy centre. For spirals with a small pitch angle the pattern produced by systems lagging behind (which essentially has a pitch angle of 0° - ie. circular) is not immediately apparent since it closely resembles the "almost" circular spiral pattern. This dispersion of systems beyond the co-rotation radius is therefore more apparent in spiral systems with greater pitch angles which is evident in Figure 4.9 where the pitch angle has been increased from 10° to 20° and even more so in Figure 4.10 where a pitch angle of 30° has been used.

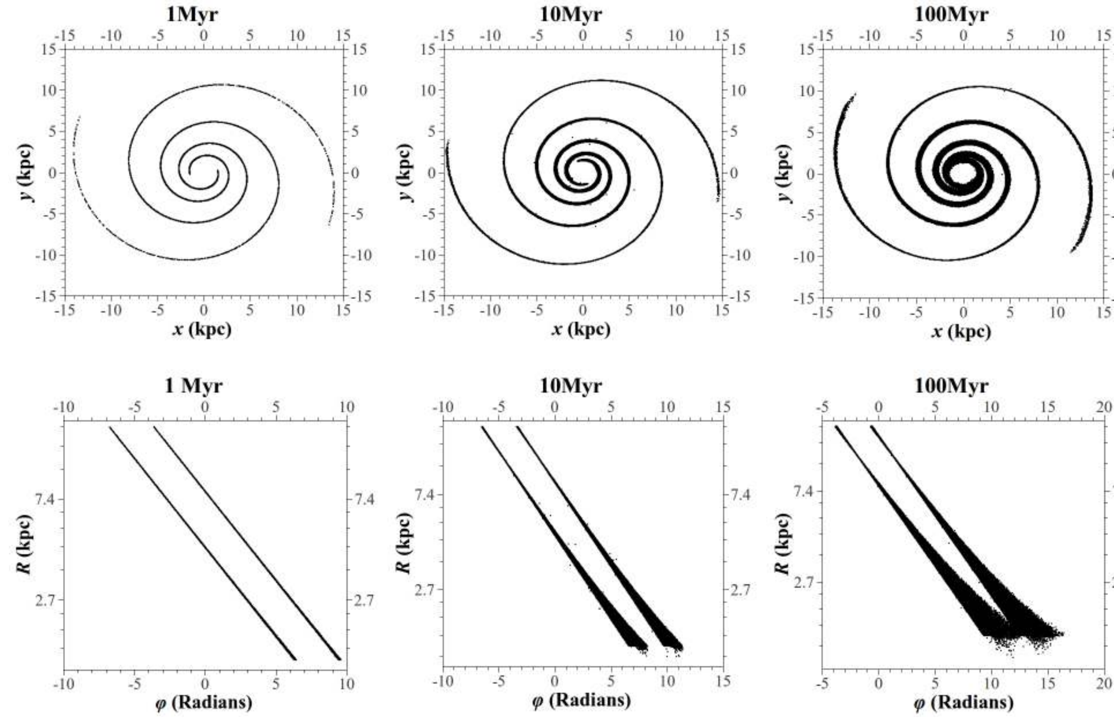

Figure 4.8: *For a pitch angle of α = 10° and a pattern speed of Ω_p = 30kms^{-1}kpc^{-1} the top set of figures shows the structure of the dynamical model at different epochs; 1, 10 and 100Myr. These plots include all systems, from newly added binary systems to HMXBs. The spiral structure is still present long after the model has reached a population equilibrium (~ 20Myr) however dispersion from the arms is evident at 100Myr. The most notable feature is the mixing in the centre of the galaxy. The bottom plots show R-ϕ plots of the positions of the systems. In these plots the ϕ dispersion of the systems from the arms becomes much clearer and the onset of the central mixing is apparent even at 10Myr.*

The following pages depict the positions of X-ray emitters (red dots) as defined by the prescription in Section 4.2.3 in relation to the pre-SN binary systems (black dots) for different epochs along with their respective populations. Figures 4.11, 4.13 and 4.15 show how the model begins for pitch angles of 10, 20 and 30° respectively. The

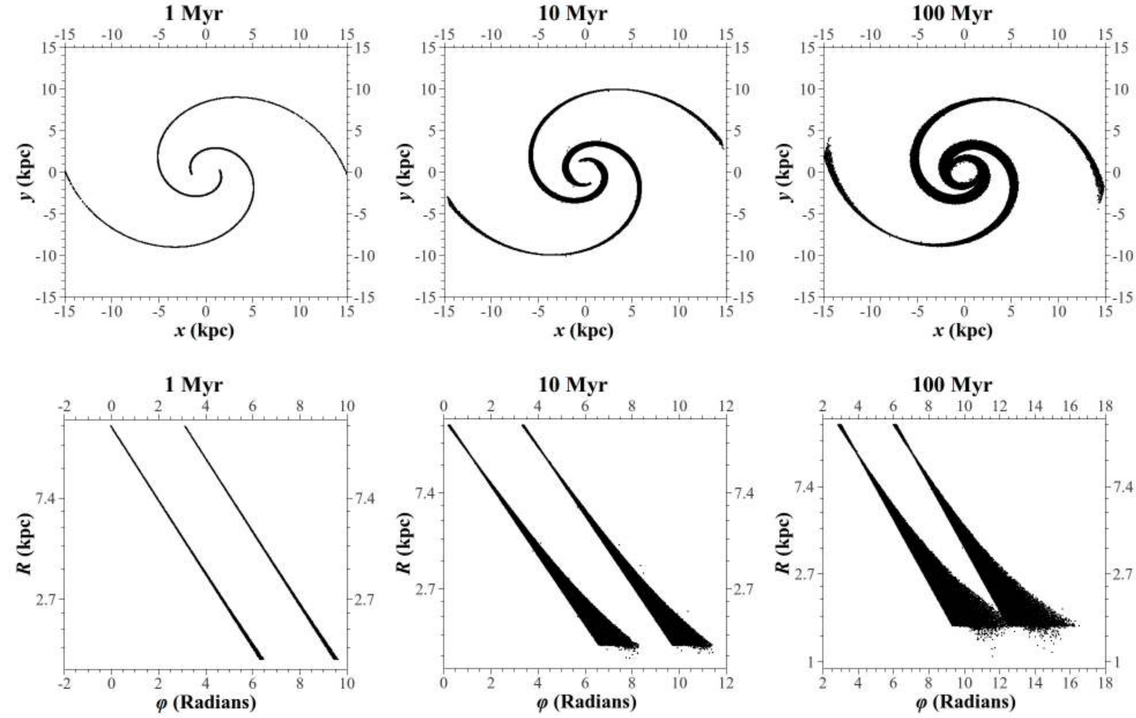

Figure 4.9: *While the central mixing is equally as apparent as in Figure 4.8 the dispersion in the outer arms is more noticeable due to the increased pitch angle of 20°.*

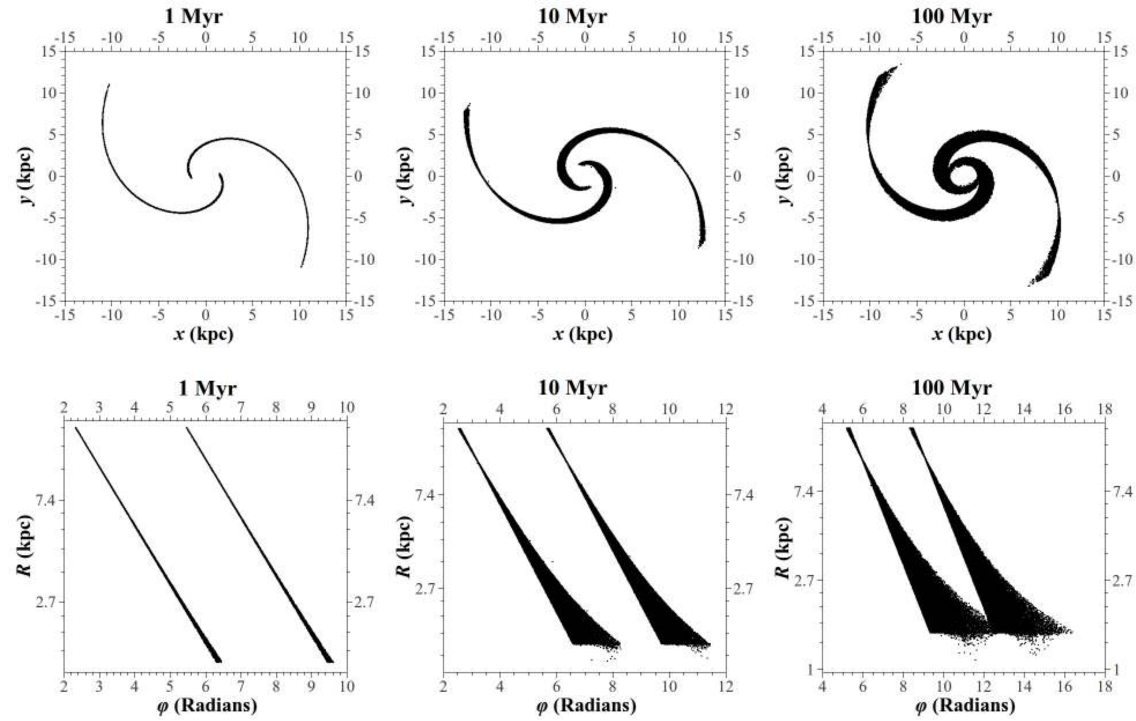

Figure 4.10: *The dispersion of systems past the co-rotation radius is most apparent for the spiral with $\alpha = 30°$.*

density of systems is higher at small R - a consequence of the the radial distribution function (Equation 4.4.1) - which consequently leads to more X-ray emitters in the central regions as can be seen from the "snapshots" from 0.5-5Myr. Kennicut (1983) describes a star formation rate (SFR) that is is an exponentially decaying function of radial distance while more recently the multi-wavelength study of M33 by Verley et al., (2009) suggests that the SFR of young stars in that galaxy declines with radius (with scalelength 2kpc). We note however that the SFR in galaxies has been traditionally parameterised by the surface density of gas (Schmidt, 1959) or the dynamical timescales (Shu, 1973). We therefore suggest that the populations of HMXBs in the outer regions of our model galaxies may be underestimated. As the model reaches equilibrium ($\sim$20Myr) this central concentration is apparent as is the apparent lack of dispersion of X-ray emitters, even with a kick, from the spiral pattern produced by the pre-SN systems (see Figures 4.12, 4.14 and 4.16). For the case of a pitch angle of 10° we see almost no dispersion of the pre-SN binaries from the thin spiral arms. In some cases a HMXB can be seen separate from the arm (see Figure 4.12 - 60Myr). This suggests that for low pitch angles neither the young stellar or HMXB populations will deviate much from the spiral pattern. For this reason, HMXBs with a large space velocity may travel to areas distinct from arms with a low pitch angle. For the case of a pitch angle of 20° the pre-SN binaries tend to disperse more from the logarithmic spiral and indeed the HMXBs follow suit. The X-ray sources however, even with a high space velocity, become less separated from the binaries (see Figure 4.14). For even greater pitch angles this effect is compounded (Figure 4.16) suggesting that although the dispersion from an infinitesimally thin spiral is greatest for higher pitch angles, it also becomes less likely to find the HMXBs separated from the light due to young stars (eg. Hα). It should also be noted that for higher pitch angles the co-rotation radius becomes ever clearer (by the reduction in the width of the arms at this point). This implies that dispersions from a thin spiral in (well behaved) spiral galaxies could provide a diagnostic for the determination of the pattern speed in the galaxy (provided a rotation curve has been defined).

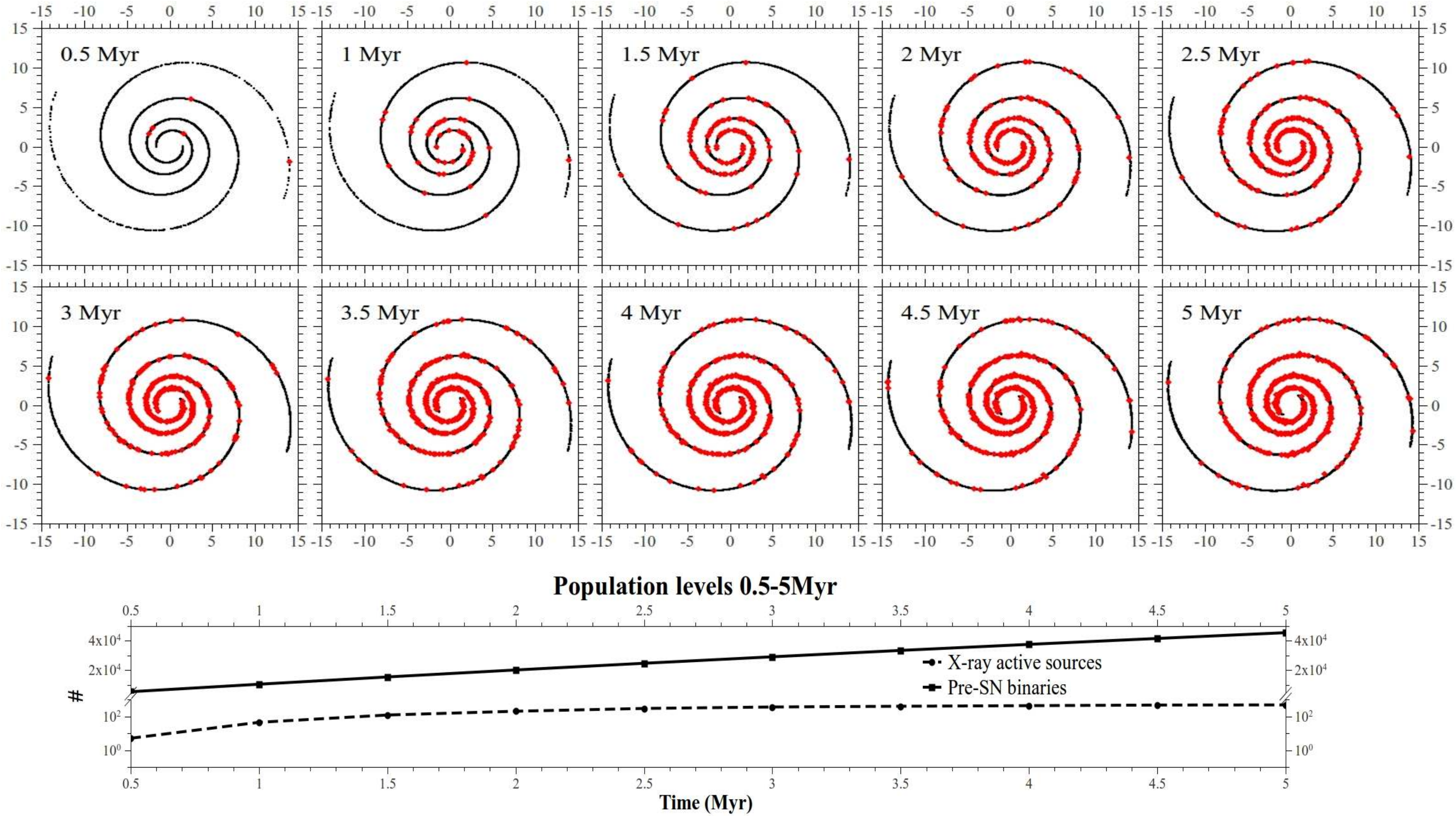

Figure 4.11: *HMXBs (red dots) plotted with the population of pre-SN systems (black dots) from the model for a pitch angle of 10° at epochs from 0.5-5Myr.*

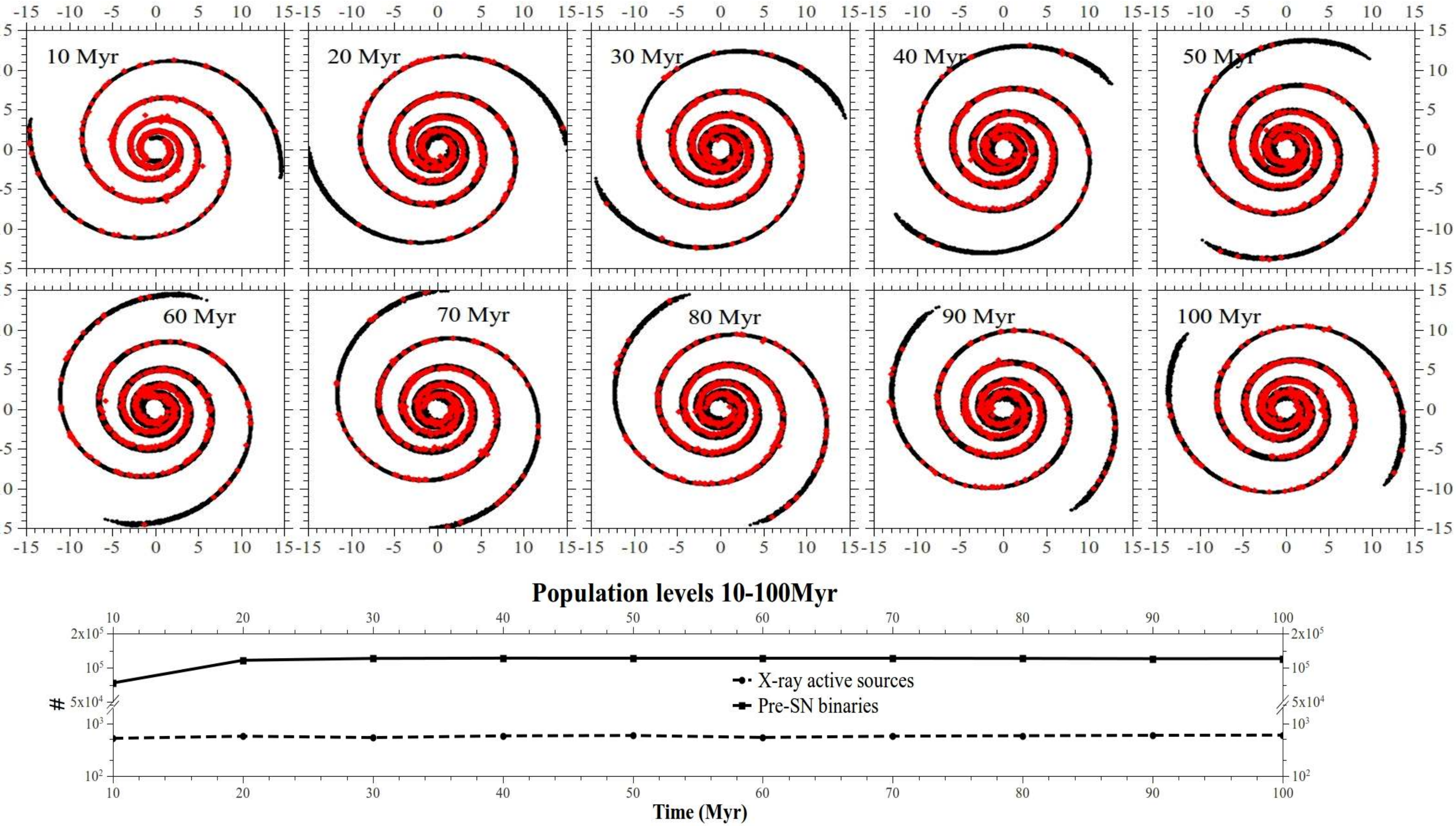

Figure 4.12: *HMXBs (red dots) plotted with the population of pre-SN systems (black dots) from the model for a pitch angle of 10° at epochs from 10-100Myr.*

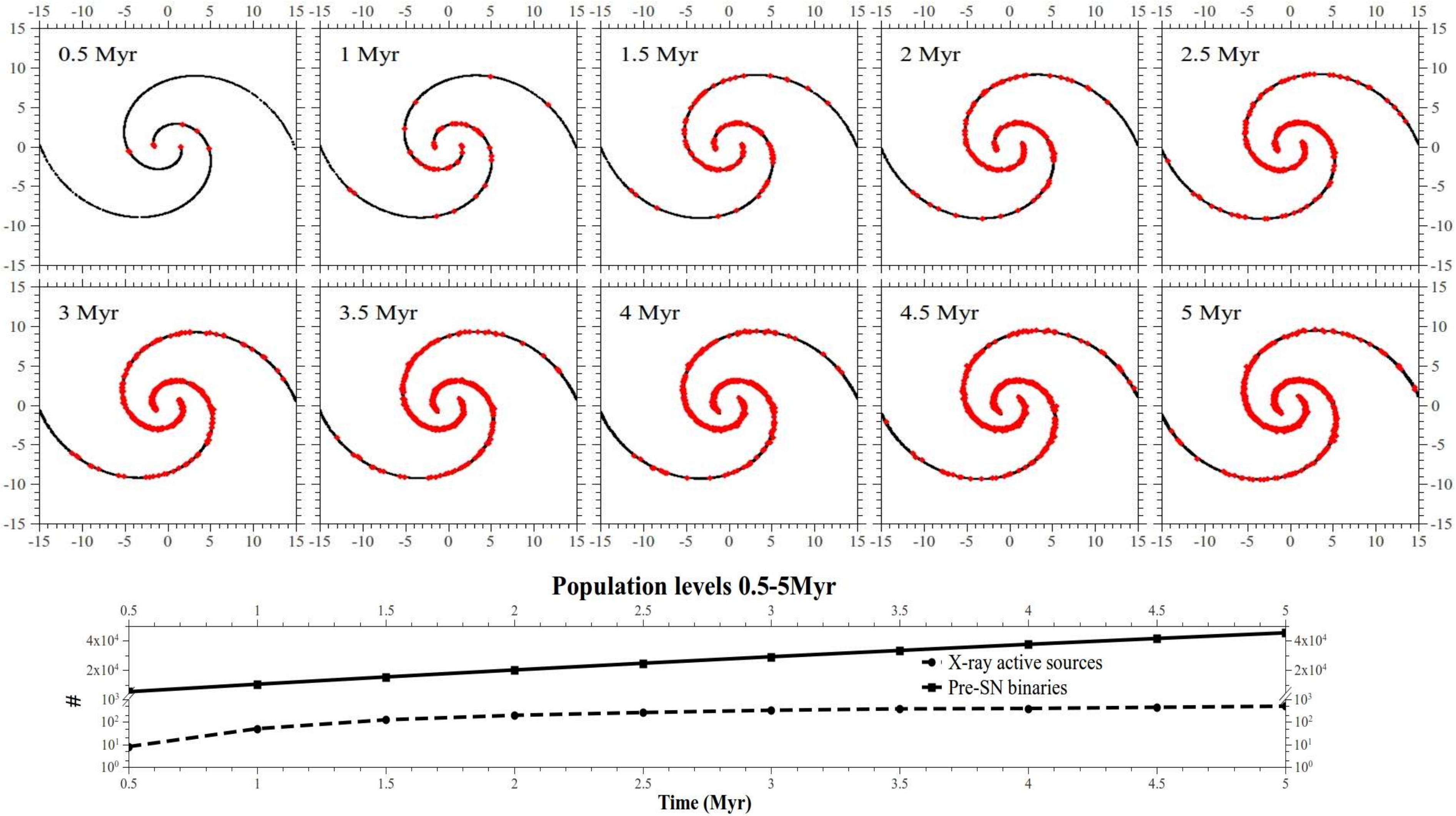

Figure 4.13: *HMXBs (red dots) plotted with the population of pre-SN systems (black dots) from the model for a pitch angle of 20° at epochs from 0.5-5Myr.*

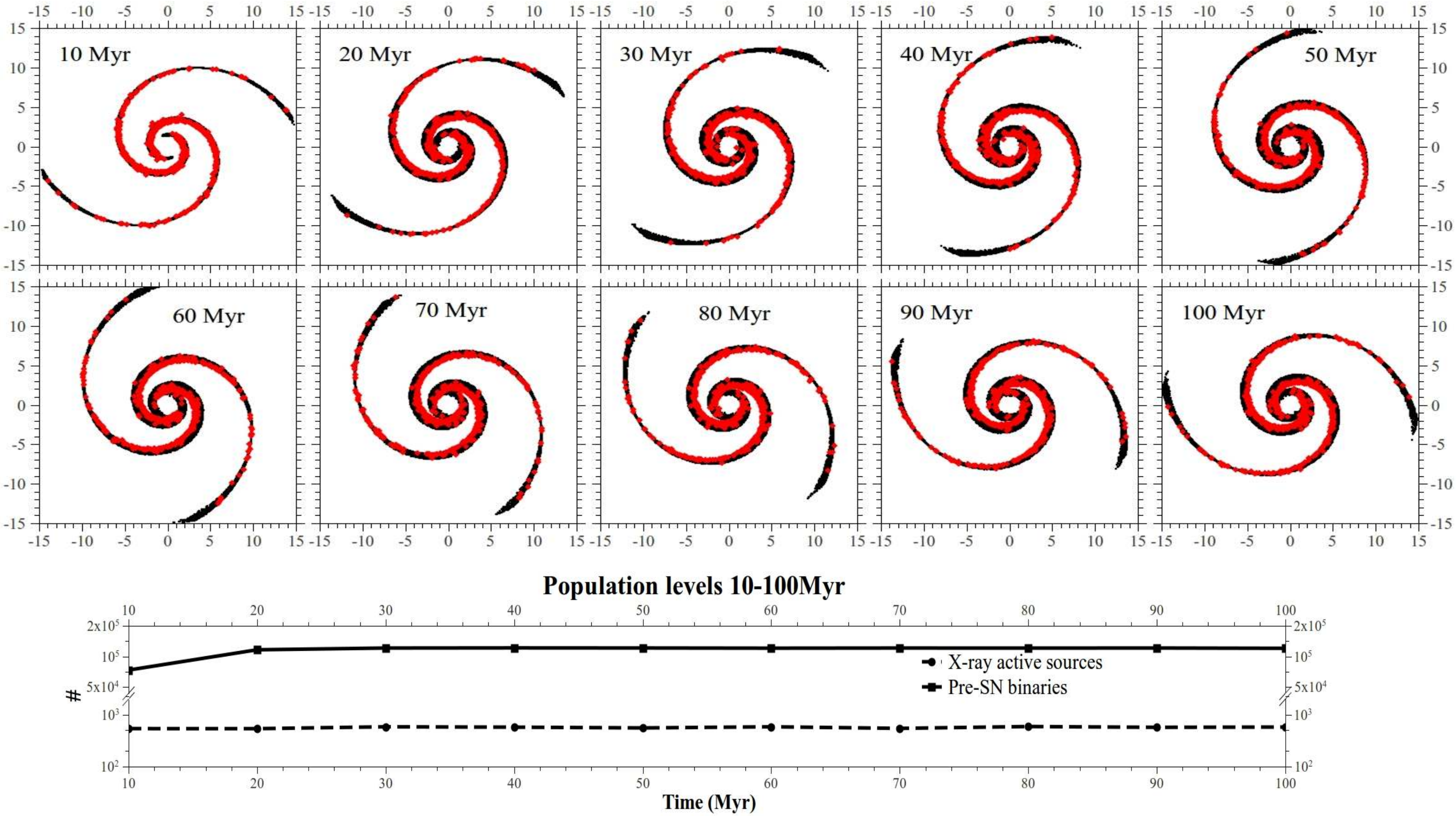

Figure 4.14: *HMXBs (red dots) plotted with the population of pre-SN systems (black dots) from the model for a pitch angle of 20° at epochs from 10-10Myr.*

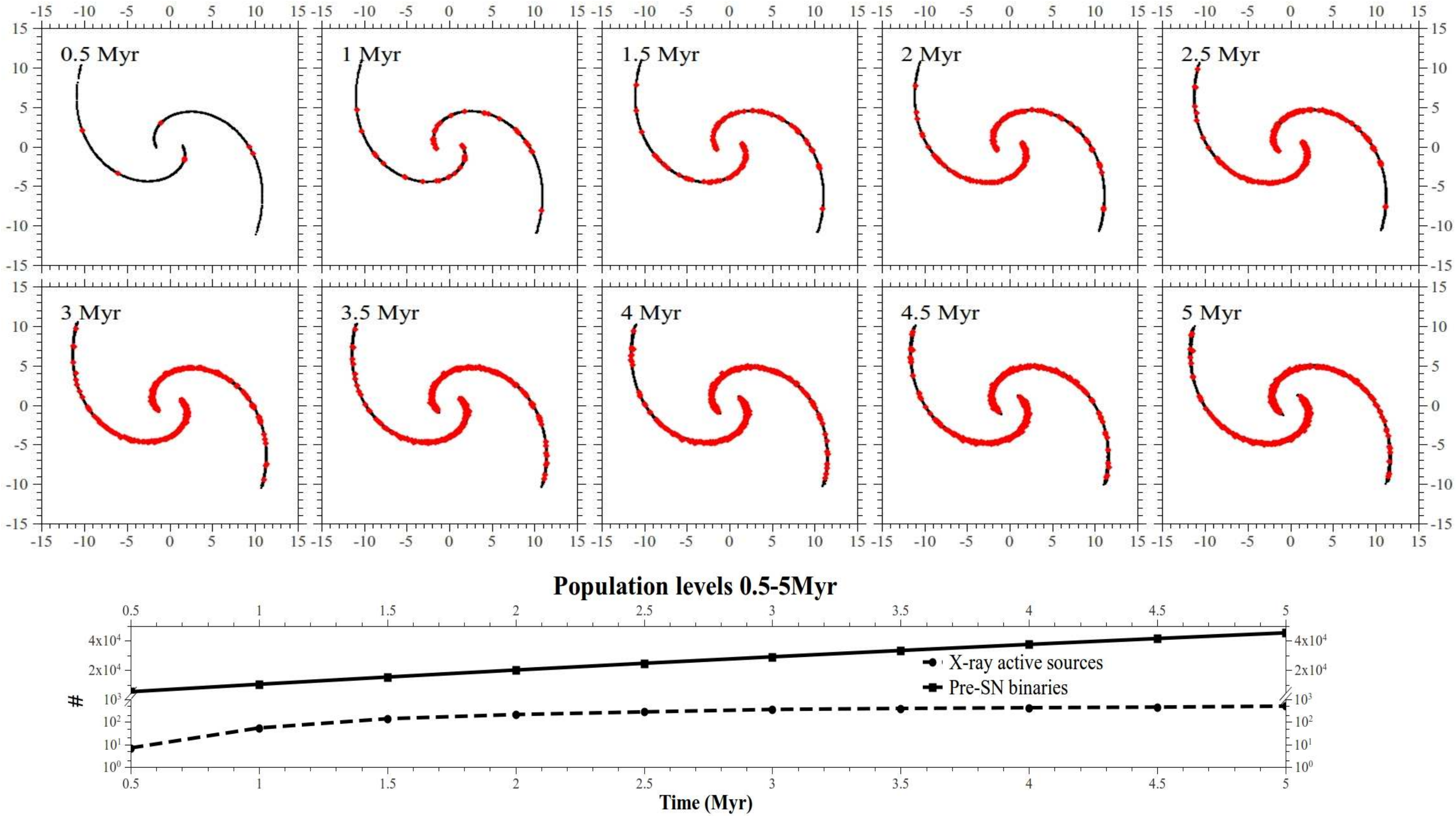

Figure 4.15: *HMXBs (red dots) plotted with the population of pre-SN systems (black dots) from the model for a pitch angle of 30° at epochs from 0.5-5Myr.*

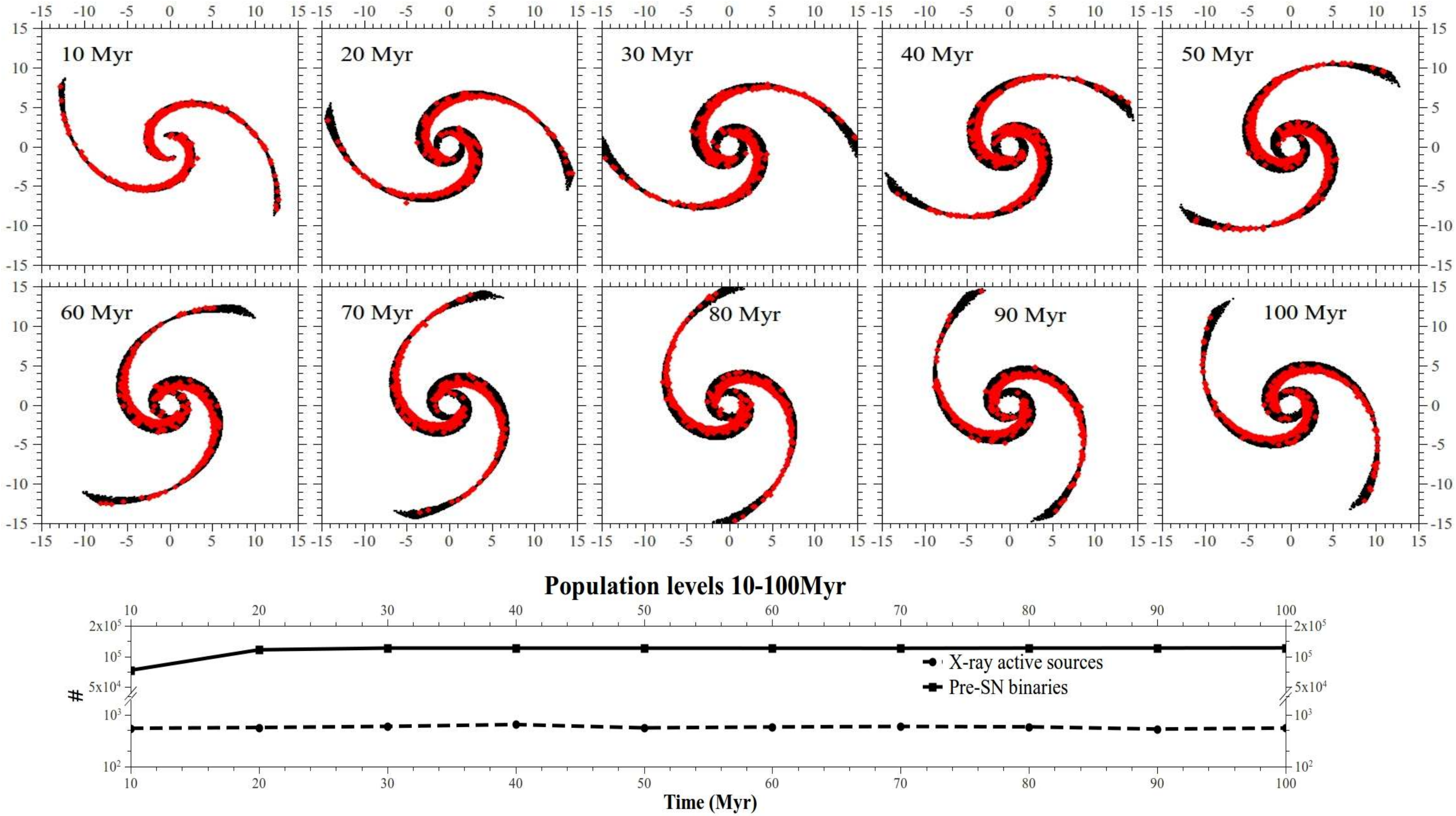

Figure 4.16: *HMXBs (red dots) plotted with the population of pre-SN systems (black dots) from the model for a pitch angle of 30° at epochs from 10-100Myr.*

As the populations of X-ray emitters is quite low (<1,000) we collect the positions of these emitters at 0.5Myr year intervals up to 100Myr to create an increased sample of positions. These positions are then modulated (in ϕ) via their epoch and the pattern speed of the spiral so that they occupy the same region of space in the polar coordinate system (ie. if τ is the epoch of the recorded position of ϕ then we subtract $\tau\Omega_p$ from ϕ). This increased sample allows a better determination of the dispersion of HMXBs from the spiral arms as it includes a range of possible positions. This distribution of HMXB positions then necessarily includes positions of the same HMXBs at different epochs as is evident in the trajectories of HMXBs emanating from the spiral arm (eg. Figure 4.17). We plot the increased sample of HMXB positions (black dots) over the positions of pre-SN systems at 100Myr (red dots). The positions of pre-SN systems at 100Myr is taken as a reference since at this point the model is in equilibrium and gives a representative view of the expected distributions of young stars about a spiral arm for each respective pitch angle (and consequently Hα emission). It is apparent, even with this larger sample of HMXB positions, that HMXBs do not tend to travel very far from their birthplace in the spiral arms. In fact, it could be suggested that HMXBs represent a good tracer for star forming regions in spiral galaxies. The dispersion from the spiral arms is most notable in Figure 4.17 as the tracks protruding from the spiral arm (note we switch that colour code in an effort to improve the contrast between the populations: red dots - pre-SN binaries, black dots - HMXBs). The low pitch angle in this case keeps the spiral arms from getting very wide making the dispersion of HMXBs clearer whereas for the higher pitch angles (Figures 4.18 and 4.19) the spiral arms are much thicker, hiding the movement of HMXBs from the arm.

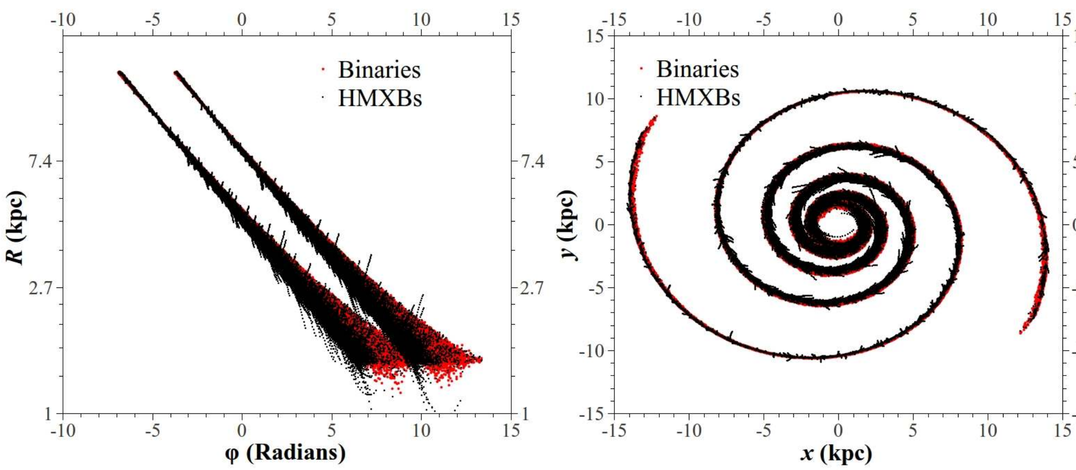

Figure 4.17: *For a pitch angle of 10° an increased sample of HMXB positions (black dots) is plotted over the positions of pre-SN systems at 100Myr (red dots). The dispersion of HMXBs is apparent in the many "tracks" coming out of the spiral arms.*

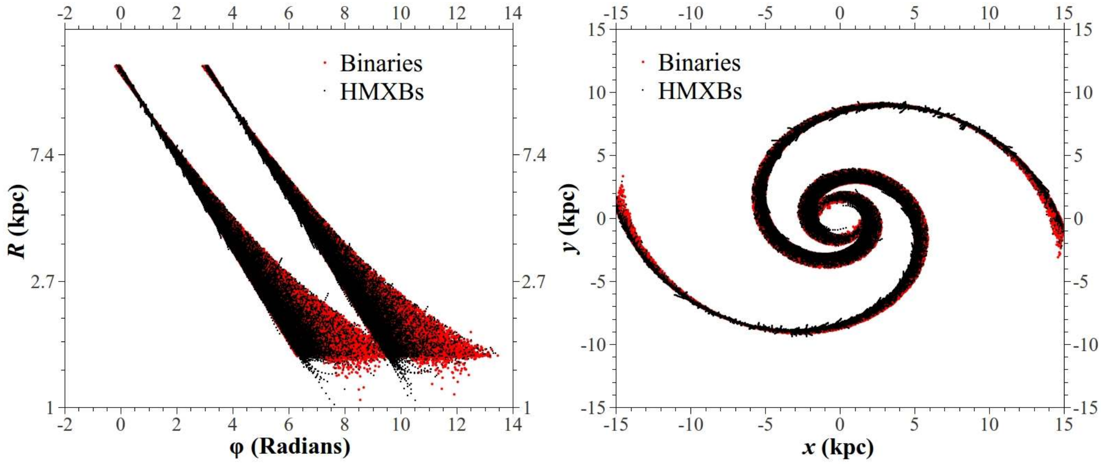

Figure 4.18: *Here we plot the increased sample of HMXB positions for the case of a spiral pitch angle of 20°.*

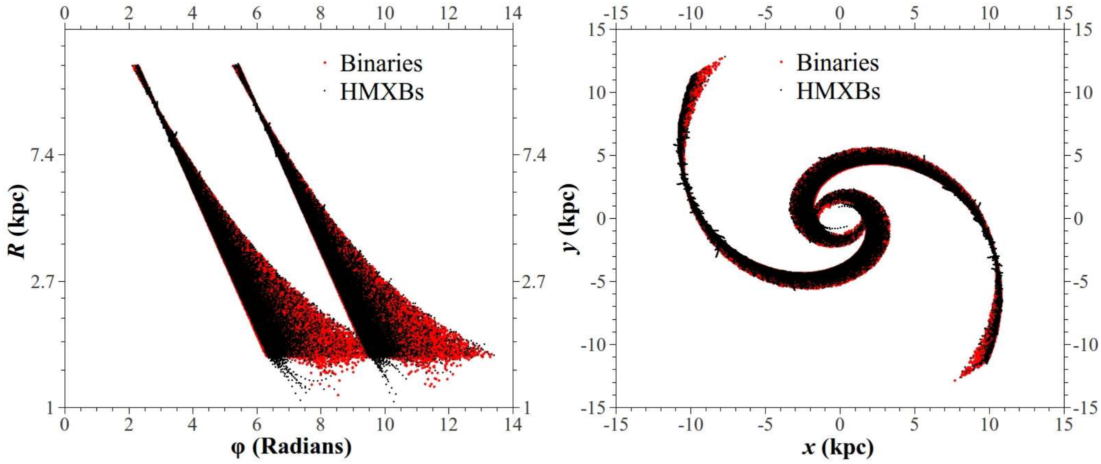

Figure 4.19: *Here we plot the increased sample of HMXB positions for the case of a spiral pitch angle of 30°.*

To quantitatively measure the dispersion of the population from the spiral arms we measure the distribution in ϕ for the increased sample of HMXBs (those modulated by $\tau\Omega_p$) and pre-SN systems (at 100Myr) which lie in distinct ranges of R. These distributions are then fit with multi-peak Gaussian curves. The variance in these distributions is then plotted as a function of R. This gives a measure of how “dispersed” the systems are as one moves out along the spiral arm.

We plot histograms of ϕ-values for those HMXBs and pre-SN systems in the range R =1-2kpc. These distributions are then fit with a curve representing the sum of two Gaussian distributions (see Figure 4.21). The variance, σ, is then a measure of the dispersion from the spiral arms of the systems within a radial distance of 1-2kpc. This is then done for the systems with a radial distance in the range 2-3kpc, 3-4kpc etc. out to ∼15kpc (the maximum radial distance) so that we end up with a set of variances measuring how the systems become dispersed as a function of radial distance R. For the $\alpha = 10°$ dataset from above we plot the distributions in Figure 4.21. In each plot is listed the variance, σ, of the Gaussian fit for both spiral arms. For those systems within 1-2kpc the central mixing manifests itself as one of the spiral arms having a wider distribution than the other. Although this mixing is symmetric the arms originate (at $\tau = 0$Myr) at $\phi = 0$ and π and consequently the distributions on the $R-\phi$ plot lead to the second arm (which originates at π) "acquiring" binaries from the first. Also, those systems within the range of 2-3kpc have an even wider distribution in ϕ than those in the range 1-2kpc. One would expect that the more central systems would have a wider distribution (due to the increased rotational velocity) but due to the spiral arms having a starting radius of 1.5kpc the population of systems within 1-2kpc (16,291) is less than two thirds the population between 2-3kpc (25,623). The variance in the distributions then systematically drops as one moves out to greater R. As the effects of mixing are diminished in the outer regions the variance in the distributions from both arms tend to equalise. However, this coherence is marginally lost in the very outer regions as the population levels drop and identical fits become less probable. We make these plots for all three pitch angles (the plots for $\alpha = 20°$ and 30° are shown in Figures B.2 and B.4 in Appendix B respectively). The dispersion along the arms are then plotted in Figure 4.22. It can be seen that the dispersions in ϕ are generally lower for spirals with higher pitch angle as expected but also that the dispersions of HMXBs is tightly correlated with those of the young stellar population for the lowest pitch angle. This correlation is decreased with increasing pitch angle and suggests that, in general, the distribution of HMXBs should be thinner than that of young stars.

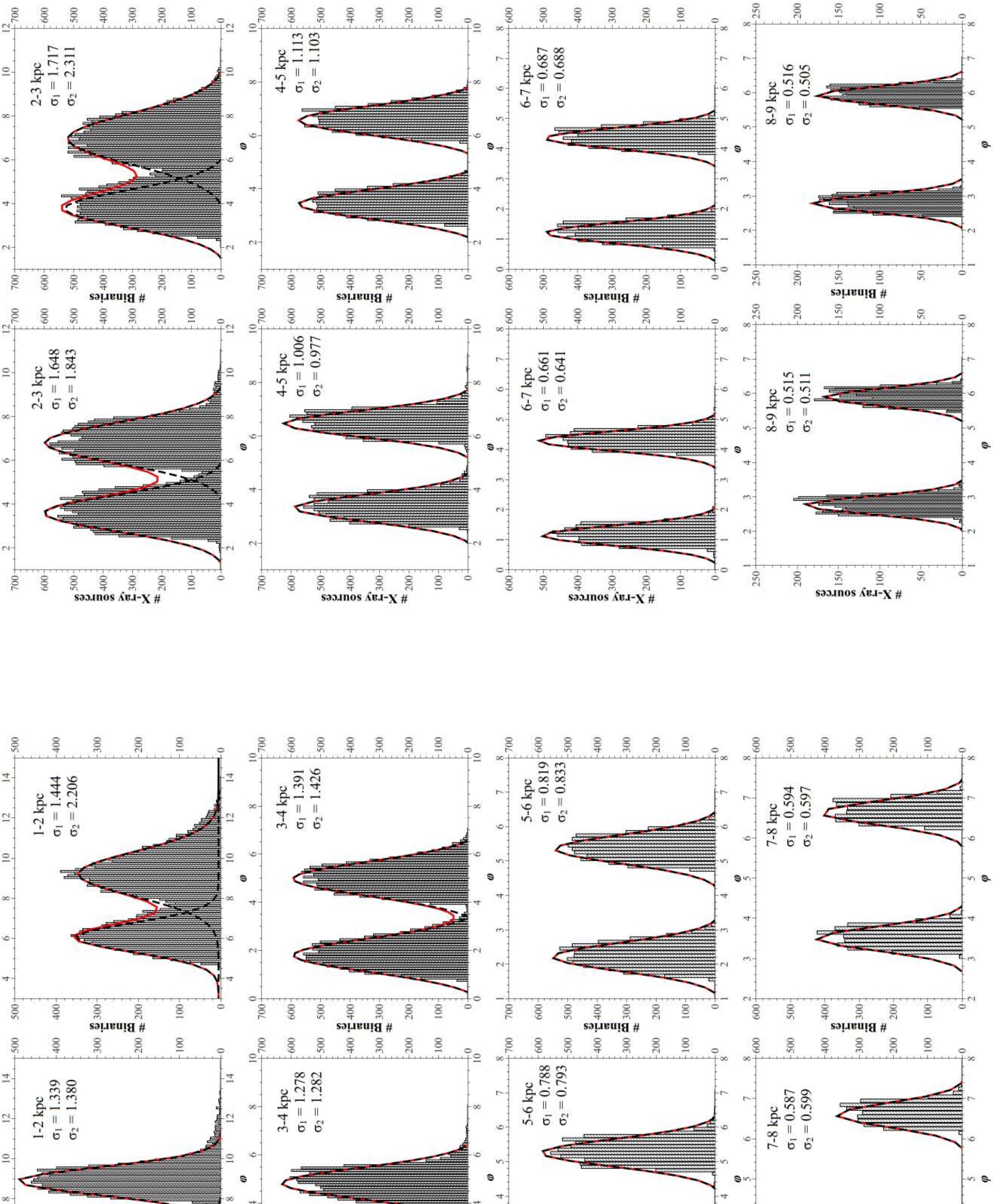

1-2 kpc
σ1 = 1.339
σ2 = 1.380
1-2 kpc
σ1 = 1.444
σ2 = 2.206
3-4 kpc
σ1 = 1.278
σ2 = 1.282
3-4 kpc
σ1 = 1.391
σ2 = 1.426
5-6 kpc
σ1 = 0.788
σ2 = 0.793
5-6 kpc
σ1 = 0.819
σ2 = 0.833
7-8 kpc
σ1 = 0.587
σ2 = 0.599
7-8 kpc
σ1 = 0.594
σ2 = 0.597
2-3 kpc
σ1 = 1.648
σ2 = 1.843
2-3 kpc
σ1 = 1.717
σ2 = 2.311
4-5 kpc
σ1 = 1.006
σ2 = 0.977
4-5 kpc
σ1 = 1.113
σ2 = 1.103
6-7 kpc
σ1 = 0.661
σ2 = 0.641
6-7 kpc
σ1 = 0.687
σ2 = 0.688
8-9 kpc
σ1 = 0.515
σ2 = 0.511
8-9 kpc
σ1 = 0.516
σ2 = 0.505
X-ray sources
Binaries
φ

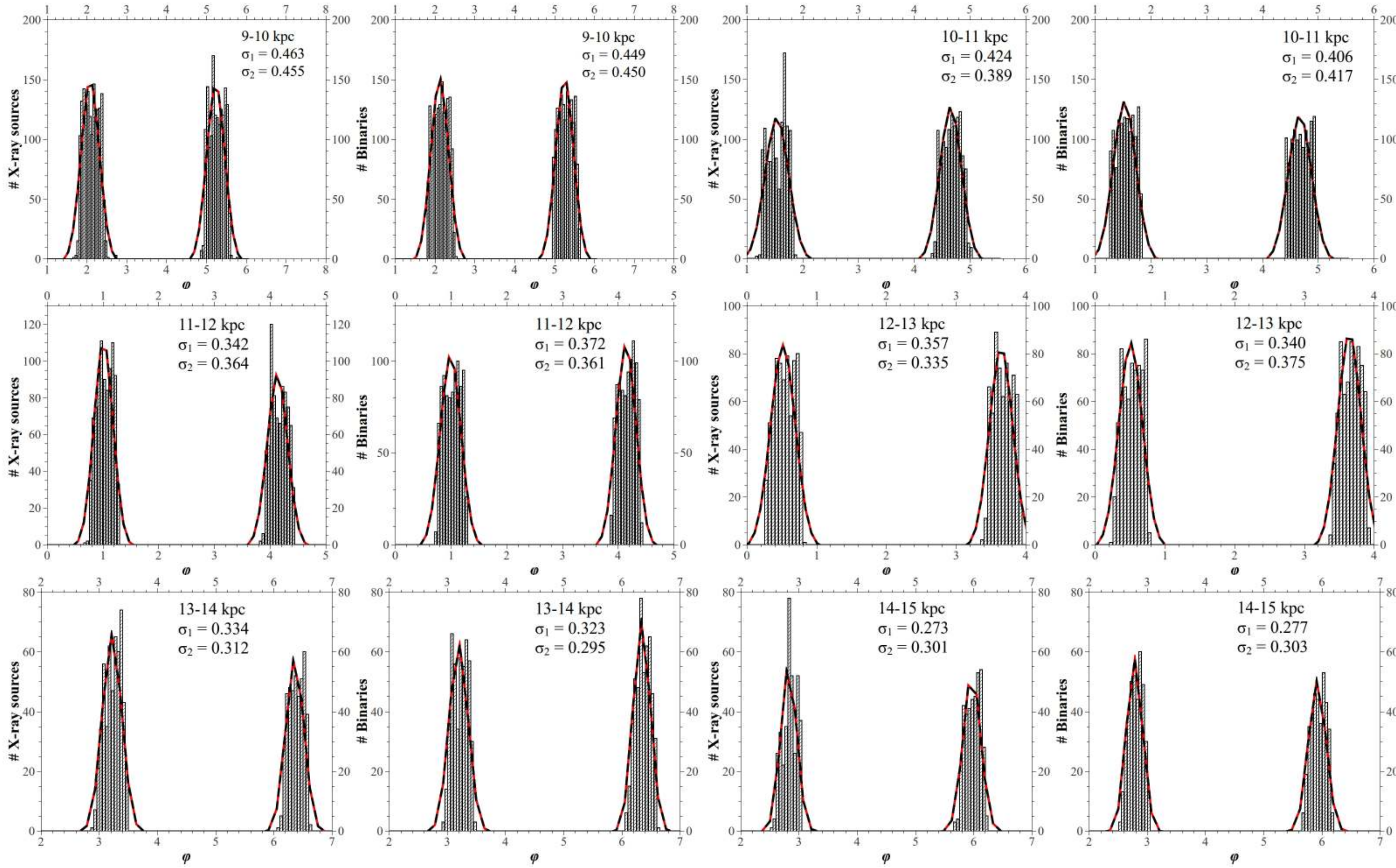

Figure 4.21: *For systems in distinct radial distance bins (eg. 1-2kpc, 2-3kpc, etc.) the distribution of ϕ-values for both the increase sample of HMXBs and the pre-SN systems at 100Myr are plotted. These distributions are then fit with a double peaked Gaussian curve. The variance, σ, for each of the fits is listed (one for each arm - subscript 1 refers to the left arm) and is a measure of the dispersion of the systems from the spiral arm. The dispersion is greatest in the galaxy centre and decreases outwards but at the very centre mixing causes one arm to exhibit a greater dispersion than the other. As this mixing effect decreased as greater radial distances the dispersions in both arms tends to equalise.*

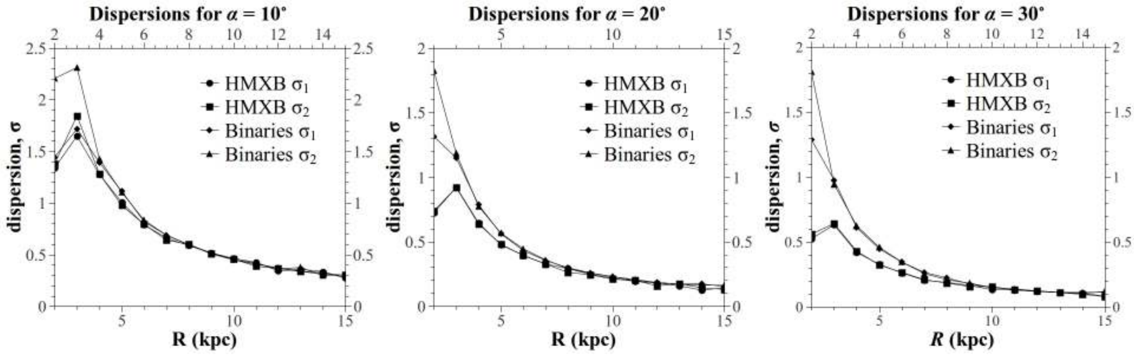

Figure 4.22: *The dispersions from Figures 4.21, B.2 and B.4 are gathered here and plotted as a function of radial distance. Increasing pitch angles mean that the dispersions will be generally lower for spirals with a high pitch angle. For the case of a pitch angle of 10° there is no great difference in the distributions of HMXBs and the pre-SN binaries. This difference increases with increasing pitch angle with HMXBs having a lower dispersion than the pre-SN binaries.*

4.4.2 Constant pitch angle, α

In this section we investigate the dispersions for varying pattern speeds while holding the pitch angle constant at 20°. We use pattern speeds of 10kms^{-1}kpc^{-1} and 50kms^{-1}kpc^{-1} for this purpose (Note that the dispersions can be compared with the dispersions from Figure 4.9 which also has a pitch angle of 20° but a pattern speed of 30kms^{-1}kpc^{-1}). These pattern speeds have co-rotation radii at 23.4kpc and 3.9kpc respectively (see Table 4.1). As in the previous section we firstly qualitatively describe the dispersions of all objects in the model from the spiral arm at epochs of 1Myr, 10Myr and 100Myr (see Figures 4.23 and 4.24). The major difference from above is that in the case 10kms^{-1}kpc^{-1} pattern speed the co-rotation radius lies well beyond the maximum radial extent of the objects in the model. For this reason all of the objects move ahead of the spiral pattern and the thickening of the spiral arm sets in much quicker. In the case of a pattern speed of 50^{-1}kpc^{-1} the co-rotation radius is clearly apparent in the 100Myr plots and is already seen in the 10Myr plots making spirals with high pattern speeds a good diagnostic in determining the co-rotation radius. As in the case for the previous section the central mixing of objects is also evidenced in these snapshots.

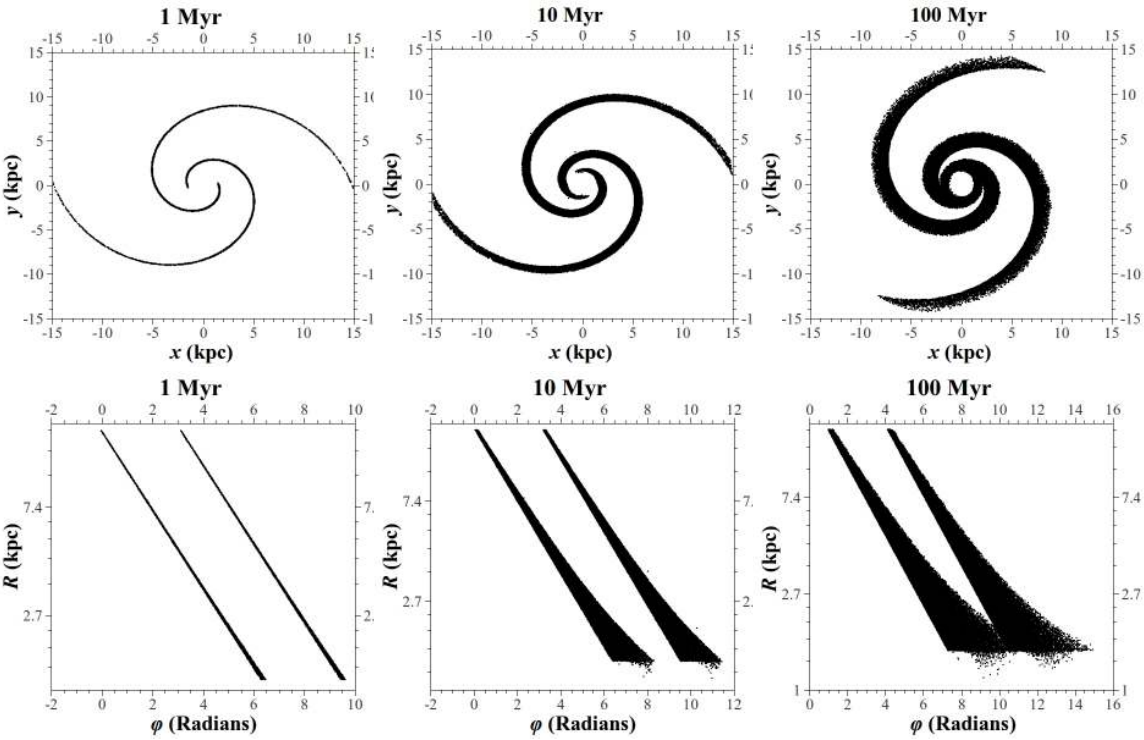

Figure 4.23: *For a pattern speed of 10kms^{-1}kpc^{-1} we show here the progression of the dispersion of objects in the model (both newly formed binaries and HMXBs) from the spiral arms. The co-rotation radius for this case lies well beyond the maximum radial distance in the model at 23.4kpc. Because of this the objects move ahead of the spiral pattern at all radii and results in much thicker arms.*

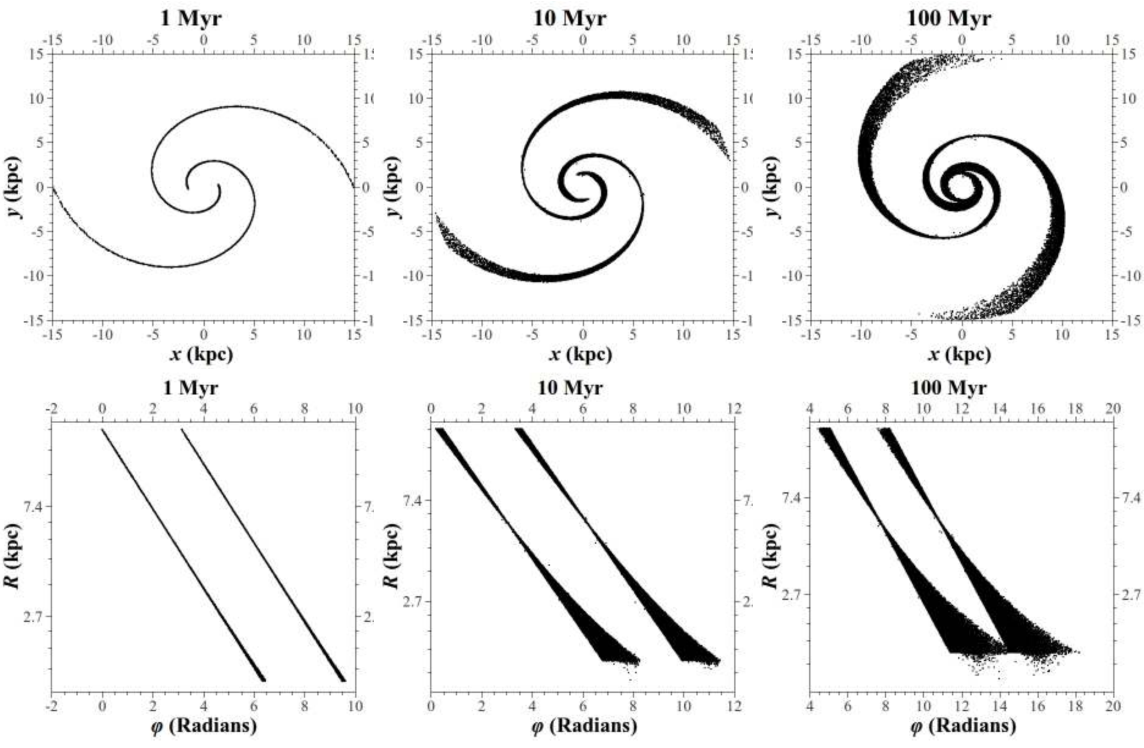

Figure 4.24: *As above, here we present the progression of the dispersion of objects in the model with a pattern speed of 50kms^{-1}kpc^{-1}. The co-rotation radius in this case is at 3.9kpc and can be seen already at 10Myr in the apparent thinning of the spiral arms.*

We plot on the following pages the positions of the HMXBs compared to the population of pre-SN binaries at different epochs. As in the case for all of the varying pitch angles the population of HMXBs is tightly correlated with the spiral arms up to 5Myr. However, when the model has reached equilibrium (after 20Myr) we notice that for a low pattern speed (Figure 4.25) the HMXBs are closer to the spiral arms than the population of pre-SN binaries. The orbital rotation of the pre-SN binaries is much greater than the pattern speed for the range of radii here and results in thick arms being formed. HMXBs can be found in any part of the arms but are preferentially placed close to the thin spiral. For this reason we suggest that HMXBs won't, in general, be placed away from the light of young stars in spirals with low pattern speed. On the other hand, for the case of spirals with high pattern speed we see that the thickness of the arms is at a minimum at small galactocentric radii and in these places the high space velocity of the HMXBs allows the to travel appreciably away from the population of pre-SN binaries at the co-rotation radius (see Figure 4.28 - 60/70Myr).

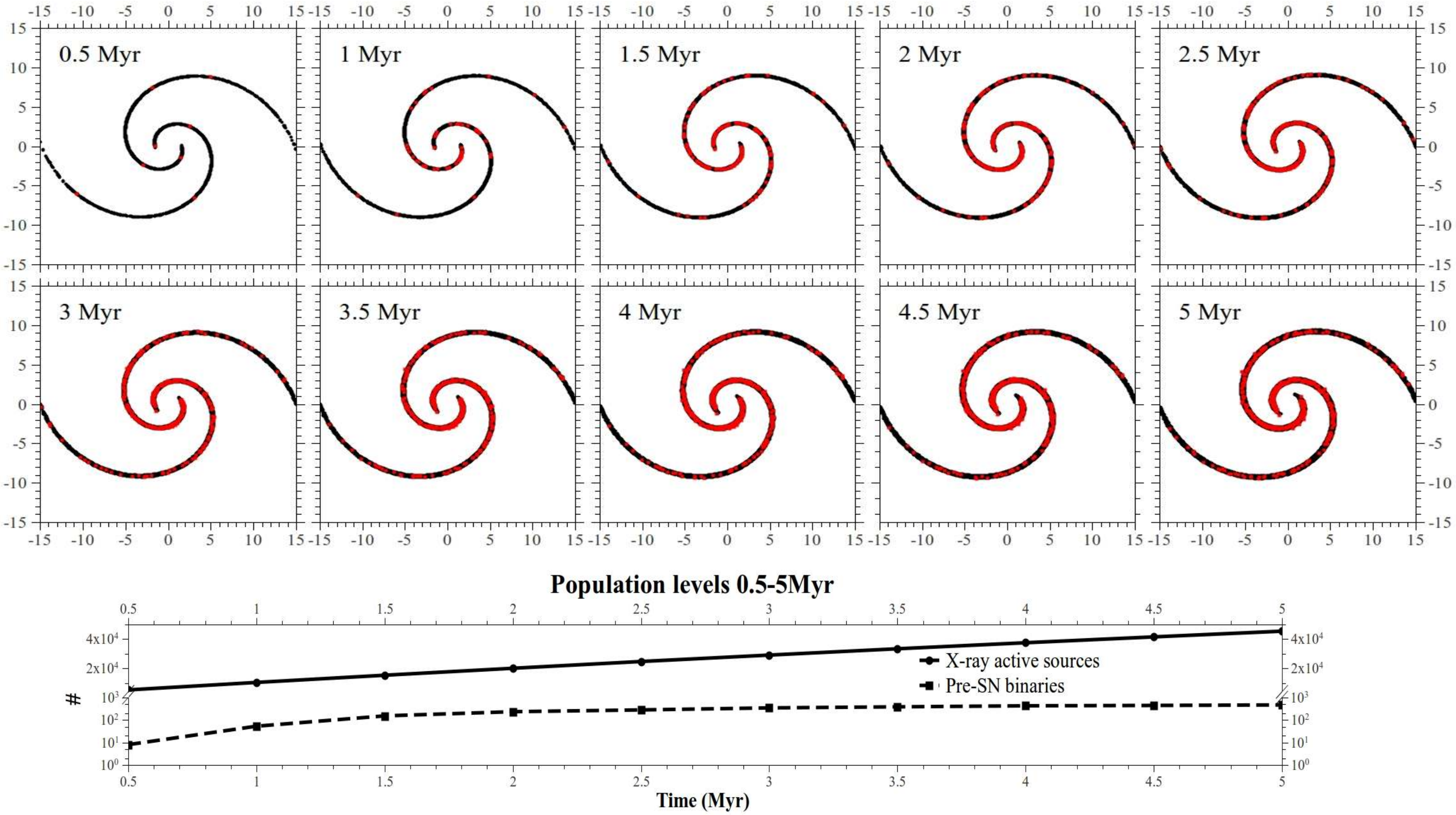

Figure 4.25: *HMXBs (red dots) plotted with the population of pre-SN systems (black dots) from the model with a pattern speed of 10kms^{-1}kpc^{-1} at epochs from 0.5-5Myr.*

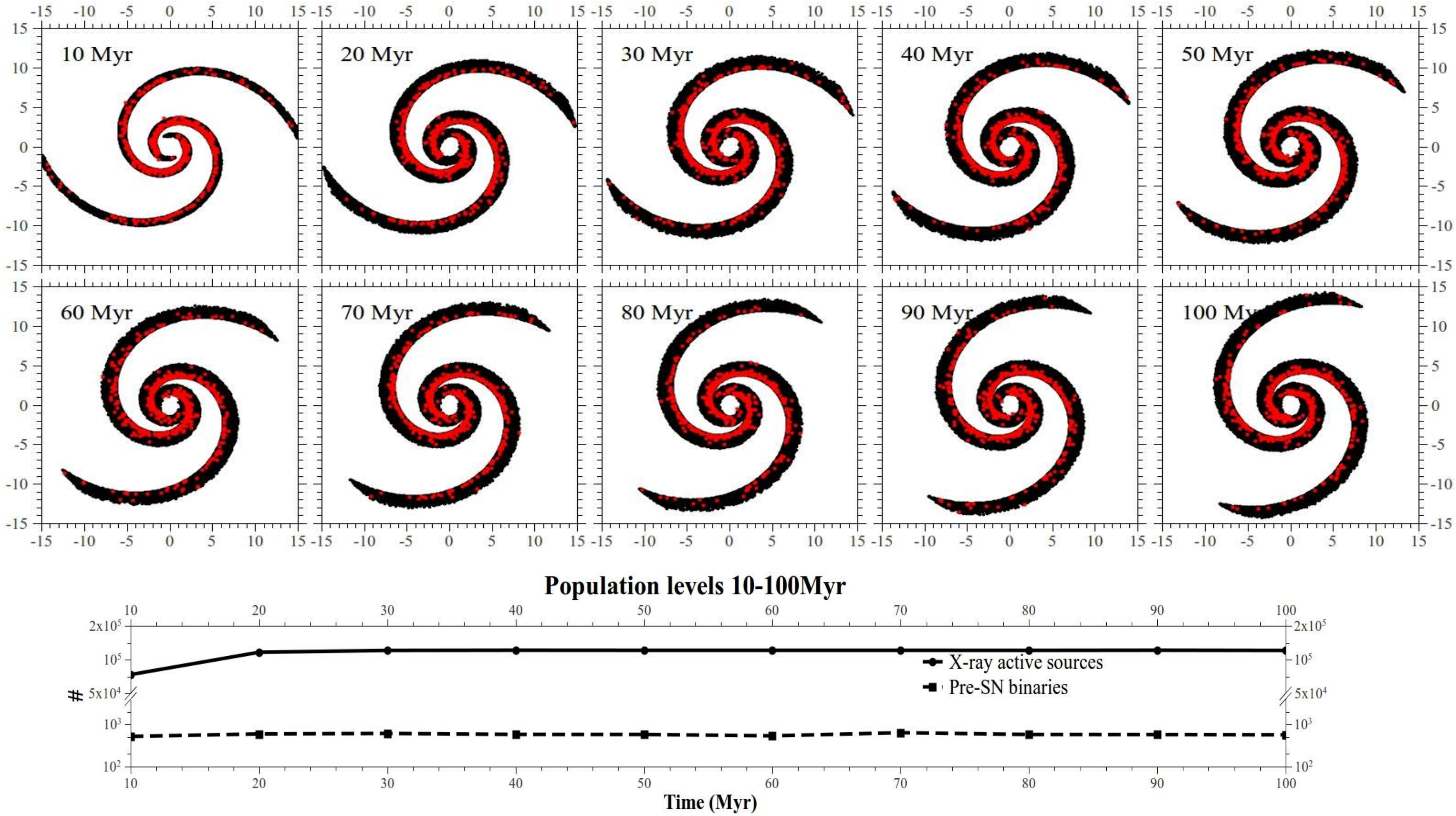

Figure 4.26: *HMXBs (red dots) plotted with the population of pre-SN systems (black dots) from the model with a pattern speed of 10kms*$^{-1}$*kpc*$^{-1}$ *at epochs from 10-100Myr.*

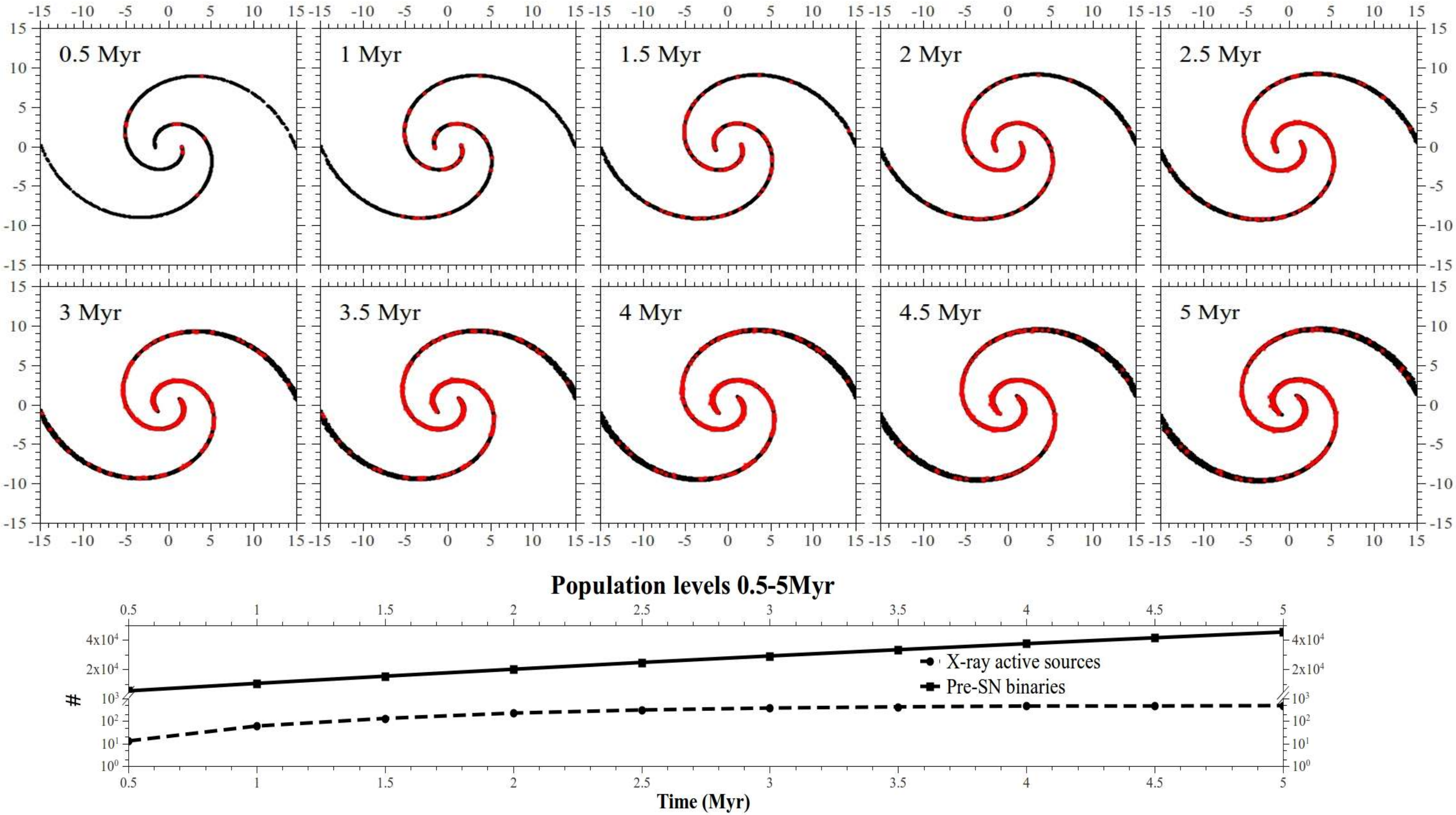

Figure 4.27: *HMXBs (red dots) plotted with the population of pre-SN systems (black dots) from the model with a pattern speed of* $50kms^{-1}kpc^{-1}$ *at epochs from 0.5-5Myr.*

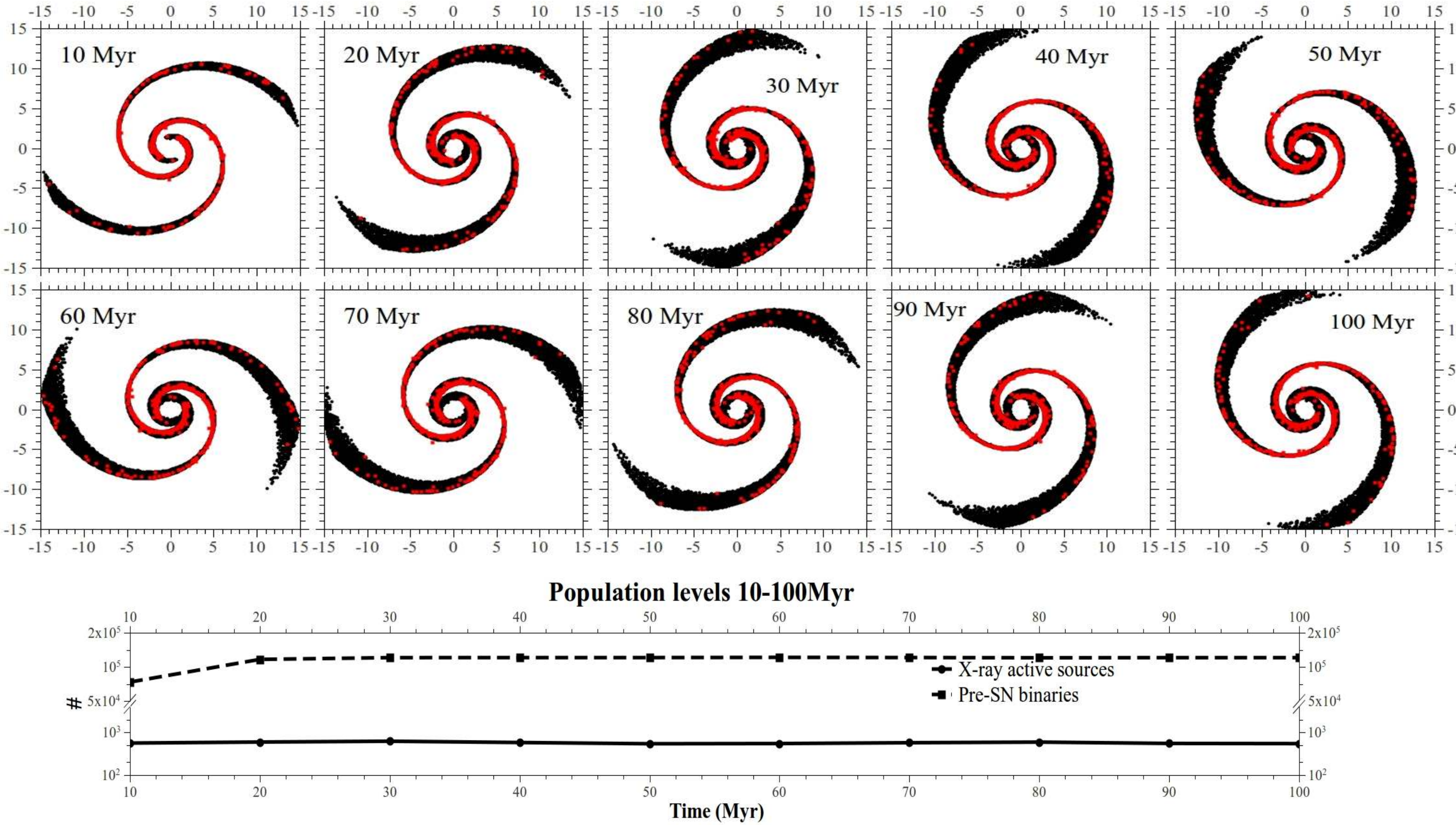

Figure 4.28: *HMXBs (red dots) plotted with the population of pre-SN systems (black dots) from the model with a pattern speed of $50kms^{-1}kpc^{-1}$ at epochs from 10-100Myr.*

To get a better sample of HMXB positions we use the same method as above to modulate the ϕ-positions to the same area in a polar coordinate system. As can be seen for the case of a low pattern speed (Figure 4.29) the thick spiral arms mean that HMXBs won't be able to travel to positions which are distinct from the population of pre-SN binaries. Although the HMXBs can be placed anywhere in the thick arms they are preferentially found in a thinner spiral than their pre-SN counterparts. In contrast to the latter, the HMXBs from the model with a pattern speed of 50kms^{-1}kpc^{-1} can be clearly seen as separate from the spiral arms around the co-rotation radius (Figure 4.30).

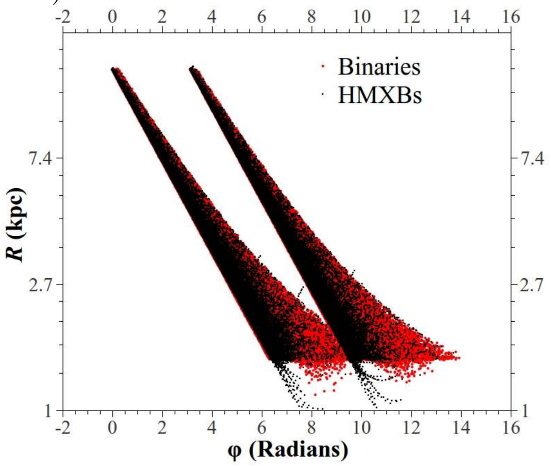

Figure 4.29: *Here we plot the increased sample of HMXB positions for the case of a spiral with a pattern of 10kms^{-1}kpc^{-1}. The thick arms which are due to the low pattern speed hide instances where the HMXB might have travelled away from the pre-SN population.*

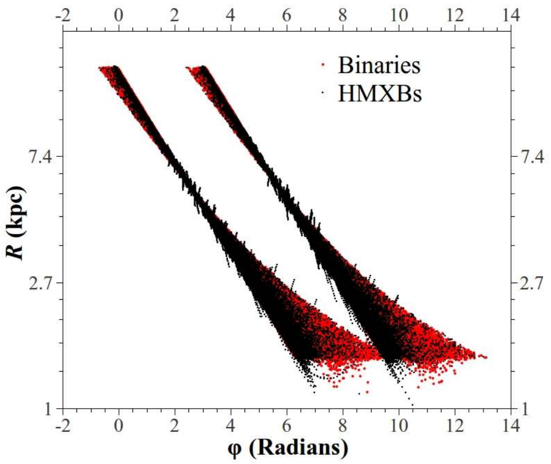

Figure 4.30: *Here we plot the increased sample of HMXB positions for the case of a spiral with a pattern of 10kms^{-1}kpc^{-1}. The high pattern speed causes the spiral arm to thin at the co-rotation radius (3.9kpc) allowing the HMXBs to travel away from the population of pre-Sn binaries.*

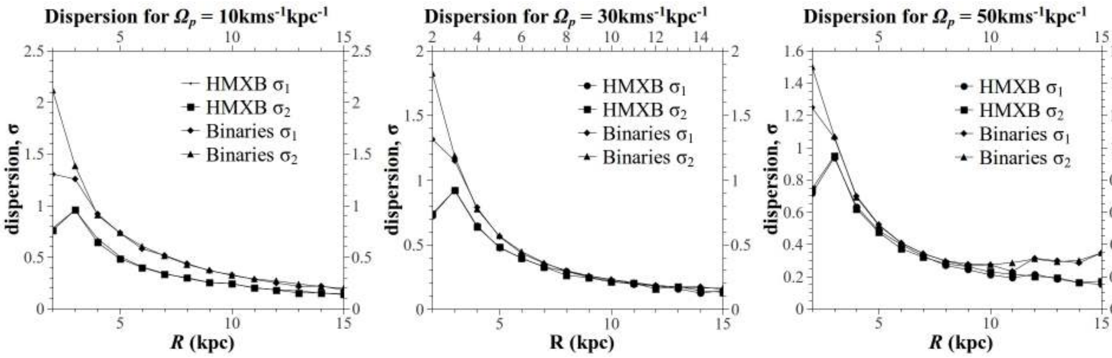

Figure 4.31: *The dispersions from Figures 4.21, B.2 and B.4 are gathered here and plotted as a function of radial distance.*

Again we quantitatively measure the dispersion in ϕ along the spiral arm for both cases. Following the same prescription as above we fit multi-peak Gaussian curves to the distributions in ϕ for distinct radial distance bins (see Figures B.6 and B.6 in Appendix B). We plot the dispersions as a function of R in Figure 4.31

4.5 Discussion

We have constructed a population synthesis program that populates a dynamical model in order to investigate the dispersions of HMXBs from the spiral arms where they originated. The population synthesis creates a sample of high mass binaries which conforms to observed distributions of stellar mass, mass ratios, semi-major axes and orbital eccentricities. We use the fitting functions of Eggleton et al., (1989) to evolve the binaries until one of the components explodes as a SN. We include the effects of mass transfer and tidal interactions in the pre-SN systems. We apply a distribution of kicks to the SN remnants and determine whether the system remains intact or is disrupted following the prescription of Hills (1983). The undisrupted systems, each containing a massive star and a compact object, are then assumed to emit X-rays due to a wind fed accretion onto the compact object. We use the binary birthrate of Iben and Tutukov (1995) to populate the dynamical model with binary systems that evolve according to the above prescription. The binaries are born along a spiral pattern with varying pitch angles and pattern speeds and initially orbit the galaxy centre in accordance with the potential defined in Section 3.3. The undisrupted post-SN binaries are then given a kick of 50kms^{-1} in a random 3D direction. We then measure the distribution of these X-ray emitters compared to the population of pre-SN binaries which we assume to adequately represent a population of young stars in a galaxy and consequently the distribution of Hα emission.

From the population synthesis model we find that the rate of disruption of massive binaries due a SN is strongly sensitive to the presence of of kick velocity which is imparted to the stellar remnant. The presence of even a modest kick can double the disruption rate in our model from ∼35% to ∼70% (disruption with no kick can also occur due to the escape of mass from the system). We find that the theoretical distributions of SN kick velocities (described in Section 4.2.2) can disrupt between 77% and 88% of high mass binaries (see Table 4.2 and Figure 4.6).

We find from the dynamical model that the population of HMXBs do not move appreciably far from the population of pre-SN binaries even though they have a high space velocity. In fact, we find that in all cases our HMXBs are tightly correlated to the spiral pattern from which they originate and are only seen distinctly apart from the pre-SN binaries in areas where the spiral arm is thin (Figures 4.17, 4.18, 4.19, 4.29 and 4.30). The thickness of the arms defined by the pre-SN binaries is a direct result of the nature of the spiral arms themselves. For low pitch angles we find that the spiral arms remain thin because the circular motion of the stars in the potential is similar to the almost circular (low α) spiral pattern (Figure 4.12). For this reason we suggest that HMXBs may be more readily found away from the spiral arms in galaxies with a low pitch angle. For galaxies with increasing pitch angle the circular motion of the stars is more and more at odds with the spiral pattern. This causes a thickening of the arms and although the HMXB distribution follows this thickening they are less likely to be found away from the light due to a young stellar population. The HMXBs tend to have a thinner distribution than the pre-SN binaries and are generally tightly correlated with the spiral pattern making them excellent tracers of recent star formation.

We also find that the pattern speed of the spiral has a noticeable effect on the dispersion of stars from the spiral. For a low pattern speed (and hence large co-rotation radius) we find that the dispersion creates very thick arms since the stars move much quicker than the spiral pattern and as a consequence the HMXBs are rarely placed away from the young stars in this case (Figure 4.29). Conversely, for a high pattern speed (and small co-rotation radius) we find that the high space velocity of the HMXBs enable them to travel away from the pre-SN binaries near the co-rotation radius, placing them in a position which would be distinct from the light of the young stellar population (Figure 4.30).

We also measure the dispersion of the pre-SN binaries and HMXBs in ϕ for each case as a function of galactocentric radius. We find that for low pitch angles the dispersion of pre-SN binaries and HMXBs is very similar but as the pitch angle is increased the pre-SN binaries become more dispersed than the HMXBs (Figure 4.22). In an opposite fashion we find that for small pattern speeds the dispersion of pre-SN binaries is greater than that of HMXBs and tends to equalise as the pattern speed is increased (Figure 4.31).

Observations of spiral galaxies have revealed many different populations of X-ray sources. These include the HMXBs, Low Mass X-ray binaries (LMXBs), SN remnants (SNRs) and also Active Galactic Nuclei (AGNs)[1]. These sources represent different populations with HMXBs, and the less luminous SNRs, representing a young population with lifetimes in the range 10^{6-7} yrs and should be concentrated towards the regions of recent star formation, namely the spiral arms of galaxies. The LMXBs represent an older population of stars with lifetime in the range 10^{8-9} yrs and should generally be distributed evenly around the disks of spirals although it has to be noted that they may trace out a spiral pattern if the arm/inter-arm stellar density ratio is high. The AGNs represent a population of background sources and have no connection with the spiral arms of a particular galaxy. The LMXBs may be separated from the HMXBs by their soft spectra although (rare) high mass black hole binaries have been suggested to have soft spectra also. For this reason colour-colour diagrams have been used to distinguish X-ray sources. HMXB sources also exhibit variability in their X-ray emission due to the intermittent nature of accretion on to the compact object and so a study of the temporal variation in X-ray luminosities can identify HMXBs. The LMXBs also have higher X-ray luminosities compared to HMXBs. In order to compare our model to observations of X-ray sources in spiral galaxies one would obviously have to use these methods to separate the different classes of sources.

XMM-Newton and Chandra have amassed many extragalactic X-ray sources and a study of their distributions will compliment the results of our model. Chandra's subarcsecond resolution can resolve discrete X-ray sources in galaxies out to a distance of the Virgo cluster and its photometric abilities allow it to distinguish between X-ray sources. In general the distributions would have to be corrected for host galaxy inclination and assumptions would have to be made about their vertical distribution in the galaxy. Shtykovskiy and Gilfanov (2007) have already used Chandra data to study the distributions of HMXBs in M51. However, their study reveals that HMXBs have a wider distribution than the observed distribution of Hα emission at odds with the results from our model[2]. We suggest that the major sources of disagreement

[1] Other low luminosity sources may include accreting white dwarfs and old SNRs

[2] Due to the low counts of X-ray sources their conclusion does not have a high statistical significance

between the studies is that our model does not include a radial velocity dispersion in the pre-SN binaries which could greatly increase dispersion of HMXBs from our model and that M51 does not display a perfectly logarithmic spiral (see Figure 4.1). Further work would include a radial velocity dispersion in the pre-SN binaries and would also investigate varying SFRs along the spiral arms.

Bibliography

Andredakis, Y. C., Peletier, R. F., and Balcells, M.: 1995, *MNRAS* **275**, 874

Arzoumanian, Z., Chernoff, D. F., and Cordes, J. M.: 2002, *ApJ* **568**, 289

Athanassoula, E., Garcia-Gomez, C., and Bosma, A.: 1993, *A&AS* **102**, 229

Baade, W.: 1944, *ApJ* **100**, 137

Belczyński, K. and Bulik, T.: 1999, *A&A* **346**, 91

Bethe, H. A. and Brown, G. E.: 1998, *ApJ* **506**, 780

Blaauw, A.: 1958, *Ricerche Astronomiche* **5**, 105

Blaauw, A.: 1961, *Bull. Astron. Inst. Netherlands* **15**, 265

Blaauw, A. and Ramachandran, R.: 1998, *Journal of Astrophysics and Astronomy* **19**, 19

Boissier, S. and Prantzos, N.: 2009, *A&A* **503**, 137

Bondi, H. and Hoyle, F.: 1944, *MNRAS* **104**, 273

Brown, G. E. and Bethe, H. A.: 1994, *ApJ* **423**, 659

Brown, W. R., Geller, M. J., Kenyon, S. J., and Kurtz, M. J.: 2005, *ApJ* **622**, L33

Burrows, A., Hayes, J., and Fryxell, B. A.: 1995, *ApJ* **450**, 830

Bush, S. J., Cox, T. J., Hayward, C. C., Thilker, D., Hernquist, L., and Besla, G.: 2010, *ApJ* **713**, 780

Butcher, J.: 2003, *Numerical methods for ordinary differential equations*, J. Wiley

de Grijs, R.: 1998, *MNRAS* **299**, 595

de Vaucouleurs, G.: 1948, *Annales d'Astrophysique* **11**, 247

de Wit, W. J., Testi, L., Palla, F., and Zinnecker, H.: 2005, *A&A* **437**, 247

Dehnen, W. and Binney, J.: 1998, *MNRAS* **294**, 429

della Valle, M. and Livio, M.: 1994, *ApJ* **423**, L31

Dray, L. M., Dale, J. E., Beer, M. E., Napiwotzki, R., and King, A. R.: 2005, *MNRAS* **364**, 59

Duquennoy, A. and Mayor, M.: 1991, *A&A* **248**, 485

Eggleton, P. P.: 1983, *ApJ* **268**, 368

Eggleton, P. P., Tout, C. A., and Fitchett, M. J.: 1989, *ApJ* **347**, 998

Fathi, K., Allen, M., Boch, T., Hatziminaoglou, E., and Peletier, R. F.: 2010, *MNRAS*

406, 1595
Fehlberg, E.: 1969, **4(2)**, 93
Flynn, C., Sommer-Larsen, J., and Christensen, P. R.: 1996, *MNRAS* **281**, 1027
Frail, D. A., Goss, W. M., and Whiteoak, J. B. Z.: 1994, *ApJ* **437**, 781
Freeman, K. C.: 1970, *ApJ* **160**, 811
Freudenreich, H. T.: 1998, *ApJ* **492**, 495
Giacconi, R. and Gursky, H. (eds.): 1974, *X-ray astronomy*, Vol. 43 of *Astrophysics and Space Science Library*
Gies, D. R.: 1987, *ApJS* **64**, 545
Gies, D. R. and Bolton, C. T.: 1986, *ApJS* **61**, 419
Graham, A. W. and Worley, C. C.: 2008, *MNRAS* **388**, 1708
Hakobyan, A. A., Mamon, G. A., Petrosian, A. R., Kunth, D., and Turatto, M.: 2009, *A&A* **508**, 1259
Hills, J. G.: 1983, *ApJ* **267**, 322
Hobbs, G., Lorimer, D. R., Lyne, A. G., and Kramer, M.: 2005, *MNRAS* **360**, 974
Hogeveen, S. J.: 1992, *Ap&SS* **194**, 143
Hoogerwerf, R., de Bruijne, J. H. J., and de Zeeuw, P. T.: 2001, *A&A* **365**, 49
Huang, Y.: 1987, *PASP* **99**, 461
Iben, Jr., I., Tutukov, A. V., and Yungelson, L. R.: 1995, *ApJS* **100**, 217
Irrgang, A., Przybilla, N., Heber, U., Nieva, M. F., and Schuh, S.: 2010, *ApJ* **711**, 138
Jurić, M., Ivezić, Ž., Brooks, A., Lupton, R. H., Schlegel, D., Finkbeiner, D., Padmanabhan, N., Bond, N., Sesar, B., Rockosi, C. M., Knapp, G. R., Gunn, J. E., Sumi, T., Schneider, D. P., Barentine, J. C., Brewington, H. J., Brinkmann, J., Fukugita, M., Harvanek, M., Kleinman, S. J., Krzesinski, J., Long, D., Neilsen, Jr., E. H., Nitta, A., Snedden, S. A., and York, D. G.: 2008, *ApJ* **673**, 864
Kaper, L., van Loon, J. T., Augusteijn, T., Goudfrooij, P., Patat, F., Waters, L. B. F. M., and Zijlstra, A. A.: 1997, *ApJ* **475**, L37+
Kazarian, M. A.: 1997, *Astrofizika* **40**, 296
Kennicutt, Jr., R. C.: 1983, *ApJ* **272**, 54
Kennicutt, Jr., R. C.: 1998, *ARA&A* **36**, 189
Knapen, J. H. and van der Kruit, P. C.: 1991, *A&A* **248**, 57
Kotake, K., Yamada, S., and Sato, K.: 2003, *ApJ* **595**, 304
Kregel, M., van der Kruit, P. C., and de Grijs, R.: 2002, *MNRAS* **334**, 646
Kusenko, A. and Segrè, G.: 1996, *Physical Review Letters* **77**, 4872
Lin, C. C. and Shu, F. H.: 1964, *ApJ* **140**, 646
Lipunov, V. M., Postnov, K. A., and Prokhorov, M. E.: 1997, *MNRAS* **288**, 245
Martin, J. C.: 2006, *AJ* **131**, 3047

Mason, B. D., Gies, D. R., Hartkopf, W. I., Bagnuolo, Jr., W. G., ten Brummelaar, T., and McAlister, H. A.: 1998, *AJ* **115**, 821

Massevitch, A. G., Popova, E. I., Tutukov, A. V., and Iungelson, L. R.: 1979, *Ap&SS* **62**, 451

McMillan, R. J. and Ciardullo, R.: 1996, *ApJ* **473**, 707

Meurs, E. J. A. and van den Heuvel, E. P. J.: 1989, *A&A* **226**, 88

Minkowski, R.: 1941, *PASP* **53**, 224

Miyamoto, M. and Nagai, R.: 1975, *PASJ* **27**, 533

Mosenkov, A. V., Sotnikova, N. Y., and Reshetnikov, V. P.: 2010, *MNRAS* **401**, 559

Mueller, M. W. and Arnett, W. D.: 1976, *ApJ* **210**, 670

O Maoileidigh, R.: 2009, *PhD Thesis*

Oemler, Jr., A. and Tinsley, B. M.: 1979, *AJ* **84**, 985

Ohta, K., Hamabe, M., and Wakamatsu, K.-I.: 1990, *ApJ* **357**, 71

Pols, O. R. and Marinus, M.: 1994, *A&A* **288**, 475

Portegies Zwart, S. F.: 2000, *ApJ* **544**, 437

Portegies Zwart, S. F. and Verbunt, F.: 1996, *A&A* **309**, 179

Poveda, A., Ruiz, J., and Allen, C.: 1967, *Boletin de los Observatorios Tonantzintla y Tacubaya* **4**, 86

Reid, M. J., Menten, K. M., Zheng, X. W., Brunthaler, A., Moscadelli, L., Xu, Y., Zhang, B., Sato, M., Honma, M., Hirota, T., Hachisuka, K., Choi, Y. K., Moellenbrock, G. A., and Bartkiewicz, A.: 2009, *ApJ* **700**, 137

Riess, A. G. and Macri, L.: 2007, in *Bulletin of the American Astronomical Society*, Vol. 38 of *Bulletin of the American Astronomical Society*, pp 826–+

Robin, A. C., Reylé, C., Derrière, S., and Picaud, S.: 2003, *A&A* **409**, 523

Sanders, R. H. and Huntley, J. M.: 1976, *ApJ* **209**, 53

Scheck, L., Plewa, T., Janka, H.-T., Kifonidis, K., and Müller, E.: 2004, *Physical Review Letters* **92(1)**, 011103

Schmidt, M.: 1959, *ApJ* **129**, 243

Sersic, J. L.: 1968, *Atlas de galaxias australes*

Shaw, R. L.: 1979, *A&A* **76**, 188

Shtykovskiy, P. E. and Gilfanov, M. R.: 2007, *Astronomy Letters* **33**, 299

Shu, F. H.: 1973, in J. M. Greenberg & H. C. van de Hulst (ed.), *Interstellar Dust and Related Topics*, Vol. 52 of *IAU Symposium*, p. 257

Spitzer, L.: 1978, *Physical processes in the interstellar medium*

Stone, R. C.: 1979, *ApJ* **232**, 520

Stone, R. C.: 1991, *AJ* **102**, 333

Tademaru, E. and Harrison, E. R.: 1975, *Nature* **254**, 676

Thielemann, F.-K., Brachwitz, F., Höflich, P., Martinez-Pinedo, G., and Nomoto, K.:

2004, **48**, 605

Toomre, A.: 1981, in S. M. Fall & D. Lynden-Bell (ed.), *Structure and Evolution of Normal Galaxies*, pp 111–136

Toomre, A. and Toomre, J.: 1972, *ApJ* **178**, 623

van den Heuvel, E. P. J. and Habets, G. M. H. J.: 1984, *Nature* **309**, 598

van den Heuvel, E. P. J., Portegies Zwart, S. F., Bhattacharya, D., and Kaper, L.: 2000, *A&A* **364**, 563

van der Kruit, P. C. and Searle, L.: 1981, *A&A* **95**, 105

Verley, S., Corbelli, E., Giovanardi, C., and Hunt, L. K.: 2009, *A&A* **493**, 453

Vrancken, M., De Greve, J. P., Yungelson, L., and Tutukov, A.: 1991, *A&A* **249**, 411

Waters, L. B. F. M. and van Kerkwijk, M. H.: 1989, *A&A* **223**, 196

Woosley, S. E. and Weaver, T. A.: 1986, *ARA&A* **24**, 205

Wyse, R. F. G., Gilmore, G., and Franx, M.: 1997, *ARA&A* **35**, 637

Yoachim, P. and Dalcanton, J. J.: 2006, *AJ* **131**, 226

Appendix A

Runaway Model

A.1 Derivation of R_i

As described in Section 3.2 above we obtain the radial distribution by defining a function which is the difference of two exponential functions. This gives us a distribution which has a central hole but beyond this, the distribution is exponentially decaying, the rate of which is defined by the scalelength, h_r. The radial distribution function is

$$A_0 \left[\exp\left(\frac{-r}{h_r}\right) - C \exp\left(k[(\frac{r}{r_e})^{\frac{1}{4}} - 1]\right)\right] \tag{A.1.1}$$

which is an exponential profile minus a Sérsic profile. Here A_0 is a constant which keeps the area under the curve of the above equation equal to one when it is integrated from 0 to R_{max} (which is set at 15kpc). We introduce a constant C which, at $r = 0$, sets the Sérsic part of the equation equal to the exponential part of the equation. This means that no test particle will have $R = 0kpc$. k is a constant which can be evaluated numerically by noting that r_e, the effective radius which contains half the total light, must satisfy the following equality

$$2 \int_0^{r_e} C \exp\left(k[(\frac{r}{r_e})^{\frac{1}{4}} - 1]\right) \partial r = \int_0^{\infty} C \exp\left(k[(\frac{r}{r_e})^{\frac{1}{4}} - 1]\right) \partial r \tag{A.1.2}$$

Using Equation 3.2.2 it is now possible to express the Sérsic part of Equation A.1.1 as an exponential with scalelength h_b such that

$$\begin{aligned} I(r) &= I_0 \exp\left[\left(\frac{-r}{h_b}\right)^{\frac{1}{n}}\right] \\ &= I_e \exp\left[k\left\{\left(\frac{r}{r_e}\right)^{\frac{1}{n}} - 1\right\}\right] \end{aligned} \tag{A.1.3}$$

The total distribution function can now be written as the difference of two exponentials, greatly simplifying the derivation of radial distances.

$$I = I_0\left[\exp\left(\frac{-r}{h_r}\right) - \exp\left(\frac{-r}{h_b}\right)^{\frac{1}{n}}\right] \tag{A.1.4}$$

We then set each of the elements of set B_R equal to the area under the curve of equation A.1.4 integrated from 0 to R_i, the test particles radial distance.

$$B_{Ri} = \int_0^{R_i} A_0\left[\exp(\frac{-r}{h_r}) - C\exp(\frac{-r}{h_b})^{\frac{1}{n}}\right]\partial r \tag{A.1.5}$$

This gives, taking n =1;

$$B_{Ri} = A_0\left\{h_r - h_r\exp(\frac{-R_i}{h_r}) + h_b\exp(\frac{-R_i}{h_b}) - h_b\right\} \tag{A.1.6}$$

It is clear from the above equation that there is no analytical solution for R_i. We now employ Newtons method to solve Equation A.1.5 for the radial distance of each test particle. The method can be applied using the following equation where $f(R_i)$ is a function defining the behaviour of R_i and is just Equation A.1.5 rearranged to equal zero.

$$\begin{aligned} f(R_n) &= 0 \\ f'(R_n) &= \frac{\partial f(R_n)}{\partial R} \\ R_{n+1} &= R_n - \frac{f(R_n)}{f'(R_n)} \end{aligned} \tag{A.1.7}$$

At each iteration of the above equation R_{n+1} gets ever closer to the real value of R_i. Of course some initial guess must be inserted for the initial iteration and this can be extracted from the element B_{Ri} - if for example $B_{Ri} = 0.5$ then a rough value can be taken from a quick glance at a plot of the curve, in practice we assign an initial R for B_{Ri} values in distinct bins - Figure 3.1. We performed with this method over 50 iterations and extract a reasonable distribution (Figure 3.1) but note that if the function $f(R)$ traces out multiple peaks this method becomes inefficient. For the above method we set

$$f(R_1) = A_0 \left\{ h_r - h_r \exp(\frac{-R_1}{h_r}) + h_b \exp(\frac{-R_1}{h_b}) - h_b \right\} - B_{Ri} \tag{A.1.8}$$

and $f'(R_1)$ is simply

$$f'(R_1) = A_0 \left[\exp(\frac{-R_1}{h_r}) - C \exp(\frac{-R_1}{h_b})^{\frac{1}{n}} \right] \tag{A.1.9}$$

A_0 can be evaluated by setting B_{Ri} in Equation A.1.5 equal to one and integrating from 0 to R_{max}. This gives

$$A_0 = \left\{ h_r - h_b - h_r \exp\left(\frac{-R_{max}}{h_r}\right) + h_b \exp\left(\frac{-R_{max}}{h_b}\right) \right\}^{-1} \tag{A.1.10}$$

Using the parameters h_r =3.37, h_b =0.538 and R_{max} =15 A_0 is calculated as 0.3581.

A.2 Derivation of z_i

The distribution of the heights of the test particles above/below the galaxy disk is based on a function of the form

$$A_z \text{sech}^2\left(\frac{z}{h_z}\right) \tag{A.2.1}$$

where A_z is again a number that sets the area under the above curve equal to 1 when integrated from z_{min} to z_{max} (where $z_{min} = -z_{max}$). It is useful to express A_z as a function of h_z and z_{max}. A_z is found by setting

$$\begin{aligned} 1 &= \int_{z_{min}}^{z_{max}} A_z \text{sech}^2\left(\frac{z}{h_z}\right) dz \\ &= \left[A_z h_z \tanh\left(\frac{z}{h_z}\right) \right]_{-z_{max}}^{z_{max}} \\ &= A_z \left[h_z \tanh\left(\frac{z_{max}}{h_z}\right) - h_z \tanh\left(\frac{-z_{max}}{h_z}\right) \right] \\ &= A_z \left[2h_z \tanh\left(\frac{z_{max}}{h_z}\right) \right] \end{aligned} \tag{A.2.2}$$

giving

$$A_z = \left[2h_z \tanh\left(\frac{z_{max}}{h_z}\right) \right]^{-1}$$

In the same manner as for the derivation of R_i, the elements of set B_z are set equal to the area under the curve of Equation A.2.1 integrated from $-z_{max}$ to z_i such that

$$B_{zi} = \int_{-z_{max}}^{z_i} A_z \mathrm{sech}^2\left(\frac{z}{h_z}\right) \partial z \tag{A.2.3}$$

This gives

$$\begin{aligned} B_{zi} &= \left[A_z h_z \tanh\left(\frac{z}{h_z}\right)\right]_{-z_{max}}^{z_i} \\ &= A_z \left[h_z \tanh\left(\frac{z_i}{h_z}\right) + h_z \tanh\left(\frac{z_{max}}{h_z}\right)\right] \\ \frac{B_{zi}}{A_z} &= 2B_z h_z \tanh\left(\frac{z_{max}}{h_z}\right) \\ &= h_z \left[\tanh\left(\frac{z_i}{h_z}\right) + \tanh\left(\frac{z_{max}}{h_z}\right)\right] \end{aligned} \tag{A.2.4}$$

so that

$$2B_z \tanh\left(\frac{z_{max}}{h_z}\right) - \tanh\left(\frac{z_{max}}{h_z}\right) = \tanh\left(\frac{z_i}{h_z}\right)$$

Where we have used the relation $\tanh(-x) = -\tanh(x)$. Now we use the relation

$$\tanh^{-1}(x) = \frac{1}{2} \ln\left[\frac{1+x}{1-x}\right] \tag{A.2.5}$$

to solve for z_i such that

$$z_i = \frac{h_z}{2} \ln\left[\frac{1 + \tanh\left(\frac{z_{max}}{h_z}\right)(2B_z - 1)}{1 - \tanh\left(\frac{z_{max}}{h_z}\right)(2B_z - 1)}\right] \tag{A.2.6}$$

A.3 Derivation of M_i

The masses of the test particles is determined randomly by the following equation:

$$B_{Mi} = A_M \int_{M_{min}}^{M_i} M^{\alpha} \, \partial M \tag{A.3.1}$$

where, as above, A_M is a constant which sets the above equation equal to one when integrated from the minimum, M_{min}, to maximum, M_{max}, allowable masses, 10 and

$100M_\odot$ respectively such that

$$
\begin{aligned}
1 &= A_M \int_{M_{min}}^{M_{max}} M^\alpha \, \partial M \\
&= A_M \left[\frac{M^{(\alpha+1)}}{\alpha+1} \right]_{M_{min}}^{M_{max}} \\
A_M &= \left[\frac{M_{max}^{(\alpha+1)}}{\alpha+1} - \frac{M_{min}^{(\alpha+1)}}{\alpha+1} \right]^{-1}
\end{aligned}
\tag{A.3.2}
$$

Equation A.3.1 is now integrated to find the stellar mass associated with the random number B_{Mi}:

$$
\begin{aligned}
B_{Mi} &= A_M \left[\frac{M^{(\alpha+1)}}{\alpha+1} \right]_{M_{min}}^{M_i} \\
\frac{B_{Mi}}{A_M} &= \frac{M_i^{(\alpha+1)}}{\alpha+1} - \frac{M_{min}^{(\alpha+1)}}{\alpha+1}
\end{aligned}
\tag{A.3.3}
$$

giving for the stellar masses

$$
M_i = \left\{ (\alpha+1) \left[\frac{B_{Mi}}{A_M} + \frac{M_{min}^{(\alpha+1)}}{\alpha+1} \right] \right\}^{\frac{1}{\alpha+1}}
$$

Using the previous equation for A_M the above expression for M_i can be simplified as

$$
M_i = \left\{ (\alpha+1) \left[B_{Mi} \left(\frac{M_{max}^{(\alpha+1)}}{\alpha+1} - \frac{M_{min}^{(\alpha+1)}}{\alpha+1} \right) + \frac{M_{min}^{(\alpha+1)}}{\alpha+1} \right] \right\}^{\frac{1}{\alpha+1}}
\tag{A.3.4}
$$

so that

$$
M_i = \left\{ B_{Mi} \left[M_{max}^{(\alpha+1)} - M_{min}^{(\alpha+1)} \right] + M_{min}^{(\alpha+1)} \right\}^{\frac{1}{\alpha+1}}
$$

A.4 Derivation of Terms from Galactic Potential

Here we will derive the terms which describe the rotation curve due to the galactic potential and also the forces exerted on each of the test particles during the simulation. In cylindrical coordinates (R,ϕ,z) the galactic potential (per unit mass) is defined by Flynn et al., (1996) as

$$
\Phi(R,z) = \frac{1}{2} V_H^2 \ln(r^2 + r_0^2) + \sum_{i=1}^{2} \frac{-GM_{Ci}}{\sqrt{r^2 + r_{Ci}^2}} + \sum_{i=1}^{3} \frac{-GM_{Di}}{\sqrt{R^2 + A_{Di}^2}}
\tag{A.4.1}
$$

with

$$A_{Di} = [a_i + \sqrt{(z^2 + b^2)}]$$

where r is the galactocentric distance ($r^2 = (R^2 + z^2)$), V_H is the rotation speed at a $r >> r_0$ (r_0 the core radius of the spherical dark halo), M_{C1} is the mass of the bulge with core radius r_{C1}, M_{C2} is the mass of the central compact object with core radius r_{C2}. M_{Di} are the masses of each of the disk components ($i = 1, 2, 3$) which have parameters a_i that are related to the scalelengths while the parameter b is related to the scaleheight (which is the same for each of the disk components).

A.4.1 The Acceleration Due to Gravity

Since equation A.4.1 describes the potential per unit mass the acceleration, a, of a particle within that potential is

$$\begin{aligned} a &= -\nabla\Phi(R,z) \\ &= -\left[\frac{\partial}{\partial R}[\Phi(R,z)]\hat{R} + \frac{1}{R}\frac{\partial}{\partial\phi}[\Phi(R,z)]\hat{\phi} + \frac{\partial}{\partial z}[\Phi(R,z)]\hat{z}\right] \end{aligned} \tag{A.4.2}$$

which, with no ϕ dependence, gives

$$a = -\left[\frac{\partial}{\partial R}[\Phi(R,z)]\hat{R} + \frac{\partial}{\partial z}[\Phi(R,z)]\hat{z}\right] \tag{A.4.3}$$

The acceleration in the $\hat{R}$-direction, a_R, is

$$\begin{aligned} a_R &= -\frac{\partial}{\partial R}\left[\frac{1}{2}V_H^2\ln(r^2 + r_0^2) + \sum_{i=1}^{2}\frac{-GM_{Ci}}{\sqrt{r^2 + r_{Ci}^2}} + \sum_{i=1}^{3}\frac{-GM_{Di}}{\sqrt{R^2 + A_{Di}^2}}\right] \\ &= -\left[\frac{V_H^2 R}{(r^2 + r_0^2)} + \sum_{i=1}^{2}\frac{GM_{Ci}R}{(r^2 + r_{Ci}^2)^{\frac{3}{2}}} + \sum_{i=1}^{3}\frac{GM_{Di}R}{(R^2 + A_{Di}^2)^{\frac{3}{2}}}\right] \end{aligned} \tag{A.4.4}$$

and the acceleration in the $\hat{z}$-direction, a_z, is

$$a_z = -\left[\frac{V_H^2 z}{(r^2 + r_0^2)} + \sum_{i=1}^{2}\frac{GM_{Ci}z}{(r^2 + r_{Ci}^2)^{\frac{3}{2}}} + \sum_{i=1}^{3}\frac{GM_{Di}A_{Di}z}{(R^2 + A_{Di}^2)^{\frac{3}{2}}(z^2 + b^2)^{\frac{1}{2}}}\right] \tag{A.4.5}$$

A.4.2 The Rotation Curve

To derive the rotation curve due to the potential A.4.1 we first note that the force per unit mass, F, on a particle in this potential is given by

$$F = -\nabla\Phi(R, z) \tag{A.4.6}$$

The acceleration in the $\hat{R}$-direction, a_R, is then

$$a_R = -\frac{\partial\Phi(R, z)}{\partial R} \tag{A.4.7}$$

which is also given by

$$a_R = \ddot{R} - R\dot{\phi}^2 \tag{A.4.8}$$

Since we want to find the circular speed of a particle in the plane of this potential we let $\ddot{R} = 0$, $z = 0$ and work out $\dot{\phi}$ from the equation

$$R\dot{\phi}^2 = \nabla\Phi(R) \tag{A.4.9}$$

giving,

$$\dot{\phi} = \sqrt{\frac{\nabla\Phi(R)}{R}} \tag{A.4.10}$$

which is just

$$\dot{\phi} = \sqrt{\frac{-a_R}{R}} = \left[\frac{V_H^2}{(r^2 + r_0^2)} + \sum_{i=1}^{2} \frac{GM_{Ci}}{(r^2 + r_{Ci}^2)^{\frac{3}{2}}} + \sum_{i=1}^{3} \frac{GM_{Di}}{(R^2 + A_{Di}^2)^{\frac{3}{2}}}\right]^{1/2} \tag{A.4.11}$$

Appendix B

HMXB Model

B.1 Dispersions from the spiral arm

Below we plot the dispersions in ϕ of HMXBs and pre-SN binaries in distinct radial distance bins with multi-peak Gaussian curves as defined by the prescription in Section 4.4.

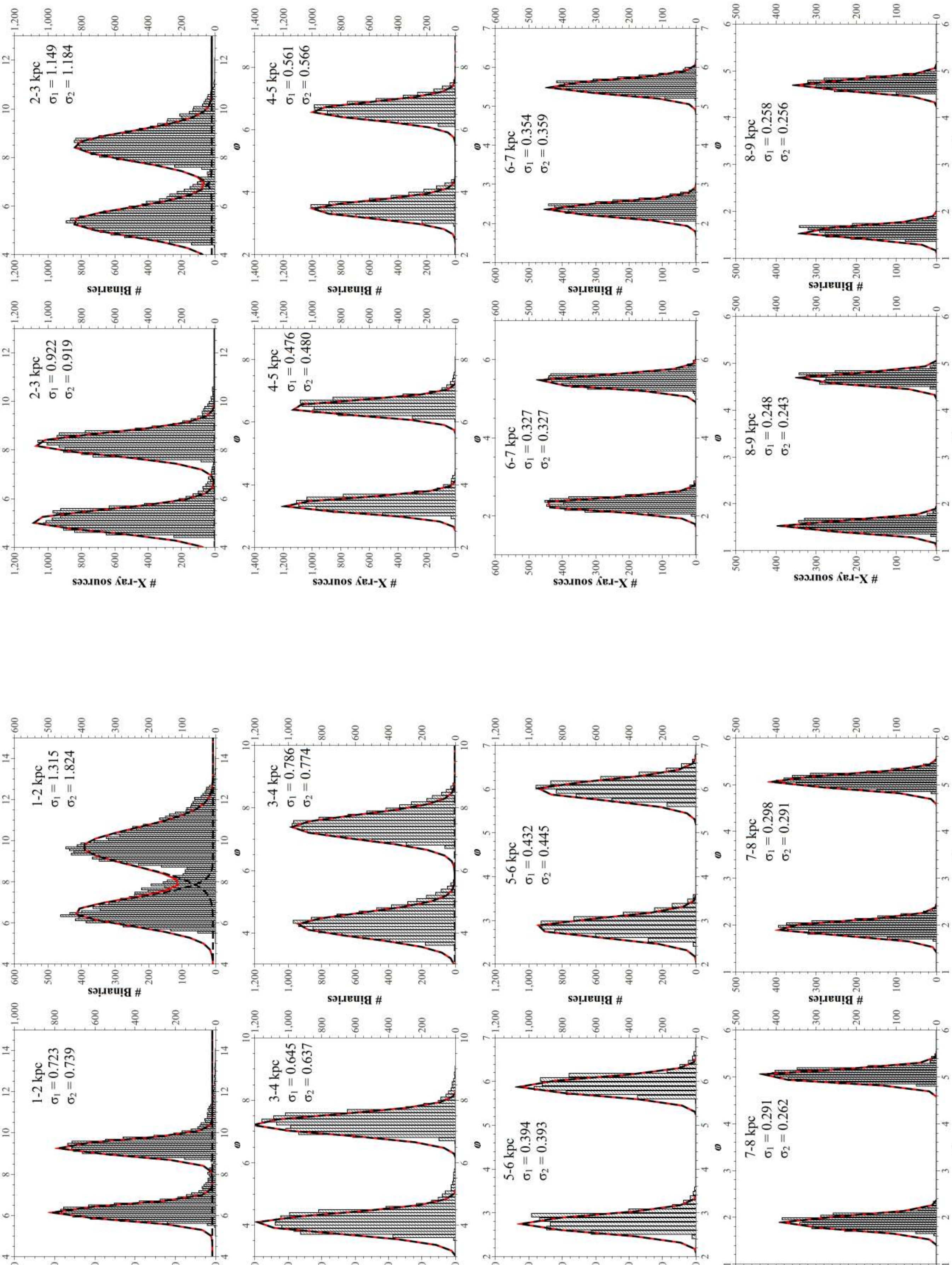

1-2 kpc
σ1 = 0.723
σ2 = 0.739
1-2 kpc
σ1 = 1.315
σ2 = 1.824
2-3 kpc
σ1 = 0.922
σ2 = 0.919
2-3 kpc
σ1 = 1.149
σ2 = 1.184
3-4 kpc
σ1 = 0.645
σ2 = 0.637
3-4 kpc
σ1 = 0.786
σ2 = 0.774
4-5 kpc
σ1 = 0.476
σ2 = 0.480
4-5 kpc
σ1 = 0.561
σ2 = 0.566
5-6 kpc
σ1 = 0.394
σ2 = 0.393
5-6 kpc
σ1 = 0.432
σ2 = 0.445
6-7 kpc
σ1 = 0.327
σ2 = 0.327
6-7 kpc
σ1 = 0.354
σ2 = 0.359
7-8 kpc
σ1 = 0.291
σ2 = 0.262
7-8 kpc
σ1 = 0.298
σ2 = 0.291
8-9 kpc
σ1 = 0.248
σ2 = 0.243
8-9 kpc
σ1 = 0.258
σ2 = 0.256
X-ray sources
Binaries
φ

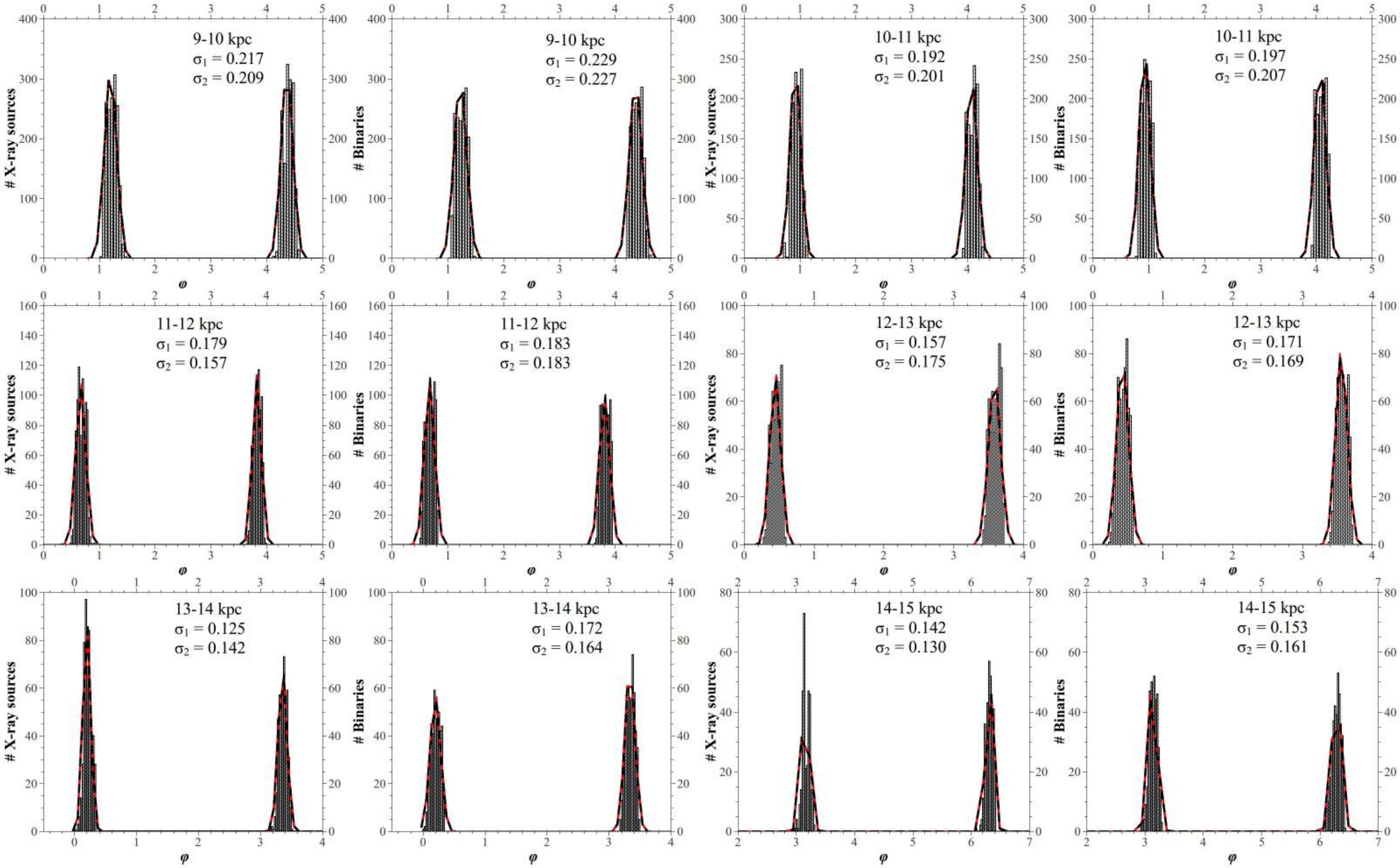

Figure B.2: *Dispersions for a pitch angle of 20° and a pattern speed of* $30kms^{-1}kpc^{-1}$.

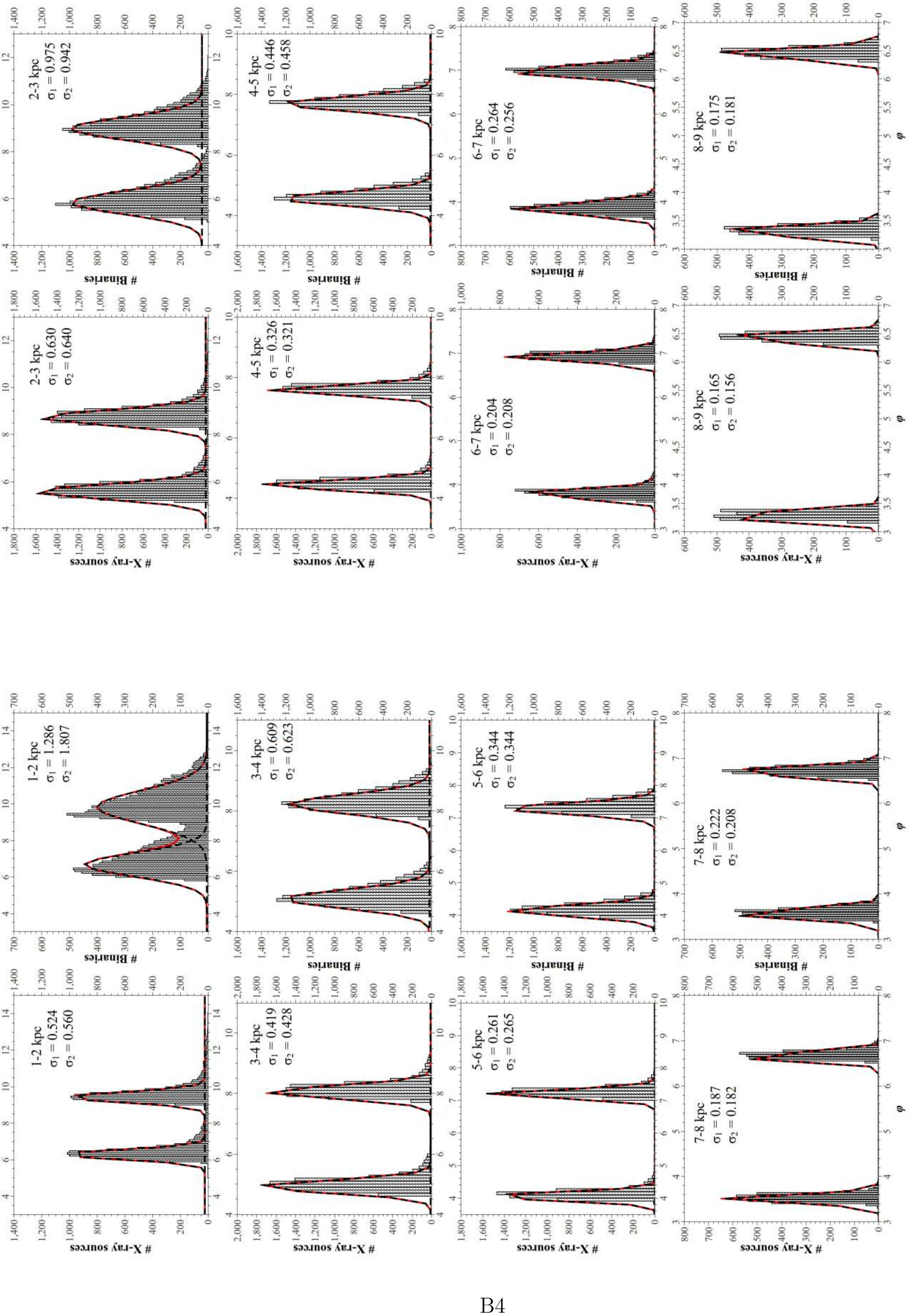

1-2 kpc
σ1 = 0.524
σ2 = 0.560
1-2 kpc
σ1 = 1.286
σ2 = 1.807
2-3 kpc
σ1 = 0.630
σ2 = 0.640
2-3 kpc
σ1 = 0.975
σ2 = 0.942
3-4 kpc
σ1 = 0.419
σ2 = 0.428
3-4 kpc
σ1 = 0.609
σ2 = 0.623
4-5 kpc
σ1 = 0.326
σ2 = 0.321
4-5 kpc
σ1 = 0.446
σ2 = 0.458
5-6 kpc
σ1 = 0.261
σ2 = 0.265
5-6 kpc
σ1 = 0.344
σ2 = 0.344
6-7 kpc
σ1 = 0.204
σ2 = 0.208
6-7 kpc
σ1 = 0.264
σ2 = 0.256
7-8 kpc
σ1 = 0.187
σ2 = 0.182
7-8 kpc
σ1 = 0.222
σ2 = 0.208
8-9 kpc
σ1 = 0.165
σ2 = 0.156
8-9 kpc
σ1 = 0.175
σ2 = 0.181
X-ray sources
Binaries
φ

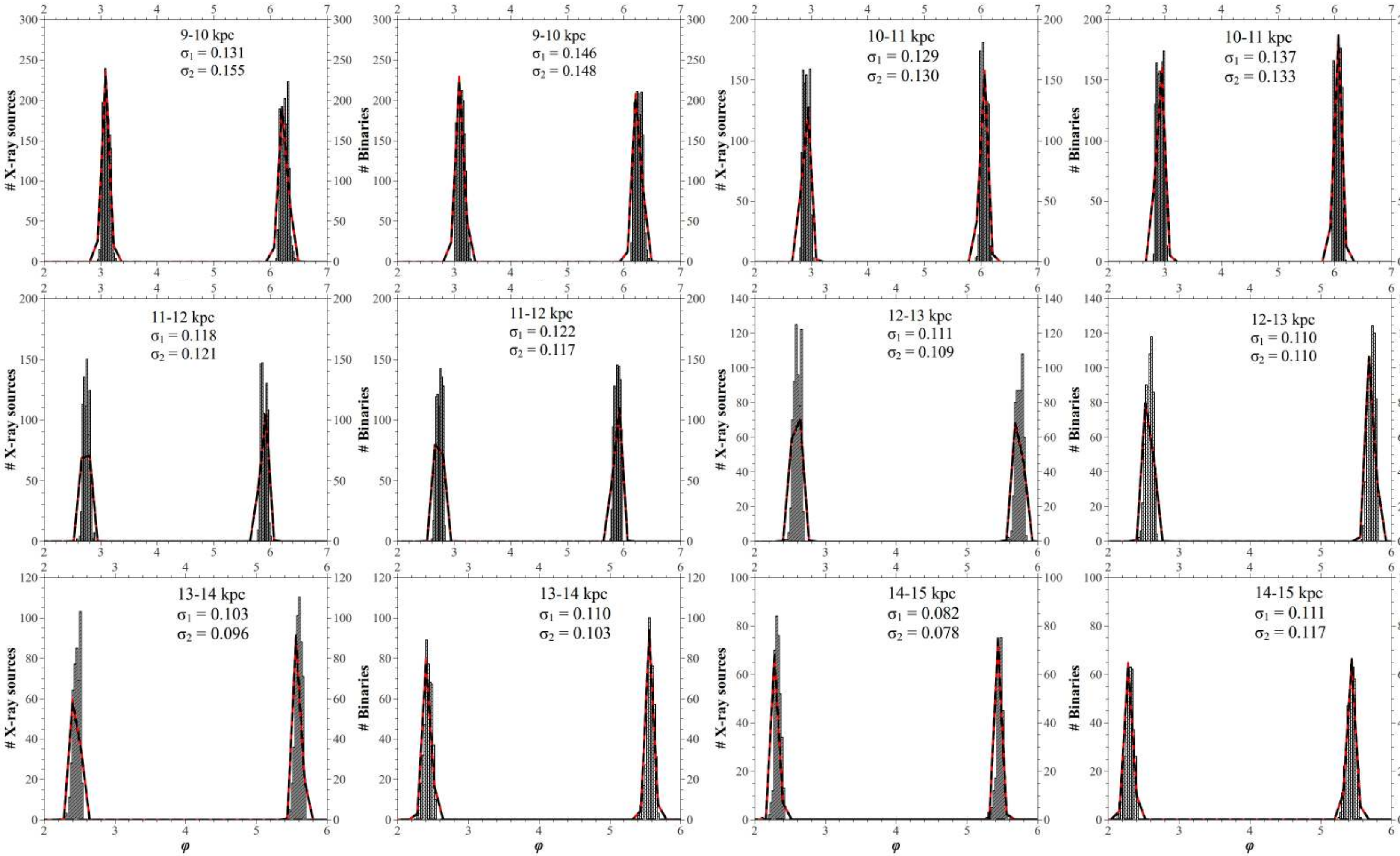

Figure B.4: *Dispersions for a pitch angle of 30° and a pattern speed of $30kms^{-1}kpc^{-1}$.*

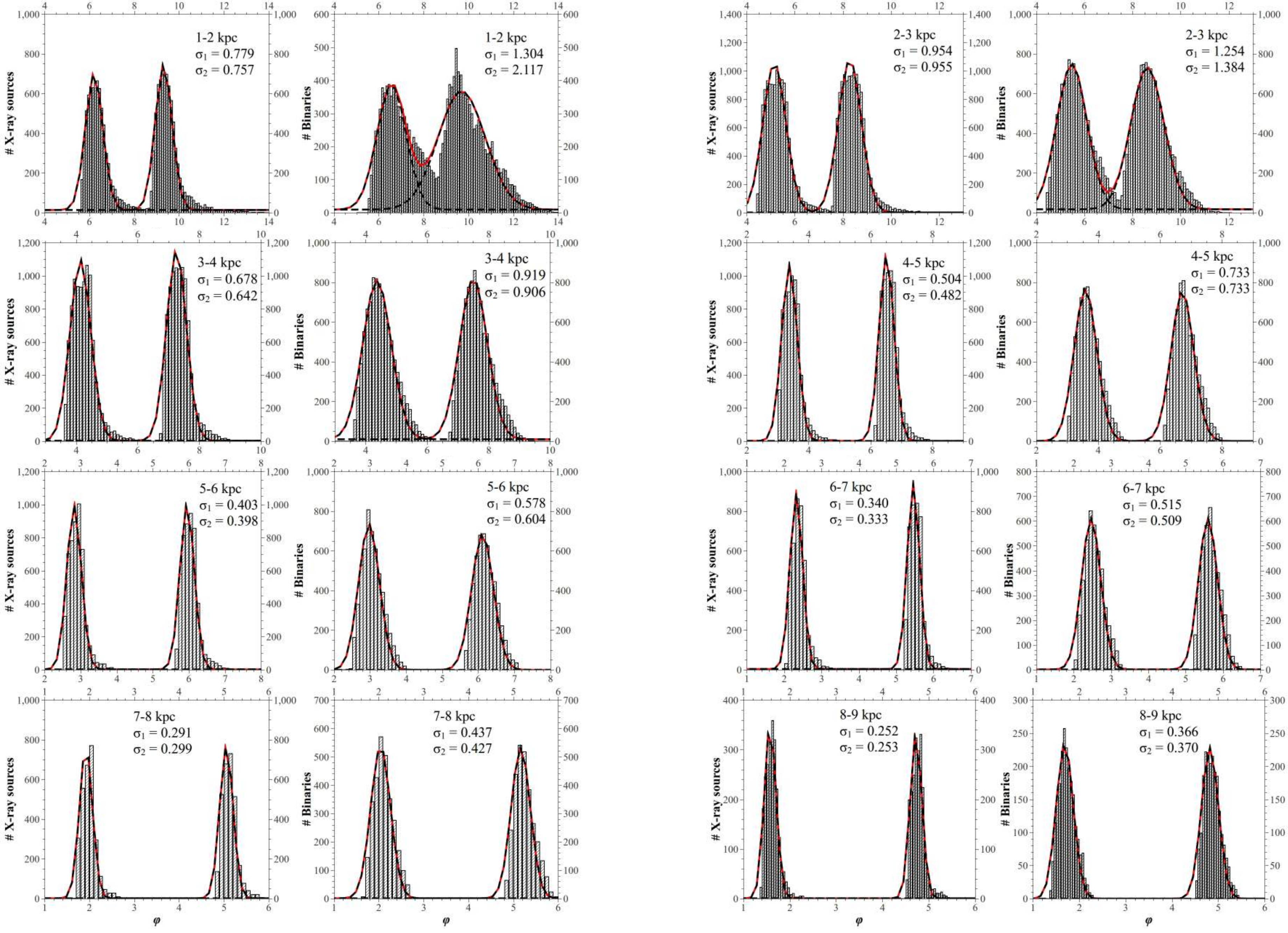
1-2 kpc
σ1 = 0.779
σ2 = 0.757
1-2 kpc
σ1 = 1.304
σ2 = 2.117
2-3 kpc
σ1 = 0.954
σ2 = 0.955
2-3 kpc
σ1 = 1.254
σ2 = 1.384
3-4 kpc
σ1 = 0.678
σ2 = 0.642
3-4 kpc
σ1 = 0.919
σ2 = 0.906
4-5 kpc
σ1 = 0.504
σ2 = 0.482
4-5 kpc
σ1 = 0.733
σ2 = 0.733
5-6 kpc
σ1 = 0.403
σ2 = 0.398
5-6 kpc
σ1 = 0.578
σ2 = 0.604
6-7 kpc
σ1 = 0.340
σ2 = 0.333
6-7 kpc
σ1 = 0.515
σ2 = 0.509
7-8 kpc
σ1 = 0.291
σ2 = 0.299
7-8 kpc
σ1 = 0.437
σ2 = 0.427
8-9 kpc
σ1 = 0.252
σ2 = 0.253
8-9 kpc
σ1 = 0.366
σ2 = 0.370
X-ray sources
Binaries
φ

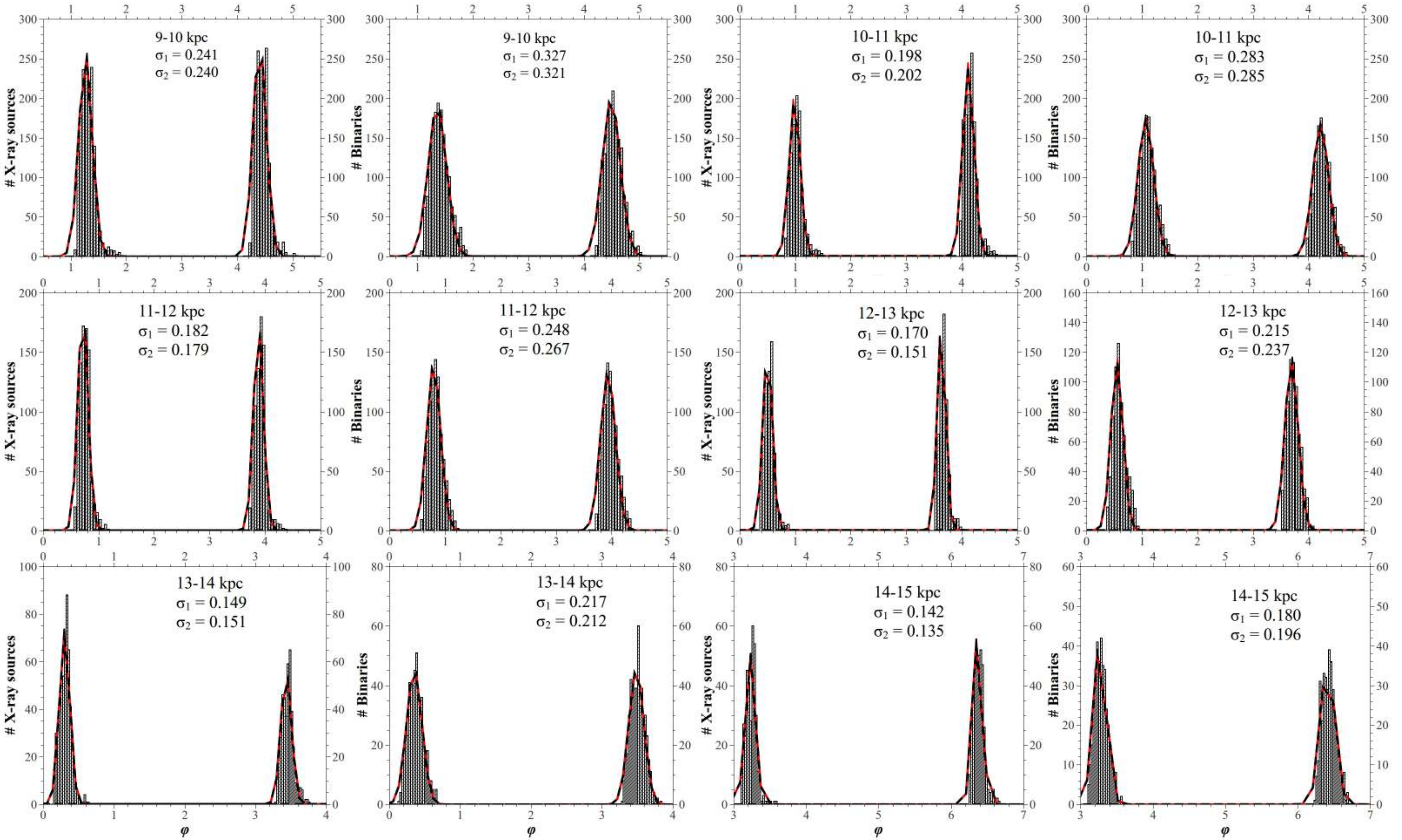

Figure B.6: *Dispersions for a pitch angle of 20° and a pattern speed of 10kms^{-1}kpc^{-1}.*

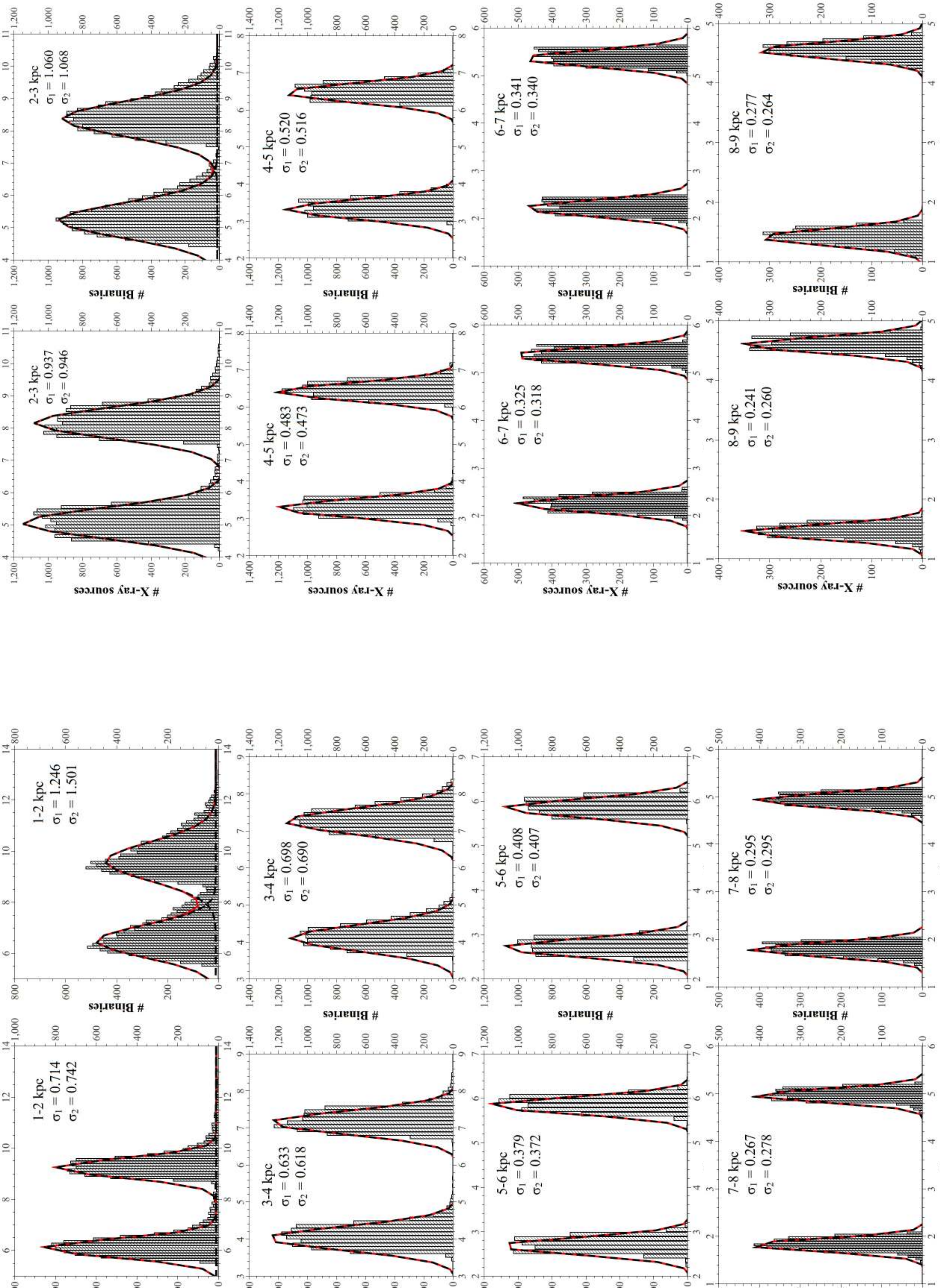

1-2 kpc
σ1 = 0.714
σ2 = 0.742
1-2 kpc
σ1 = 1.246
σ2 = 1.501
2-3 kpc
σ1 = 0.937
σ2 = 0.946
2-3 kpc
σ1 = 1.060
σ2 = 1.068
3-4 kpc
σ1 = 0.633
σ2 = 0.618
3-4 kpc
σ1 = 0.698
σ2 = 0.690
4-5 kpc
σ1 = 0.483
σ2 = 0.473
4-5 kpc
σ1 = 0.520
σ2 = 0.516
5-6 kpc
σ1 = 0.379
σ2 = 0.372
5-6 kpc
σ1 = 0.408
σ2 = 0.407
6-7 kpc
σ1 = 0.325
σ2 = 0.318
6-7 kpc
σ1 = 0.341
σ2 = 0.340
7-8 kpc
σ1 = 0.267
σ2 = 0.278
7-8 kpc
σ1 = 0.295
σ2 = 0.295
8-9 kpc
σ1 = 0.241
σ2 = 0.260
8-9 kpc
σ1 = 0.277
σ2 = 0.264
X-ray sources
Binaries
φ

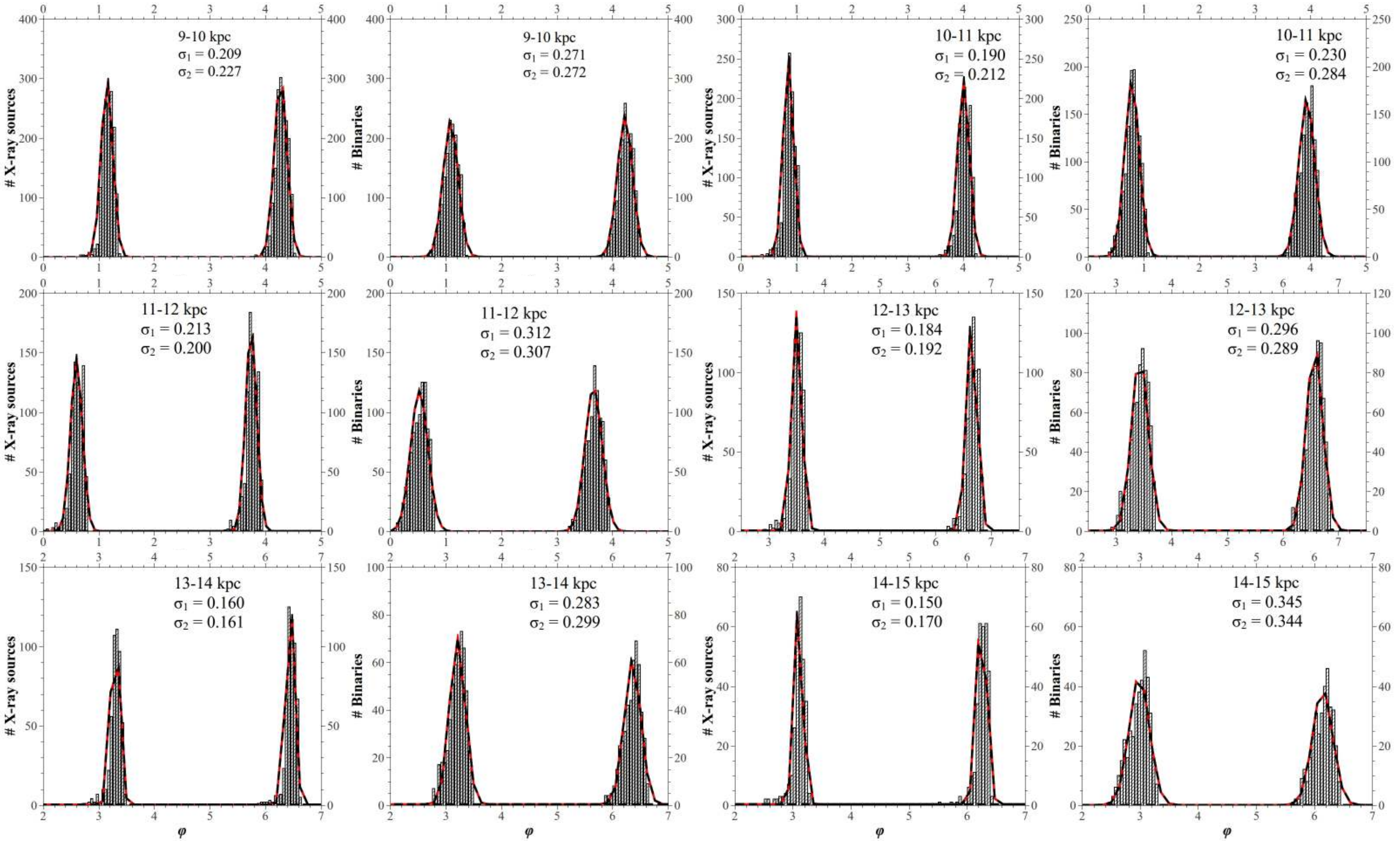

Figure B.8: *Dispersions for a pitch angle of 20° and a pattern speed of* $50kms^{-1}kpc^{-1}$.

Appendix C

SN Sample

In the following tables we list the SNae used for the study in this thesis. We also include some details about the host galaxy of each SN and also some derived properties.

Table C.1: *Here we list the sample of SN for the "edge-on" study. The first and second column list the SN designation and also its type, determined by a spectral and photometric analysis. The third, fourth, fifth and sixth columns describe some properties of the host galaxy - the host galaxy designation, the galaxy type, its redshift and the inclination of the galaxy respectively. The seventh, eighth and ninth columns describe some derived properties - the height of the SN above the disk of the host galaxy, the distance along the disk and the normalised distance along the disk. See Section 2.2 for a full description of these parameters.*

SN Name	SN Type	Host Galaxy	Galaxy Type	Redshift (z)	Inclination (i°)	z_{SN} (kpc)	R_{SN} (kpc)	R_N ($\frac{R_{SN}}{R_{Gal}}$)
1989C	II P	M+01-25-25	SBcd	0.0063	90	0.20	0.04	0.00
2005dn	II	NGC6861F	SBdm?	0.0107	80	1.17	0.04	0.00
1983E	II L	NGC3044	SBc	0.0043	90	2.59	0.35	0.03
2002E	II	NGC4129	SBab	0.0039	90	0.12	0.17	0.03
1995F	Ic	NGC2726	Sa	0.0051	90	0.11	0.19	0.04
1999an	II	IC 755	SBb	0.0050	82	0.03	0.35	0.05
2003dr	Ib/c pec	NGC5714	Scd:	0.0075	83	1.95	0.82	0.06
2003dg	Ib/c pec	UGC 6934	Scd:	0.0186	81	0.05	1.50	0.08
2011cb	IIb	IC5249	SBd	0.0078	83	0.93	1.33	0.08
2000G	II	UGC 1773	SB:	0.0121	80	0.28	0.86	0.08
2005ae	IIb	E209-G09	SBcd:	0.0037	82	0.39	1.35	0.10
1997dm	II P:	E294-G17	Sc:	0.0304	85	0.74	3.68	0.11
2011ef	IIb	UGC12640	Sdm:	0.0135	83	0.01	0.79	0.11
2001ci	Ic	NGC3079	SBc	0.0037	80	0.04	1.90	0.11
2009au	IIn	E443-G21	Scd:	0.0095	81	0.15	1.32	0.12
2008U	II	UGC 8917	Scd:	0.0126	84	0.22	1.61	0.13
1988I	IIn	LEDA0086944	Sc	0.0383	90	2.39	2.99	0.13
1981A	II	NGC1532	SBb	0.0040	82	3.96	3.97	0.14
1986J	II	NGC 891	Sb	0.0018	90	0.14	2.23	0.16
1999cr	II	E576-G34	Scd	0.0101	81	1.24	1.00	0.16
2007ac	II	UGC10550	Scd:	0.0307	83	3.92	3.66	0.16
1994ac	II	M+00-60-52	Sc	0.0179	81	0.32	2.49	0.17
2007av	II P	NGC3279	Sd	0.0048	83	0.17	1.50	0.18
2004ay	IIn	UGC11255	Scd:	0.0330	82	0.16	5.49	0.21
1961F	II L:	NGC3003	SBbc	0.0050	83	1.00	3.59	0.21
2003E	II	M-04-12-04	Sbc	0.0148	84	0.30	3.11	0.22
2010gw	II P	IC4992	SBc	0.0140	84	0.58	4.43	0.24
2001cm	II	NGC5965	Sb	0.0115	82	1.96	8.74	0.25
2005aw	Ic	IC4837A	Sb:	0.0134	81	1.26	8.49	0.26
1985O	II	UGC 511	Sc	0.0154	82	1.39	4.12	0.27
2000ez	II	NGC3995	SBm	0.0110	90	2.66	4.81	0.28
2001ey	IIn	M-01-57-10	Sc	0.0255	80	0.38	5.91	0.28
1937A	II P:	NGC4157	SBb	0.0026	90	1.08	2.82	0.28
2001dc	II P	NGC5777	Sb	0.0071	82	0.22	3.62	0.28
2006iv	IIb	UGC 6774	Scd:	0.0081	83	0.20	3.06	0.31
2003da	II	UGC 4992	Scd:	0.0139	84	0.49	3.27	0.35
1995H	II	NGC3526	Sc	0.0047	84	0.48	1.88	0.35
2010bj	II P	NGC2357	Sbc:	0.0076	82	0.06	5.55	0.35
2003J	II P	NGC4157	SBb	0.0026	90	0.14	3.71	0.37
2008eu	II	E289-G10	SBcd	0.0101	80	0.80	4.63	0.39
2005aj	Ic	UGC 2411	S?	0.0085	86	0.39	8.72	0.43
2005ab	II	NGC4617	Sb	0.0155	80	2.34	12.11	0.45
2001ch	Ic	M-01-54-16	Scd	0.0098	82	0.53	3.50	0.46
2001ir	IIn	M-02-22-22	Sd:	0.0199	84	1.16	10.38	0.47
2007sq	II P	M-03-23-05	Sbc:	0.0155	82	0.07	13.00	0.47
1989L	IIn L	NGC7339	SBbc	0.0045	85	0.26	3.34	0.48
2007ag	Ib	UGC 5392	Scd:	0.0209	84	0.40	6.54	0.49
1998en	II	UGC 3645	Sbc	0.0212	82	0.52	8.73	0.52
2010ku	II P	IC 716	Sbc pec	0.0183	80	0.14	10.34	0.59
2001dh	II	M-06-44-26	Sd	0.0085	84	0.95	6.64	0.59
2010E	II P	E013-G28	Sbc	0.0154	80	0.85	10.53	0.61
2004dw	II	UGC11394	Scd:	0.0142	83	0.38	11.19	0.66
2010cl	II P	M-02-25-20	Sd:	0.0090	83	0.23	5.33	0.67
1990Z	II	M+01-57-14	Scd:	0.0250	83	1.29	19.31	0.69
2002bx	II	IC2461	Sb	0.0076	80	0.71	8.11	0.77
1986E	II L	NGC4302	Sc	0.0037	90	0.94	8.52	0.78
2003ac	IIb:	IC3203	Sb	0.0234	82	0.66	17.75	0.85
2003A	Ib/c	UGC 5904	Sb	0.0221	81	1.59	23.10	0.89
2001ak	II	UGC11188	Sd	0.0178	82	0.40	9.35	0.89
2009gc	II:	M-03-28-32	S?	0.0270	82	2.66	20.00	0.96
1940A	II L	NGC5907	Sc	0.0022	90	0.30	14.60	0.96
1992N	II	IC4831	Sab	0.0146	90	1.85	29.50	0.99
2004cr	II	UGC11603	S?	0.0175	86	0.28	16.15	1.22
2005da	Ic pec:	UGC11301	Sc	0.0151	80	1.29	33.65	1.90

Table C.2: *Here we list the sample of SN for the "face-on" study. The first and second column list the SN designation and also its type, determined by a spectral and photometric analysis. The third, fourth, fifth and sixth columns describe some properties of the host galaxy - the host galaxy designation, the galaxy type, its redshift and the inclination of the galaxy respectively. The seventh and eighth columns describe some derived properties - the distance along the disk and the normalised distance along the disk. See Section 2.2 for a full description of these parameters.*

SN Name	SN Type	Host Galaxy	Galaxy Type	Redshift (z)	Inclination (i°)	R_{SN} (kpc)	R_N ($\frac{R_{SN}}{R_{Gal}}$)
1985F	Ib	NGC4618	SBd	0.0018	37	0.56	0.12
2007Y	Ib	NGC1187	SBc	0.0047	46	14.06	0.93
1996N	Ib	NGC1398	SBab	0.005	48	5.13	0.25
1984L	Ib	NGC 991	SBc	0.0051	28	3.88	0.44
2007C	Ib	NGC4981	SBbc	0.0056	46	3.37	0.38
2004ao	Ib	UGC10862	SBc	0.0057	24	2.78	0.30
2004gq	Ib	NGC1832	SBbc	0.0067	49	4.97	0.49
2000de	Ib	NGC4384	Sa	0.008	39	1.02	0.17
2009jf	Ib	NGC7479	SBc	0.008	40	13.23	0.66
1999dn	Ib	NGC7714	SBd: pec	0.0094	42	3.06	0.29
2006gi	Ib	NGC3147	Sbc	0.0094	31	27.34	1.16
2011gd	Ib	NGC6186	SBa	0.0098	41	0.59	0.07
2009iu	Ib	NGC7329	SBc	0.0106	47	19.21	0.79
2003gk	Ib	NGC7460	SBb pec:	0.0108	44	4.13	0.45
1997dc	Ib	NGC7678	Sc	0.0116	45	2.95	0.18
2000dv	Ib	UGC 4671	Sb	0.0138	32	2.75	0.26
2009ha	Ib	M-01-07-24	Sc pec:	0.0148	42	4.64	0.42
2010kc	Ib	NGC7624	Scd:	0.0151	42	1.05	0.12
2006ep	Ib	NGC 214	Sc	0.0151	42	15.22	0.92
1991ar	Ib	IC 49	Sc	0.0153	34	5.26	0.40
2002cw	Ib	NGC6700	SBc	0.0153	46	8.98	0.69
1999di	Ib	NGC 776	Sb	0.0166	12	5.89	0.35
2010ln	Ib	UGC 2685	Sb	0.0171	45	7.37	0.42
2005O	Ib	NGC3340	SBbc	0.019	29	2.68	0.24
2004gv	Ib	NGC 856	S0/a:	0.0202	45	7.31	0.48
2004ew	Ib	E153-G17	Sc	0.022	44	7.97	0.24
2006cb	Ib	NGC5541	Sbc	0.026	46	3.25	0.27
2001fx	Ib	IC5345	Sab	0.0271	45	5.94	0.50
2004eh	Ib	UGC 1892	SBb	0.0339	24	9.32	0.42
2010ig	Ib	UGC 1306	S0	0.0385	27	22.29	0.76
2006jc	Ib pec	UGC 4904	SBbc	0.0056	49	2.18	0.76
2007J	Ib pec	UGC 1778	Sdm:	0.0169	37	5.95	0.50
1982R	Ib:	NGC1187	SBc	0.0047	46	8.66	0.57
2007fo	Ib:	NGC7714	SBd: pec	0.0094	42	2.39	0.23
2011fl	Ib:	IC1584	SBb	0.016	29	5.88	0.39
2011br	Ib:	IC1100	S?	0.0221	34	5.88	0.54
2010if	Ib:	NGC7372	Sbc	0.0398	27	9.64	0.28
2010br	Ib/c	NGC4051	SBbc	0.0023	35	1.01	0.14
2003jg	Ib/c	NGC2997	Sc	0.0036	41	0.89	0.05
2002ji	Ib/c	NGC3655	Sc:	0.0049	49	2.88	0.65
2007rb	Ib/c	NGC2889	Sc	0.0114	29	5.98	0.41
2009iz	Ib/c	UGC 2175	Sbc	0.0143	17	5.40	0.59
2003ih	Ib/c	UGC 2836	S0	0.0167	21	3.31	0.35
2010gr	Ib/c	UGC 2035	Sb	0.0173	49	5.82	0.33
2002cp	Ib/c	NGC3074	Sc	0.0173	27	24.07	1.01

Continued on Next Page...

SN Name	SN Type	Host Galaxy	Galaxy Type	Redshift (z)	Inclination (i°)	R_{SN} (kpc)	R_N ($\frac{R_{SN}}{R_{Gal}}$)
2010il	Ib/c	NGC6922	Sc pec:	0.019	42	2.49	0.17
2010is	Ib/c	M+04-55-02	Sb	0.0212	36	3.77	0.36
2007hb	Ib/c	NGC 819	Sc	0.0221	46	9.38	1.23
1991L	Ib/c	M+07-34-134	Sc	0.0305	48	7.30	0.52
2005ce	Ib/c:	IC5233	S?	0.0249	37	5.97	0.43
2010av	Ib/c:	IC1099	Sc:	0.0301	34	13.61	0.64
1994I	Ic	NGC5194	Sbc	0.0015	48	0.63	0.07
1983I	Ic	NGC4051	SBbc	0.0023	35	2.63	0.37
2000ew	Ic	NGC3810	Sc	0.0032	44	1.32	0.16
1997dq	Ic	NGC3810	Sc	0.0032	44	4.40	0.55
2005kl	Ic	NGC4369	Sa	0.0033	12	0.48	0.12
1997X	Ic	NGC4691	SB0/a pec	0.0037	36	0.64	0.10
1962L	Ic	NGC1073	SBc	0.004	25	6.10	0.54
2003bg	Ic	M-05-10-15	SBc	0.0044	42	2.56	0.60
2002jz	Ic	UGC 2984	SBdm:	0.0052	34	0.54	0.11
1996aq	Ic	NGC5584	Scd	0.0054	44	2.47	0.23
2008eb	Ic	NGC6574	Sbc:	0.0078	39	2.48	0.38
1990U	Ic	NGC7479	SBc	0.008	40	9.15	0.46
2002ho	Ic	NGC4210	SBb	0.0085	39	3.17	0.32
2005az	Ic	NGC4961	SBcd	0.0086	46	1.78	0.22
2009bb	Ic	NGC3278	Sc	0.0099	45	4.28	0.56
2009jy	Ic	NGC3208	Sbc	0.0101	29	8.18	0.76
2005cb	Ic	NGC6753	Sb	0.0105	29	5.76	0.38
1997B	Ic	IC 438	Sc	0.0105	41	9.33	0.54
2002jp	Ic	NGC3313	SBab	0.0126	36	42.80	1.49
2007rz	Ic	NGC1590	Sc	0.0128	32	2.21	0.34
2001M	Ic	NGC3240	Scd:	0.0133	32	5.12	0.60
2005bq	Ic	IC4367	Sc	0.0138	29	2.62	0.18
2005dg	Ic	E420-G03	Sc	0.0138	47	3.64	0.23
2010do	Ic	NGC5374	SBbc?	0.0144	29	7.29	0.51
2010X	Ic	NGC1573A	Sbc	0.0151	37	2.55	0.18
2008du	Ic	NGC7422	SBb	0.0162	34	3.03	0.34
1998ey	Ic	NGC7080	SBb	0.0162	17	8.93	0.52
2002hn	Ic	NGC2532	Sc	0.0173	34	1.57	0.07
2004fe	Ic	NGC 132	Sbc	0.0179	42	7.00	0.35
2002bm	Ic	M-01-32-19	SBbc	0.0184	12	6.93	0.27
2003is	Ic	M+07-40-03	Sc	0.0185	0	1.92	0.16
2002hf	Ic	M-05-03-20	Sc	0.019	21	7.39	0.39
2003el	Ic	NGC5000	SBbc	0.0191	32	6.65	0.35
2011bh	Ic	NGC2431	SBa	0.0191	21	7.79	0.74
2003bu	Ic	NGC5393	SBa	0.0202	42	4.36	0.40
1999bc	Ic	M+03-22-14	Sb	0.0212	41	7.93	0.61
2004eu	Ic	M+07-05-39	Sb	0.0219	35	4.11	0.44
2011bm	Ic	IC3918	Sbc	0.022	45	3.99	0.60
2005bh	Ic	UGC 6495	Sb:	0.0221	21	7.41	0.61
2007cl	Ic	NGC6479	Sc	0.0224	24	3.87	0.29
2009dp	Ic	NGC6912	SBc	0.024	34	4.84	0.25
2008gj	Ic	NGC7321	SBb	0.0241	49	17.83	0.78
2005bk	Ic	M+07-33-27	S:	0.0247	0	3.48	0.27
2001ai	Ic	NGC5278	Sb pec	0.0255	45	6.41	0.32
2003bm	Ic	UGC 4226	Scd	0.0267	34	12.25	0.47
2005mf	Ic	UGC 4798	Scd	0.0271	29	7.78	0.45
2011ee	Ic	NGC7674	Sbc pec	0.0293	24	6.72	0.35
2002cg	Ic	UGC10415	Sb	0.0312	29	1.96	0.10
2001ii	Ic	UGC 444	Sbc	0.0363	46	11.64	0.48
2010ak	Ic	M+03-41-142	Sbc pec	0.0375	49	8.62	0.37

Continued on Next Page...

SN Name	SN Type	Host Galaxy	Galaxy Type	Redshift (z)	Inclination (i°)	R_{SN} (kpc)	R_N ($\frac{R_{SN}}{R_{Gal}}$)
2002ap	Ic pec	NGC 628	Sc	0.0021	24	12.01	0.93
2003id	Ic pec	NGC 895	Scd	0.0078	45	6.89	0.41
2003jd	Ic pec	M-01-59-21	Sm	0.019	41	5.13	0.33
2005lr	Ic:	E492-G02	Sb pec	0.0087	46	4.32	0.40
2000F	Ic:	IC 302	SBbc	0.0198	36	9.63	0.44
2004dx	Ic:	M+07-37-36	S?	0.0303	32	4.61	0.33
2001dq	Ic?	IC1222	Sc	0.0312	37	12.53	0.40
1998dn	II	NGC 337A	Sdm	0.0013	41	3.81	0.85
1921B	II	NGC3184	SBc	0.002	15	6.46	0.72
2009ls	II	NGC3423	Scd	0.0028	31	1.93	0.31
1994P	II	M+09-20-51	SBc	0.0036	47	7.90	1.08
1992bd	II	NGC1097	SBb	0.0043	47	0.94	0.04
1947A	II	NGC3177	Sb	0.0043	42	3.86	1.01
1995ag	II	UGC11861	Sd	0.005	47	3.32	0.33
1997db	II	UGC11861	Sd	0.005	47	5.10	0.50
1995X	II	UGC12160	Sc	0.0052	37	2.57	0.40
1964F	II	NGC4303	SBbc	0.0053	25	3.19	0.15
1961I	II	NGC4303	SBbc	0.0053	25	9.32	0.45
2004G	II	NGC5668	Scd	0.0053	22	4.76	0.47
1996W	II	NGC4027	SBdm	0.0055	41	4.18	0.41
1995ad	II	NGC2139	Scd	0.0061	42	3.99	0.42
2004ep	II	IC2152	SBa	0.0063	46	1.44	0.23
2000cb	II	IC1158	Sc	0.0064	47	4.97	0.54
2002ce	II	NGC2604	SBcd	0.0067	0	2.62	0.32
2005kh	II	NGC3094	SBa	0.0074	46	7.87	0.91
2004be	II	E499-G34	SBm	0.0076	27	0.72	0.14
2003hr	II	NGC2551	S0/a	0.0076	47	7.95	1.07
1978H	II	NGC3780	Sc	0.008	38	3.39	0.24
2005dl	II	NGC2276	SBc	0.0081	21	3.05	0.23
1993X	II	NGC2276	SBc	0.0081	21	11.94	0.89
2004eg	II	UGC 3053	Scd:	0.0081	29	3.63	0.90
2008cn	II	NGC4603	Sc:	0.0082	44	3.93	0.24
1998ce	II	M-04-24-19	SBdm:	0.0084	37	2.48	0.25
1999gk	II	NGC4653	Scd	0.0085	29	8.06	0.52
1997Z	II	NGC3261	SBb	0.0087	41	9.71	0.51
2009af	II	UGC 1551	SBc	0.0089	32	3.28	0.23
1981E	II	NGC5597	SBc	0.0089	35	3.75	0.35
2006ca	II	UGC11214	Scd:	0.0089	34	4.28	0.61
1993K	II	NGC2223	SBb	0.0091	29	8.34	0.53
2002dq	II	NGC7051	SBa	0.0091	34	5.54	0.79
1997ds	II	M-01-57-07	SBd:	0.0095	27	2.91	0.27
2009aj	II	E221-G18	Sab	0.0095	36	3.19	0.63
2004cx	II	NGC7755	SBc:	0.0097	41	5.23	0.24
2007W	II	NGC5105	SBc	0.0097	42	7.97	0.70
1995J	II	NGC4512	SBd	0.01	47	9.66	0.82
2008br	II	IC2522	SBc pec	0.0101	44	5.00	0.31
2000M	II	NGC6389	Sbc	0.0103	49	3.57	0.21
2002gw	II	NGC 922	SBcd	0.0103	36	8.73	0.74
1992ab	II	NGC6389	Sbc	0.0103	49	18.63	1.09
2008fq	II	NGC6907	SBbc	0.0106	42	2.00	0.09
2002ca	II	UGC 8521	SBab	0.0109	34	3.63	0.48
1999dh	II	IC 211	Scd	0.0109	37	6.94	1.08
2005io	II	UGC 3361	SBdm:	0.0111	34	4.57	0.77
1991J	II	NGC5020	SBbc	0.0113	32	16.15	0.77
2007an	II	NGC4017	Sbc	0.0114	39	5.58	0.47
2006st	II	NGC4017	Sbc	0.0114	39	17.52	1.47

Continued on Next Page...

SN Name	SN Type	Host Galaxy	Galaxy Type	Redshift (z)	Inclination (i°)	R_{SN} (kpc)	R_N ($\frac{R_{SN}}{R_{Gal}}$)
2003bw	II	IC1077	SBbc?	0.0115	36	2.97	0.32
2006ci	II	E182-G10	Sc pec	0.0119	42	7.41	0.57
1998W	II	NGC3075	Sc	0.012	48	5.68	0.67
2008P	II	NGC2550A	Sc	0.0122	32	2.53	0.22
2003bj	II	IC4219	SBb pec	0.0122	27	4.15	0.54
1998ar	II	NGC2916	Sb	0.0123	47	10.15	0.57
2005H	II	NGC 838	S0: pec	0.0129	41	0.60	0.07
2002an	II	NGC2575	Scd:	0.013	32	10.83	0.62
2001J	II	UGC 4729	SBcd:	0.0132	32	5.34	0.69
2008ex	II	UGC11428	Scd:	0.0133	0	2.58	0.33
2000N	II	M-02-34-54	SBbc	0.0134	45	11.36	0.81
1997bn	II	UGC 4329	Scd	0.0138	41	2.44	0.15
2003ef	II	NGC4708	Sab pec?	0.0138	45	4.72	0.44
2007ct	II	NGC6944A	SBd: pec	0.0141	45	6.53	0.79
2003bl	II	NGC5374	SBbc?	0.0144	29	6.32	0.44
1987C	II	M+09-14-47	S pec:	0.0144	29	6.46	1.03
2003ho	II	E235-G58	SBd	0.0145	47	7.59	0.37
2004gf	II	UGC11864	SBdm	0.0145	37	13.77	0.74
2008bh	II	NGC2642	SBbc	0.0148	21	8.50	0.48
2004er	II	M-01-07-24	Sc pec:	0.0148	42	7.14	0.65
1999go	II	NGC1376	Scd	0.0149	29	4.97	0.28
2001ee	II	NGC2347	Sb:	0.0151	45	6.41	0.41
2006ee	II	NGC 774	S0	0.0154	39	4.36	0.32
2006ms	II	NGC6935	Sa	0.0156	32	5.66	0.31
2011dy	II	UGC12628	SBc:	0.0156	39	10.37	0.75
2001cy	II	UGC11927	SBb	0.0158	41	2.90	0.23
2005dk	II	IC4882	SBb:	0.0159	34	5.22	0.57
2006V	II	UGC 6510	Scd	0.016	21	16.83	0.94
2004dv	II	M-01-06-12	SBb	0.0162	45	9.48	0.87
2001cx	II	UGC12266	SBab	0.0163	36	7.61	0.72
1999et	II	NGC1643	SBbc pec:	0.0164	0	3.66	0.35
2001cl	II	NGC7260	Sbc	0.0165	41	7.49	0.41
2007gw	II	NGC4161	Sbc	0.0166	49	3.69	0.35
2006dk	II	NGC4161	Sbc	0.0166	49	4.42	0.41
2001di	II	UGC 3259	Sd	0.0166	41	16.51	0.95
2010id	II	NGC7483	Sa	0.0167	49	38.51	2.42
2010hb	II	UGC 2537	Scd	0.0168	17	10.64	0.90
2001ab	II	NGC6130	SBbc:	0.017	47	5.55	0.53
1998cu	II	IC1525	SBb	0.017	44	19.65	1.01
2003ej	II	UGC 7820	Scd:	0.0173	29	10.91	0.58
2002bh	II	UGC 5286	Sd	0.0175	47	12.19	0.58
2008fc	II	UGC 2883	Sb	0.0175	41	6.39	0.62
1990ah	II	M+02-02-09	SBd	0.0176	46	4.00	0.32
2004ek	II	M+05-03-75	S	0.0176	34	15.45	0.71
2001H	II	M-01-10-19	Scd	0.0177	37	2.58	0.13
2003C	II	UGC 439	SBa	0.0177	17	3.32	0.28
2011dk	II	NGC7003	Sbc	0.018	49	1.87	0.15
1996bw	II	NGC 664	Sb:	0.0182	34	7.24	0.45
1997W	II	NGC 664	Sb:	0.0182	34	7.60	0.47
2003cn	II	IC 849	Scd?	0.0182	37	12.92	0.78
2005I	II	IC 983	SBbc	0.0184	29	18.61	0.32
2007L	II	UGC 466	SBa	0.0184	17	11.44	0.78
2006cx	II	NGC7316	Sc	0.0188	37	1.77	0.15
2008T	II	UGC 3304	Sbc	0.0188	0	4.49	0.35
1985R	II	IC1809	SBab	0.0188	44	10.83	1.03
2006bx	II	UGC 5434	Sb	0.0188	41	27.21	1.91

Continued on Next Page...

SN Name	SN Type	Host Galaxy	Galaxy Type	Redshift (z)	Inclination (i°)	R_{SN} (kpc)	R_N ($\frac{R_{SN}}{R_{Gal}}$)
2007fp	II	NGC3340	SBbc	0.019	29	1.52	0.14
1999ge	II	NGC 309	Sc	0.019	34	7.67	0.23
2008bj	II	M+08-22-20	Sd	0.0191	47	2.61	0.53
2005dz	II	UGC12717	Scd:	0.0191	24	11.37	0.97
2003jc	II	M-01-58-18	S?	0.0194	0	8.08	0.54
2009jw	II	M+07-16-08	Sbc	0.0197	45	3.51	0.25
2006dp	II	M-01-03-56	Sc	0.0197	17	4.82	0.33
2004dh	II	M+04-01-48	Sbc	0.0197	39	3.36	0.33
2019:00:00	II	UGC11585	Sb	0.02	29	14.10	0.69
2000di	II	IC1637	SBc:	0.0202	41	7.75	0.38
2004fb	II	E340-G07	S?	0.0206	27	2.99	0.21
2002eo	II	NGC 710	Scd:	0.0206	17	6.66	0.43
1994ad	II	E152-G26	SBa	0.0207	49	15.86	0.72
2006C	II	UGC 7020	Sbc	0.0207	29	24.54	0.94
2011go	II	M+07-15-02	S?	0.0211	0	3.24	0.40
2009ii	II	UGC 3627	Sd	0.0211	49	13.36	0.92
2008il	II	E355-G04	SBb	0.0213	46	12.46	0.77
2007il	II	IC1704	Sbc	0.0214	44	5.98	0.43
2005aa	II	M+05-22-08	Scd	0.0216	46	4.58	0.43
2004T	II	UGC 6038	Sb	0.0217	17	5.24	0.37
2005dq	II	UGC12177	S?	0.0219	24	4.10	0.32
2000I	II	NGC2958	Sbc	0.0224	41	4.54	0.33
2009ay	II	NGC6479	Sc	0.0224	24	5.71	0.43
2005gm	II	NGC1423	SBa	0.0224	49	9.17	0.73
2003gg	II	IC1321	SBbc	0.0225	46	3.06	0.21
2002as	II	UGC 3418	SBb	0.0228	17	5.48	0.39
2005Q	II	E244-G31	Sc	0.0228	34	14.72	0.69
2005me	II	E244-G31	Sc	0.0228	34	18.36	0.86
2006du	II	IC1529	S0	0.0233	17	22.03	0.97
2010bs	II	UGC 7416	SBb	0.0234	32	16.83	0.79
2003hk	II	NGC1085	Sbc:	0.0236	45	4.29	0.10
1997co	II	NGC5125	Sb	0.0236	37	7.55	0.33
2001ae	II	IC4229	SBb:	0.0236	44	11.13	0.78
2002C	II	IC3376	SBa	0.024	42	20.93	0.87
2004gr	II	NGC3678	Sbc	0.0243	21	5.46	0.47
2003at	II	M+11-20-23	Sbc	0.0243	29	6.63	0.81
2007ab	II	M-01-43-02	SBbc	0.0244	32	24.23	0.83
2001fy	II	UGC11922	Sc	0.0245	32	1.76	0.15
2006ai	II	E005-G09	SBdm	0.0251	37	1.80	0.12
2010D	II	UGC 5714	SBc	0.0251	37	8.60	0.61
1999ew	II	NGC3677	S0/a:	0.0253	32	3.33	0.11
2004ed	II	NGC6786	SB?	0.0254	34	5.98	0.37
2003eg	II	NGC4727	SBbc	0.0258	47	9.70	0.38
2005dt	II	M-03-59-06	SBc:	0.0259	37	7.21	0.37
2005cv	II	UGC 1359	SB?	0.026	17	3.26	0.27
2011O	II	UGC 8829	SBa	0.0263	36	5.43	0.34
2003kw	II	UGC 6314	S?	0.0266	34	4.74	0.39
2011G	II	UGC 7144	Sb	0.0266	29	16.25	1.09
2001aj	II	UGC10243	SBc:	0.0268	21	8.72	0.61
2004I	II	NGC1072	SBb	0.0271	19	3.47	0.15
2001ag	II	M+08-18-09	SB	0.0271	44	3.61	0.33
2003db	II	M+05-23-21	Sc	0.0272	46	7.05	0.56
2005kx	II	NGC3197	Sbc	0.0273	41	4.39	0.21
2010ck	II	M+06-31-61	SBa	0.0277	47	6.54	0.45
2005bt	II	UGC 8205	Sb	0.028	44	2.75	0.18
2005bp	II	UGC10732	Sbc:	0.028	42	8.59	0.57

Continued on Next Page...

SN Name	SN Type	Host Galaxy	Galaxy Type	Redshift (z)	Inclination (i°)	R_{SN} (kpc)	R_N ($\frac{R_{SN}}{R_{Gal}}$)
2008dz	II	NGC5123	Scd:	0.028	24	13.69	0.66
2003T	II	UGC 4864	Sab	0.0281	0	16.02	0.51
1994A	II	UGC 8214	SBb	0.0282	29	5.87	0.48
2005D	II	UGC 3856	Scd:	0.0288	32	25.29	1.53
2000du	II	UGC 3920	Sb	0.0289	12	8.29	0.37
2006ds	II	PGC0070011	Sa	0.0295	36	3.84	0.39
2007G	II	UGC 68	SBbc	0.0297	36	2.11	0.13
2001af	II	M-04-24-01	SBbc	0.0298	42	16.23	0.70
2003ab	II	UGC 4930	Scd:	0.0299	49	7.93	0.56
2001dy	II	M+04-40-16	Sbc	0.0304	46	4.83	0.54
2001W	II	M+07-34-134	Sc	0.0305	48	18.31	1.32
2003la	II	M+10-15-89	Sab	0.0313	42	3.14	0.35
2008ev	II	UGC10155	Scd:	0.0314	32	3.94	0.21
2006dq	II	UGC11089	Sbc	0.0316	48	10.63	0.60
2003hf	II	UGC10586	Sb	0.0318	27	4.00	0.13
2001ea	II	M+05-54-38	S?	0.0324	0	7.06	0.67
2005cw	II	IC1439	SBa	0.0327	49	13.98	0.55
2005bi	II	M+07-34-36	Sbc	0.0336	45	9.12	0.53
2002en	II	UGC12289	Sd	0.0345	17	10.66	0.41
2003ht	II	UGC 2457	Scd	0.0347	17	4.49	0.21
2001it	II	M+09-25-15	Sc	0.0351	29	5.78	0.35
2003gv	II	M+05-03-66	S?	0.0354	0	7.70	0.67
2001id	II	UGC12424	Sb:	0.036	34	6.53	0.24
2003hi	II	M+07-33-16	S?	0.0364	36	7.73	0.66
2006cd	II	IC1179	SBcd	0.0376	47	9.51	0.73
2005es	II	M+01-59-79	S?	0.0385	34	7.76	0.52
2009hj	II	NGC7372	Sbc	0.0398	27	5.37	0.16
2000dq	II	M+00-06-43	Sb	0.0418	34	10.92	0.67
2003ii	II	M+06-06-53	Sbc	0.0457	36	8.53	0.58
2007iv	II	UGC12917	SBb	0.0461	42	13.67	0.46
2001dz	II	UGC 471	Sbc	0.0506	32	16.92	0.37
2006aq	II	M+07-24-32	SBb	0.0514	41	10.23	0.55
1926A	II L	NGC4303	SBbc	0.0053	25	7.27	0.35
1979C	II L	NGC4321	SBbc	0.0053	36	12.79	0.54
2009kr	II L	NGC1832	SBbc	0.0067	49	4.74	0.47
1996L	II L	E266-G10	S:	0.0336	37	15.14	0.94
2008bk	II P	NGC7793	Sd	0.0007	47	2.54	0.66
1999gq	II P	NGC4523	Sm	0.0009	21	0.82	0.76
1999gi	II P	NGC3184	SBc	0.002	15	2.41	0.27
2003gd	II P	NGC 628	Sc	0.0021	24	6.80	0.53
2003ie	II P	NGC4051	SBbc	0.0023	35	4.49	0.63
1999em	II P	NGC1637	Sc	0.0024	36	1.14	0.20
2006my	II P	NGC4651	Sc	0.0027	49	2.14	0.33
2009N	II P	NGC4487	Scd	0.0036	47	5.92	0.67
1940B	II P	NGC4725	SBab	0.004	49	11.90	0.48
2003B	II P	NGC1097	SBb	0.0043	47	16.58	0.70
2007aa	II P	NGC4030	Sbc	0.0048	44	8.77	0.75
1983K	II P	NGC4699	SBb	0.0048	43	18.61	1.70
2001X	II P	NGC5921	SBbc	0.0049	36	4.22	0.30
2001fv	II P	NGC3512	Sc	0.0049	21	2.40	0.51
1988A	II P	NGC4579	SBb	0.0051	38	5.83	0.33
1999gn	II P	NGC4303	SBbc	0.0053	25	5.35	0.26
2006ov	II P	NGC4303	SBbc	0.0053	25	5.42	0.26
2008in	II P	NGC4303	SBbc	0.0053	25	11.94	0.58
2005ad	II P	NGC 941	Sc	0.0053	42	5.97	0.73
2009G	II P	IC4444	Sbc:	0.0065	34	0.64	0.10

Continued on Next Page...

SN Name	SN Type	Host Galaxy	Galaxy Type	Redshift (z)	Inclination (i°)	R_{SN} (kpc)	R_N ($\frac{R_{SN}}{R_{Gal}}$)
2008X	II P	NGC4141	SBcd:	0.0066	45	1.19	0.24
2009E	II P	NGC4141	SBcd:	0.0066	45	2.79	0.56
2009hq	II P	NGC4152	Sc	0.0069	39	4.16	0.46
2003ao	II P	NGC2993	Sa pec	0.0075	46	1.78	0.30
2010F	II P	NGC3120	Sbc:	0.0089	45	6.30	0.68
2002ed	II P	NGC5468	Scd	0.0095	24	10.61	0.72
2008ho	II P	NGC 922	SBcd	0.0103	36	9.28	0.79
2009ga	II P	NGC7678	Sc	0.0116	45	7.40	0.46
2009bu	II P	NGC7408	SBcd:	0.0116	39	5.33	0.52
2009hf	II P	NGC 175	SBab	0.0128	29	10.82	0.67
2010ie	II P	NGC2333	Sa	0.0144	44	10.62	1.31
2009kl	II P	IC2548	SBb	0.0149	27	8.09	0.47
2008ag	II P	IC4729	Sc	0.0149	36	12.04	0.87
2008ea	II P	NGC7624	Scd:	0.0151	42	5.11	0.59
2006it	II P	NGC6956	SBb	0.0157	17	11.36	0.63
2007hv	II P	UGC 2858	Sdm	0.017	44	9.77	0.72
2009es	II P	IC1525	SBb	0.017	44	15.57	0.80
1965N	II P	NGC3074	Sc	0.0173	27	4.06	0.17
2008F	II P	M-01-08-15	SBa	0.0182	41	11.12	0.64
2008dn	II P	UGC11946	Sc	0.0184	41	11.21	0.95
2009lb	II P	UGC 2944	S?	0.0188	45	4.01	0.23
2008hg	II P	IC1720	Sbc	0.0189	43	7.78	0.60
2008W	II P	M-03-22-07	Sc	0.0193	29	6.21	0.61
2007ah	II P	UGC 2931	Sc	0.0194	24	1.89	0.17
2010hm	II P	UGC12687	SBbc	0.0206	41	7.56	0.36
2008cy	II P	M-02-39-16	Sd	0.0208	36	5.62	0.40
2007aq	II P	IC2409	Sa	0.0212	41	23.38	1.88
2010aj	II P	M-01-32-35	Sbc:	0.0214	49	7.62	0.57
2008gr	II P	IC1579	SBbc:	0.0231	49	11.27	0.89
2010kx	II P	NGC7645	SBc	0.0232	32	6.14	0.31
2010jc	II P	NGC1033	Sc:	0.0245	29	18.06	0.95
2009dm	II P	M+07-24-16	Sc	0.0247	44	7.74	0.84
2011cl	II P	IC2373	Sc	0.0254	0	18.47	1.15
2009lx	II P	M+01-30-08	SBb:	0.0272	39	9.62	0.69
2007ck	II P	M+05-43-16	S?	0.0273	36	11.97	0.84
2011bi	II P	M+07-35-37	Sc	0.0281	27	4.71	0.38
2006bs	II P	M+00-27-14	Sc	0.0303	43	7.52	0.61
2008fe	II P	UGC 9578	SBb	0.0314	17	16.08	0.83
2009ll	II P	E122-G04	SBab	0.0456	29	13.07	0.46
1999eu	II P pec	NGC1097	SBb	0.0043	47	16.41	0.70
1937F	II P:	NGC3184	SBc	0.002	15	5.94	0.67
1992bt	II P:	NGC3780	Sc	0.008	38	3.45	0.24
2010ct	II P:	NGC3362	Sc	0.0282	39	18.54	0.79
1997D	II pec	NGC1536	SBc pec:	0.0052	44	4.59	0.75
2011cq	II pec	M+00-31-44	Sbc:	0.0173	34	11.30	0.79
2001dj	II pec	NGC 180	SBbc	0.0177	36	33.99	1.36
2003ka	II pec	M+06-50-20	S:	0.0195	0	4.11	0.41
2004gg	II pec	UGC 5234	Sc	0.0203	46	5.71	0.30
2001Y	II pec	NGC3362	Sc	0.0282	39	10.08	0.43
2009jq	II pec	UGC 1919	SBb	0.0366	36	22.44	0.77
1966E	II:	NGC4189	SBc	0.0071	47	8.02	0.80
1968V	II:	NGC2276	SBc	0.0081	21	8.43	0.63
1991au	II:	UGC11616	Sc	0.0088	36	2.45	0.47
1999A	II:	NGC5874	Sc	0.0105	46	8.82	0.62
2003ja	II:	NGC 846	SBab	0.0165	29	4.85	0.26
2005lx	II:	IC 221	Sc	0.0168	42	11.70	0.71

Continued on Next Page...

SN Name	SN Type	Host Galaxy	Galaxy Type	Redshift (z)	Inclination (i°)	R_{SN} (kpc)	R_N ($\frac{R_{SN}}{R_{Gal}}$)
2003iy	II:	NGC6143	Sbc:	0.0176	17	3.12	0.32
2003gu	II:	UGC12331	S?	0.0195	47	7.62	0.75
2002at	II:	NGC3720	Sa:	0.0201	24	3.23	0.29
2003gw	II:	UGC 3252	Sc	0.0206	34	6.63	0.23
2009hz	II:	UGC11499	Sdm:	0.0256	24	11.17	0.85
2004gx	II:	UGC12663	S?	0.0269	24	4.77	0.29
2003gm	II?	NGC5334	SBc:	0.0046	44	5.32	0.47
1971K	II* P	NGC3811	SBc	0.0104	42	9.39	0.69
2006G	II/IIb	NGC 521	SBbc	0.0169	25	17.92	0.58
2011dh	IIb	NGC5194	Sbc	0.0015	48	6.41	0.73
2001ig	IIb	NGC7424	Scd	0.0031	32	11.86	0.68
2001ad	IIb	NGC6373	Sc	0.0111	39	9.82	1.14
2006ss	IIb	NGC5579	Scd	0.0121	44	7.26	0.54
2006qp	IIb	NGC5735	SBbc	0.0126	37	9.75	0.55
2008ie	IIb	NGC1070	Sb	0.0138	34	7.88	0.42
2007ay	IIb	UGC 4310	Sm	0.0146	21	5.93	0.56
2004ex	IIb	NGC 182	Sa pec:	0.0176	34	14.80	0.72
2008cx	IIb	NGC 309	Sc	0.019	34	24.95	0.74
2009fz	IIb	NGC6209	Sbc	0.0198	39	21.88	0.92
2001cf	IIb	UGC 7020	Sbc	0.0207	29	23.68	0.91
2006dl	IIb	M+04-31-05	Sbc	0.0221	39	5.07	0.65
1987K	IIb:	NGC4651	Sc	0.0027	49	1.31	0.20
2008ay	IIb:	UGC 8050	SBbc	0.0353	17	12.66	0.48
2010ad	IIb:	M+03-41-52	S0/a	0.0449	45	6.44	0.40
1999el	IIn	NGC6951	Sbc	0.0044	34	2.33	0.23
2011fh	IIn	NGC4806	SBc	0.0081	34	4.09	0.73
1994Y	IIn	NGC5371	SBbc	0.0086	37	7.50	0.36
2011A	IIn	NGC4902	SBb	0.0088	25	9.72	0.68
2003G	IIn	IC 208	Sbc	0.0116	12	2.64	0.21
2005aq	IIn	NGC1599	SBc pec:	0.0135	24	2.92	0.43
2002fj	IIn	NGC2642	SBbc	0.0148	21	7.16	0.40
2003lo	IIn	NGC1376	Scd	0.0149	29	6.28	0.36
2005db	IIn	NGC 214	Sc	0.0151	42	5.74	0.35
2006bo	IIn	UGC11578	Sdm	0.0155	43	7.44	0.53
2009kn	IIn	M-03-21-06	Sb:	0.0159	41	5.40	0.63
1995G	IIn	NGC1643	SBbc pec:	0.0164	0	4.91	0.47
2001I	IIn	UGC 2836	S0	0.0167	21	1.65	0.17
1999gb	IIn	NGC2532	Sc	0.0173	34	7.99	0.36
2004gd	IIn	NGC2341	Sc	0.0176	17	1.32	0.15
2001fa	IIn	NGC 673	Sc	0.0176	39	6.29	0.28
2004F	IIn	NGC1285	SBb pec	0.0177	46	5.28	0.34
1999eb	IIn	NGC 664	Sb:	0.0182	34	2.64	0.16
2006jd	IIn	UGC 4179	SBb	0.0187	34	9.45	0.73
2008B	IIn	NGC5829	Sc	0.0192	29	9.43	0.47
2007bb	IIn	UGC 3627	Sd	0.0211	49	13.75	0.94
2007K	IIn	M+06-20-50	SBa	0.0219	0	3.48	0.31
2005cp	IIn	UGC12886	Sbc	0.0224	41	2.72	0.13
2007rt	IIn	UGC 6109	Sc	0.0226	0	3.02	0.19
2003as	IIn	M+08-10-07	Sbc	0.0235	32	5.09	0.51
2011ap	IIn	IC1277	Scd:	0.0239	27	12.68	0.57
2008aj	IIn	M+06-30-34	SBc	0.0252	34	3.95	0.37
2005cl	IIn	M-01-53-20	SBb	0.0261	27	12.77	0.60
2002bv	IIn	UGC 4042	SBb:	0.0281	34	9.13	0.62
2002cb	IIn	M+08-24-34	SBc	0.03	21	7.12	0.69
2008be	IIn	NGC5671	SBb	0.0305	46	24.08	0.79
2005cy	IIn	UGC11241	Sb	0.0337	27	8.72	0.44

Continued on Next Page...

SN Name	SN Type	Host Galaxy	Galaxy Type	Redshift (z)	Inclination (i°)	R_{SN} (kpc)	R_N ($\frac{R_{SN}}{R_{Gal}}$)
2008en	IIn	UGC 564	Sbc	0.0375	45	17.32	0.86
2005R	IIn	UGC 6274	Scd:	0.0378	29	2.50	0.13
2005gn	IIn	E488-G30	Sc	0.0405	49	8.55	0.34
2004ec	IIn	UGC10717	Sd	0.0429	37	1.98	0.09
1987B	IIn L	NGC5850	SBb	0.0086	36	32.65	1.48
2007pk	IIn pec	NGC 579	Scd	0.0169	29	2.84	0.25
2002bu	IIn?	NGC4242	Sdm	0.0022	41	5.33	0.82